UNIVERSITY OF CALIFORNIA, SAN DIEGO

An Optical Nanofiber Total Internal Reflection Microscopy Platform for

Quantitatively Probing Nanoscale Interactions

A dissertation submitted in partial satisfaction of the

requirements for the degree of Doctor of Philosophy

in

NanoEngineering

by

Joshua T. Villanueva

Committee in charge:

Professor Donald Sirbuly, Chair
Professor Gaurav Arya
Professor Michael Heller
Professor Yu-Hwa Lo
Professor David Saintillan

2016

The dissertation of Joshua T. Villanueva is approved, and it is acceptable in quality and form for publication on microfilm and electronically:

_____

_____

_____

_____

_____

Chair

University of California, San Diego

2016

DEDICATION

This thesis is dedicated to Leonie and Rene Villanueva, my mom and dad.

EPIGRAPH

"There would seem to be nothing more obvious, more tangible and palpable than the present moment. And yet it eludes us completely. All the sadness of life lies in that fact. In the course of a single second, our senses of sight, of hearing, of smell, register (knowingly or not) a swarm of events and a parade of sensations and ideas passes through our head. Each instant represents a little universe, irrevocably forgotten in the next instant."

- Milan Kundera

TABLE OF CONTENTS

LIST OF ABBREVIATIONS

AFM   Atomic force microscopy

BD   Brownian dynamics

CNP   Citrate-coated nanoparticle

DLS   Dynamic light scattering

DNA   Deoxyribonucleic acid

DNA-NP   DNA-coated nanoparticle

DNA-WG   DNA-coated waveguide

EDL   Electric double layer

MW   Molecular weight

NP   Nanoparticle

P-B   Poisson-Boltzmann (equation)

PDF   Probability density function

TIR   Total internal reflection

TIRM   Total internal reflection microscopy

WG   Waveguide

LIST OF FIGURES

ACKNOWLEDGEMENTS

I would like to acknowledge Professor Donald J. Sirbuly for his support as chair of my committee. His guidance during my doctoral program has been invaluable, and his patience much appreciated as I learned to formulate my own research questions and investigate them in a thoughtfully detailed and methodical manner. He has helped me become an independent researcher.

I would also like to acknowledge our collaborators, Professor Gaurav Arya and Professor Yi Chen, as well as the past and current members of the Sirbuly Lab for their valuable feedback and meaningful discussions. It is always helpful to gain another perspective, and I am thankful for the experience working with them.

Finally I would like to acknowledge my family and my friends. Completing this dissertation would not have been possible without each and every one of them. Their unwavering support has been integral to my personal growth and professional development. For that I am deeply humbled and forever grateful.

Chapters 2, 3, 4, 5, and 6, in part, are currently being prepared for submission for publication of the material. (Villanueva, Joshua, Qian Huang, Gaurav Arya, Donald. J. Sirbuly) The dissertation author is the primary investigator and author of this material.

Chapter 7, in part, is a reprint of the material that appears in *Journal of Applied Physics*. (**Villanueva, Joshua**, Qian Huang, Donald J. Sirbuly. "Identification and design of novel polymer-based mechanical transducers: A nano-structural model for

thin film indentation." *Journal of Applied Physics* 116, no. 10 (2014): 104307.) The

dissertation author was the primary investigator and author of this material.

VITA

2011   Bachelor of Science, Boston University

2013   Master of Science, University of California, San Diego

2016   Doctor of Philosophy, University of California, San Diego

PUBLICATIONS

Villanueva, Joshua, Qian Huang, Donald J. Sirbuly. "Identification and design of novel polymer-based mechanical transducers: A nano-structural model for thin film indentation." *Journal of Applied Physics* 116, no. 10 (2014): 104307.

Huang, Qian, Fernando Teran Arce, Joon Lee, Ilsun Yoon, **Joshua Villanueva**, Ratnesh Lal, and Donald J. Sirbuly. "Gap controlled plasmon-dielectric coupling effects investigated with single nanoparticle-terminated atomic force microscope probes." *Nanoscale* (2016).

Ma, Yaoguang, Qian Huang, Tianlong Li, **Joshua Villanueva**, Nam H. Nguyen, James Friend, and Donald J. Sirbuly. "A local nanofiber optic ear." *ACS Photonics* (2016).

Sirbuly, Donald J., Raymond W. Friddle, **Joshua Villanueva**, and Qian Huang. "Nanomechanical force transducers for biomolecular and intracellular measurements: is there room to shrink and why do it?." *Reports on Progress in Physics* 78, no. 2 (2015): 024101.

Huang, Qian, Ilsun Yoon, **Joshua Villanueva**, Kanguk Kim, and Donald J. Sirbuly. "Quantitative mechanical analysis of thin compressible polymer monolayers on oxide surfaces." *Soft Matter* 10, no. 40 (2014): 8001-8010.

FIELDS OF STUDY

Major Field: NanoEngineering

      Studies in NanoEngineering
      Professor Donald Sirbuly

ABSTRACT OF THE DISSERTATION

An Optical Nanofiber Total Internal Reflection Microscopy Platform for

Quantitatively Probing Nanoscale Interactions

by

Joshua T. Villanueva

Doctor of Philosophy in NanoEngineering

University of California, San Diego, 2016

Professor Donald Sirbuly, Chair

Pushing the boundaries of nanoscience and engineering requires the development of sensitive instrumentation for studying small-scale systems and interactions. One of the most fundamental nanoscale phenomena, Brownian motion, remains difficult to characterize experimentally and serves as the primary motivation for developing new tools capable of quantifying the stochastic nature of systems at this scale. The behavior of colloidal nanoparticles are particularly interesting as they are

ubiquitous in nature and are foundational to the field of nanomedicine.

This dissertation discusses the development of an optical nanofiber-based total internal reflection microscopy (TIRM) platform for the statistical analysis of colloidal behavior near a surface. In this technique, the evanescent field surrounding a nanofiber waveguide provides a means for probing the physical interactions between a Brownian nanoparticle and the nanofiber surface. This interaction is quantified optically via the far field detection of an optical signal generated from the light scattered by a nanoparticle in the evanescent field. The accumulation of individual scattering events results in a statistical distribution of distance-dependent intensities that provides information about the underlying state of the system using appropriate physical models. While the technique is simple in principle, characterizing Brownian systems requires a thorough analysis of all parts of the instrumentation process to identify possible sources of error and verify the accuracy of quantitative measurements.

The nanofiber-based TIRM's overall function is verified by comparison with predicted results from a steady-state theoretical model of the Brownian motion of a particle near a surface, mediated by an electric double layer interaction. This analysis identifies practical limitations on the types of colloidal systems that are able to be investigated using this technique. Additionally, further examination of the far-field imaging process reveals that the error in quantifying nanoparticle behavior is directly related to the finite exposure time of the data collection process. With these system limitations in mind, the last part of the dissertation discusses extensions of the platform configuration for advanced characterization modalities.

Chapter 1

Introduction

1.1. Generalized Theory of Instrumentation Development

From an instrumentation perspective, probing the physical world is based on a chain of transduction mechanisms that convert physical phenomena into quantifiable signals. This is what we define as a sensor. In an increasingly digital age the sensor's output often relies on a transduction mechanism that converts an optical [1], thermal [2], mechanical [3], or chemical [4] signal into an electrical one that can be read out by a computer. For advanced instrumentation, several transducers may be coupled together to form a complex tool that can be used to investigate a very specific aspect of a system. In these platforms, each mechanism transforms the signal into another form until a link can be made between the property of interest and the electrical signal that is ultimately quantified. This is exemplified for a general sensor in Figure 1.1.

With all these transduction mechanisms influencing the measured signal, the sensor output is only useful to the extent the entire instrument is properly calibrated. [5–8] That is to say that the specific way of mapping the signal from one form to another needs to be defined for all elements in the transformation pathway. In Figure 1.1. this refers to f(X,Y,Z), g(A), and h(B). If we seek to know (within a desired level of certainty) to what particular system property the final signal read out corresponds, the only way to do so is to fully understand the physical underpinnings of each transduction mechanism. Development of complex sensors requires a detailed analysis of the entire signal transformation pathway because key information concerning the errors and limitations of the sensing platform can often be identified

and localized to specific parts of the transducer chain. From this theoretical understanding of the sensor as a whole, we can develop experimental calibration methods that can be used to verify expected sensor function and thereby bolster our confidence in the exact meaning or interpretation of the quantified signal.

Signal Transformation Pathway
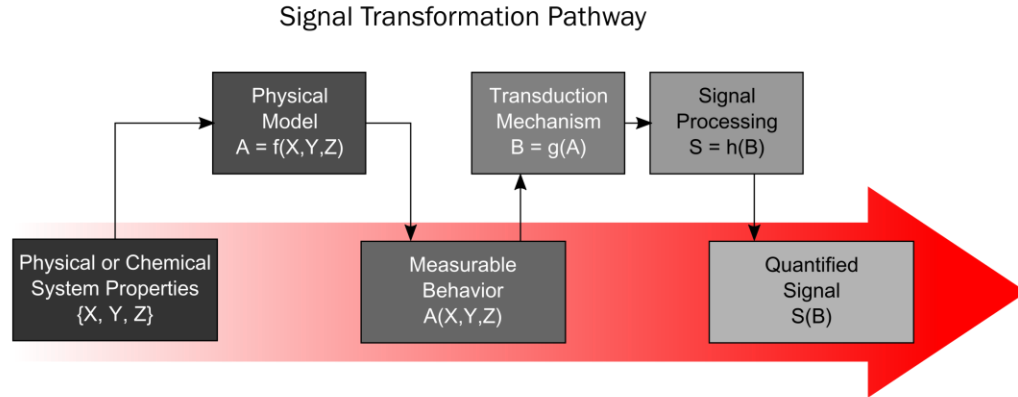
Figure 1.1. Signal transformation pathway. Schematic representation of a generalize instrument workflow**,** quantifying a generic physical phenomenon.

Generally speaking, we can group sensors based on the level of certainty we would have about the quantified signal output. Robust sensors are those that are well-characterized by a signal transformation relationship that correctly describes sensor behavior in a wide set of cases. These sensors typically involve a single transducer element whose behavior is based on intrinsic material properties. Usually these material properties can be controlled and tuned via well-developed manufacturing processes. One example of this is a thermistor whose resistance is mediated by the number of charge carriers in the semiconducting material comprising the sensor, which changes as a function of the temperature. [9] While these sensors have well characterized properties, they often can only be used in a narrow parameter space before their function deviates from a standard calibrated relationship. Additionally,

they are limited in their capabilities and can only characterize the simplest of system properties.

In a research settings, though, novel sensors are constantly being developed to study and characterize a variety of different systems. Often these platforms are comprised of multiple transduction elements that results in a less robust overall sensing mechanism; however, they may still be useful as long as there are calibration technique to empirically map out the overall transduction mechanism. In this case there are often underlying physical details (parts of the transformation pathway) that are either unknown or whose explicit treatment may be too difficult to address or unwarranted depending on the level of accuracy required of the measurement. Moreover, it may be possible also that the manufacturing process of such sensors are not as refined, so while the transduction mechanism is physically understood, controlling the aspects of the system that influence the transducer behavior prove to be challenging.

Related to these novel sensors are tools and instruments where calibration techniques may be very difficult to perform or whose transduction mechanism has no simple analytical form. For these systems extracting meaningful data from a quantified signal additionally requires thoughtful technique design to indirectly access the desired information about the physical system. This can include methods such as signal normalization to a reference or extrapolation of a trend to physically unattainable conditions.

From this general discussion of sensor design, it is apparent that efficient instrumentation development has to innately be an application-centric endeavor. Without an end goal signal to measure, it will be very difficult to define the exact signal transformation pathway. Without this, identifying exactly what types of calibrated relationships are needed then will be challenging. Furthermore, the nature of the calibration may also depend on the required resolution or accuracy of the measurement. So while instrumentation development is an appealing engineering goal, it is an impractical effort to design for generality without first defining a specific application and thereby the signal transformation pathway.

1.2. Colloidal Nanoparticles as a System of Interest

Colloidal particles are a particularly interesting system of research for nanotechnology at the present. They represent a prototypical model system used for fundamental investigations of Brownian motion where the stochastic nature of these systems has captivated researchers concerned with placing order and predictability on the randomness of their motion. [10] Additionally, colloidal nanoparticles are a foundational material for the field of nanomedicine where they are leveraged as minimally invasive diagnostic reporters of the *in vivo* environment or as therapeutic agents to combat disease with a level of specificity previously unattainable. [11–16] From a fundamental perspective, however, the application of simple colloidal systems in nanomedicine is complicated by a lack of understanding of the behavior of these systems in the complex environment of the body. [17–23]

When considering nanoparticle systems, typically we are concerned with characterizing either physical properties of the particles themselves or the various interactions at play in a system of many particles. Physical particle properties include information of size, shape, material composition, and surface functionality. These properties influence the behavior of these system, which can be described by the interaction potential or force among multiple particles, or between particles and another surface. These forces and potentials then dictate how close colloidal particles can get other surfaces. [24] Furthermore, the dynamic nature of Brownian particles is also an aspect of interest, describing how the colloidal system behaves over time. [25–28]

Experimentally, colloidal nanoparticles are a difficult system to study because the scale of the interactions in the system and the dynamics of their transport require highly sensitive instrumentation. Also colloids are a many-bodied system, with characteristics at both the single-particle level and solution-level. Studying these systems requires high spatial and temporal resolution to probe different regimes of behavior. Since all these characteristic properties listed above are interrelated and depend on one another, to fully understand a system, one also needs to have the appropriate theories to relate the properties.

1.3. Dissertation Outline

Our proposed method of measuring the properties of Brownian particles involves the development of a variant of a total internal reflection microscopy technique based on a nanofiber waveguide architecture. Because investigating

Brownian systems requires highly sensitive instrumentation, we must analyze every aspect of the signal transformation pathway with extreme care to ensure that we are quantifying the system behavior in the proper manner. The best way to understand the capabilities of the sensor and the subtle limitations of the technique is to first have a general overview of the system to form an intuition for predicting how the signal will be formed based on different physical colloidal behavior. We will first present a broad introduction to the proposed technique in Chapter 2, then the experimental and image processing details are discussed in Chapter 3 and 4 with thoughtful explanations for specific procedural choices; this is important for developing a robust technique. The quantified results are verified by comparison with a theoretical model for the platform physics in Chapters 5. After verification, further attention is given in Chapter 6 to the details of the far field imaging setup and the subtleties of quantitative microscopy, from which we identify the quantitative limitations of the technique. The last part of the dissertation in Chapters 7, 8 and 9 discusses the extension of the fiber-based TIRM platform in more complicated configurations for advanced characterization techniques. This dissertation is concerned with understanding the signal transformation pathway for the proposed platform, which is a generalization of the instrumentation and technique development process for all nanofiber TIRM sensing platforms. The foundational work presented here serves as an example for identifying key research aspects for novel sensor design, which are particularly important when designing tools and methods for quantifying stochastic, nanoscale phenomena.

Chapter 2

Background on Colloidal Physics and State-of-the-Art Instrumentation

2.1. Qualitative Description of the Brownian Motion of a Particle Near a Surface

We first need to have a basic understanding of the system physics to tell us what we should expect by probing a colloidal system using our nanofiber waveguide platform. From that underlying physical understanding we can assign meaning to collected data if we know how the instrument functions. This will also determine the exact transduction mechanism employed to probe the system. If we have concrete analytical models of the system, then we may be able to back out quantitative information about the system.

Colloidal particles move around in solution due to the random thermal fluctuations of the system. This was observed by Robert Brown with pollen grains in solution, thus it is called Brownian motion. [10] The modern understanding of this random movement is that at any temperature above absolute zero molecules move due to the thermal energy in the system. For a colloid in solution, it is subject to the random bombardment of the solution molecules in all directions. At any instant in time, the net force on the particle from these bombardments is not zero and therefore it causes the particle to move in the direction of the net force. At the next instant in time the magnitude and direction of that force can change based on the new distribution of molecular forces acting on the particle. The higher the thermal energy of the system, the stronger the bombardments become and therefore the further the same particle will move in a given time. Via the fluctuation-dissipation theorem, this mechanism of random movement is also what causes the dissipation of energy (on the macroscopic

scale, it is the root of phenomena like viscous drag and diffusion). [29] This random movement will be the driving transport mechanism for the colloidal particles when we consider a hydrostatic system.

When a colloidal particle is near another solid structure, in addition to the random molecular bombardments from the solution it will also experience an electrostatic force that will influence its movement. [30–32] This electrostatic interaction is due to the charges on both surface, which for like charges prevents the surfaces from getting too close to one another and for opposite charges causes surfaces to come together. Moreover, this interaction is mediated by the presence of ions in solution. Whenever a charged surface is in an ionic solution, an electric double layer forms around the charged surface where the oppositely charged ions accumulate on the surface, effectively screening the surface charges. [33] These ion layers have an ordered structure that gradually decays away to the disordered state of the bulk solution; the characteristic dimension of this decaying ionic structure is called the Debye length. The Debye length is only dependent on the concentration of the ions in solution and not on the charges on the surface. [24] The higher the salt concentration, the smaller the Debye length and the more the surface charge is screened, which means that the surfaces can get closer to one another.

Of course at the nanoscale, nothing is as simple as it seems, and there are other phenomena that arise in more complicated, real world systems, particularly related to near-wall motion of colloidal particles. [34,35] However these two phenomena, Brownian motion and the electric double layer mediated electrostatic interaction,

coupled together form a foundational understanding of colloidal behavior that will inform how we plan to quantitatively study nanoparticle system. These two phenomena are depicted schematically in Figure 2.1. This understanding forms the basis for many different characterization techniques and the mathematical treatment of the two phenomena will be discussed in Chapter 5.
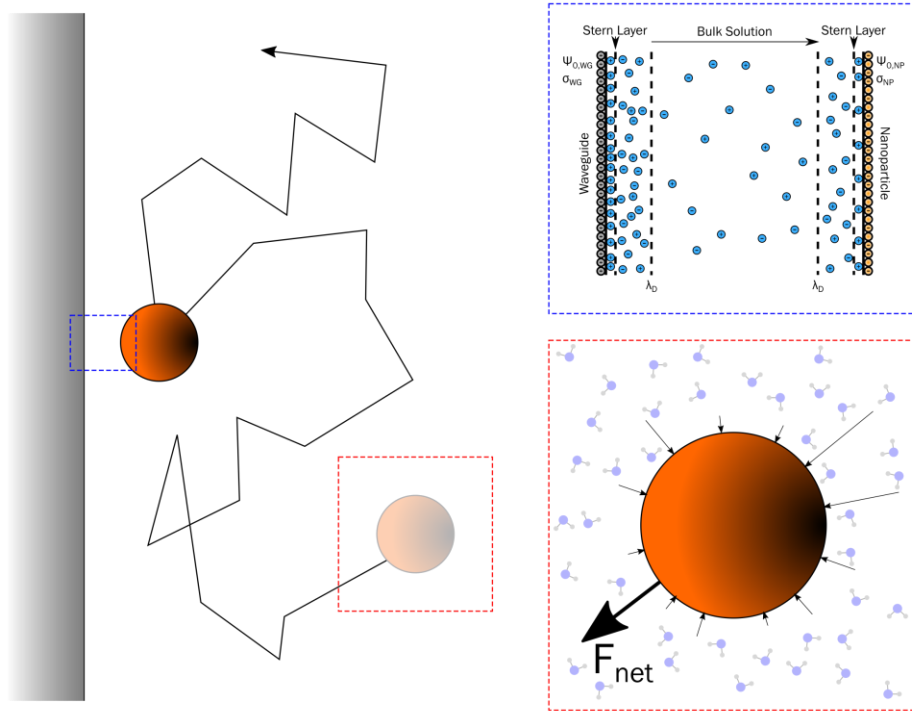
Figure 2.1. Brownian motion of a particle near a surface. Schematic representation of the molecular mechanisms dictating the stochastic motion of a colloidal particle near a charged surface. The red inset depicts an instantaneous state of the system where the distribution of molecules interacting with the particle surface result in a random net force vector. The blue inset shows the electric double layer that forms on a charged surface when there are ions present in the solution.

2.2. State-of-the-Art Characterization Methods

Typically when attempting to experimentally characterize colloidal system and measure the properties discussed in the previous section, the first choice one has to

make is a matter of system scale. Does one want to focus on a single particle or on the multi-particle system? Both perspectives have their own benefits and drawbacks.

2.2.1. Single-Particle Characterization

For the single particle case, the level of detail attainable for characterizing the system is very high and very specific interactions can be probed. Single-particle characterization includes atomic force microscopy (AFM), and trap-based spectroscopy methods like optical trapping or magnetic trapping. [36–41] In these techniques, a particle's position is precisely controlled and it is brought in proximity to a surface, and the forces acting on the particle at a particular distance are measured by modulation of an optical signal that is detected by an imaging sensor. For AFM the particle is attached directly to the cantilever or the AFM tip and the cantilever is moved relative to another surface via a piezo stage. Forces acting on the particle cause the cantilever to deflect and the reflection of a laser off the back of the cantilever is used to measure the deflection via an optical sensor. For optical and magnetic traps, the position of the trap center holding the particle is controlled by the focusing optics of the system or the configuration of magnets. The trap is moved relative to a surface via piezo elements or by changing the focusing of the optical or magnetic setup. The spatial distribution of light scattered from the particle in the trap center is monitored with an optical sensor and when the particle moves out of the trap center due to a force, this spatial distribution changes. The specific relationship between the change in the resulting optical signals and the force is a function of the particular instrument. For AFM, it is the stiffness of the cantilever, and for the optical/magnetic traps it is the

strength of the trapping mechanism (which can also be described as a stiffness). Interpreting how the actual quantified signal is generated from the optical modulation is a separate, non-trivial matter. These techniques are good for direct characterization of static system properties (size, shape, steady-state potential distribution) assuming the appropriate model is known, but they cannot look at the dynamics of a real system, and it is difficult to generate a lot of statistics for obtaining solution-average values of specific particle properties. [42]

2.2.2. Solution-Level Characterization

While single-particle characterization techniques are fundamentally important for understanding the precise electrostatic interactions relevant to the system, solution-level characterization is more practical because very rarely are colloidal particles leveraged in applications as single entities. Dynamic light scattering (DLS) is a standard method for measuring solution-averaged properties of particles suspended in a colloidal solution. [38,43] In a DLS a beam of light is directed through the colloidal solution and the scattering of this light is monitored by an optical sensor on the other end. The modulation of this optical intensity is dictated by the interference of light scattered by multiple particles freely diffusing in the beam path. The way this interference pattern evolves over time is a function of how the particles diffuse through the solution, which can then be related to the physical properties of the nanoparticle. Because many particles pass through the beam of light, the quantified signal can only be related to an average of the individual properties. While DLS is good at collecting information about the state of the system as a whole, it can only

monitor particle movement in the beam path, and therefore cannot look at interactions of particles with a surface. Also, because it is a technique based on interference of multiple scattering sources, anything that scatters light more strongly will be more strongly weighted in the averaging and therefore the technique is sensitive to contamination and the presence of large particles in the solution. This last point is an important limitation of the DLS to be aware of because colloidal solutions are never perfectly uniform; there is an inherent inhomogeneity (with regard to size, shape, surface functionality, etc.) in all batch-synthesized colloidal particle solutions, and solution-average techniques lose that information. [44,45]

Of greater interest is in understanding how the characteristic of the individual particles determine the solution-level behavior of the system. There is a need for other characterization methods that can probe colloidal systems at both levels. Bridging the gap is the technique of total internal reflection microscopy (TIRM). [35,46–48] The crux of the TIRM technique is the ability to sensitively measure distances between a colloidal particle and surface via modulation of an optical signal, much in the same way as AFM or optical traps. However, the primary difference is that the optical modulation is not built around a mechanism used to precisely hold the particle in a certain position (cantilever bending or deviation from trap center), but rather on the optical properties of the surface and medium as an independent transduction phenomenon. For TIRM, the scattering of a nanoparticle within the evanescent field generated at the interface of a total internal reflection (TIR) setup is monitored in the

far field via an optical sensor. To understand this better, the basics of TIR must be explained.

2.3. A Primer on Total Internal Reflection Microscopy

For TIR, two materials of different refractive indices form an interface; in the case of TIRM this is usually a solid-liquid interface with the solid material having a higher index than the liquid phase. Via Snell's law ($n_1 \sin\theta_1 = n_2 \sin\theta_2$) when a ray of light is incident on the interface, the angle of the refracted light ray will depend on the incident angle and the ratio of the refractive indices. When the light hits the interface from the high index medium above a certain critical angle, θ_C, the angle of refraction will be greater than 90 degrees and the refracted light will remain in the first material. Then at the interface, as a consequence of solving Maxwell's equation, there must be an evanescent field that does not propagate in space, but is a standing wave with power that decays away from the interface exponentially. This is shown in in Figure 2.3. [49]

It is this distance-dependent power decay of the evanescent field that is leveraged as the transduction mechanism linking distance with the intensity of light scattered by an object near the interface. However, proper calibration of this scattering intensity-distance relationship is very important. Furthermore, since the relationship that is required is the scattering intensity of a nanoparticle as a function of proximity to a surface, the specific physics involving the scattering mechanism may also play a role in the exact from of the exponential decay. [50] Additionally, as has been suggested previously, the exact method of intensity collection and quantification will

be an important factor in the proper calibration of this transduction mechanism. As with the previously described techniques, the properties of the colloidal system that determine the interaction forces that influence how the particles move near the surface again must be determined using appropriate mechanistic models. A major benefit of TIRM versus the single-particle characterization techniques is that high throughput data collection is more feasible because particles do not have to be individually held in place. The down side though is that it is much more difficult to obtain highly sensitive measurements of individual particle-surface interactions without any positional control because the fact dynamics of the system. Also the experimental procedure must be tuned to ensure the particles will be close enough to the surface for proper imaging.
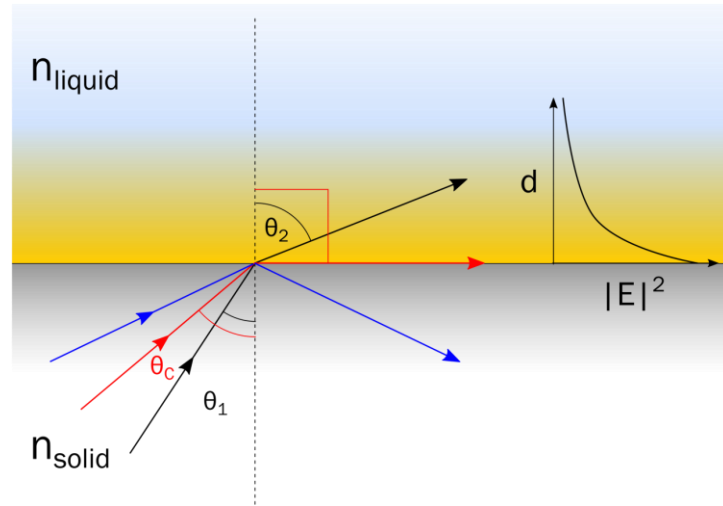
Figure 2.3. Total internal reflection. Schematic representation of total internal reflection. The rays (black) hit the interface from the high index phase and are refracted at an angle determined by Snell's law. Above a critical angle (red), the rays (blue) are refracted at an angle greater than 90 degrees and remain in the high index medium. Under total internal reflection an evanescent wave is generated in the low index medium, which exhibits an electric field power profile that exponentially decays as a function of distance from the interface.

Moreover most TIRM setups do not measure particles in bulk solution, but rather particles that have settled to the bottom of a fluid volume as the substrate acts as the interface. [51] This is not really representative of colloidal behavior in the applications like nanomedicine where particles are constantly interacting with surfaces without settling out of solution. [52] To overcome this, instead of a planar TIR configuration, our platform uses a nanofiber waveguide suspended across a microchannel. The nanofiber geometry allows for all-around sensing, which is not possible with planar TIRM. This technique is like DLS in that we probe in the middle of solution to get the bulk solution dynamics. However, instead of a laser beam we have a physical nanofiber, which allows for separation of the individual particle-surface interactions. This is a major advantage over DLS as building up solution-average properties from the accumulation of individual single-particle measurements results in less sensitivity to contamination by strongly scattering objects in solution. It is this configuration that we hope to probe the true dynamics of colloidal suspensions in a high throughput manner to generate robust solution level statistics that retain information about solution heterogeneity, and also provide both particle property information as well as particle-surface interaction information all in technique. The next chapter will discuss the nanofiber TIRM platform in more detail.

Chapter 2, in part, is currently being prepared for submission for publication of the material. (Villanueva, Joshua, Qian Huang, Gaurav Arya, Donald. J. Sirbuly) The dissertation author is the primary investigator and author of this material.

Chapter 3

Nanofiber TIRM Platform Description

3.1. Technique Overview

A general schematic of the nanofiber-based TIRM platform and experimental setup is shown in Figure 3.1–1. The sensing element of the platform is a single-crystalline tin dioxide (SnO_2) nanofiber waveguide suspended across an etched channel in a silicon oxide (SiO_x) substrate. Similar to traditional TIRM methods, the evanescent field surrounding a waveguiding nanofiber is leveraged to determine fine displacements of a colloidal nanoparticle that moves near the surface of the nanofiber via a distance-dependent scattering intensity signal. The 325 nm line of a helium-cadmium (HeCd) laser is used to couple light in the optical cavity, which is guided down the fiber axis via TIR, thus forming the evanescent field. When a colloidal sample surrounds the nanofiber, light scattered by the nanoparticles in the evanescent field can be monitored in the far field. To collect this scattering signal, a thin glass coverslip is placed on top of the solution, over a thin polydimethylsiloxane (PDMS) spacer, to image the scattering through a flat surface. This full device assembly is imaged using an upright darkfield microscope through a 0.55 N.A. air objective lens (50x magnification) and the far field signal is collected by an electron multiplied charge-coupled device (CCD) camera.

The raw data collected in the experiment is in the form of a video that captures transient scattering events along the length of the fiber as the particles in solution randomly diffuse around the fiber. A processing algorithm must be used to extract quantitative scattering intensity information from the raw data. Then a calibrated relationship between scattering intensity I_S and distance d converts the quantified

signal to a form that can be analyzed using the appropriate physical models. In this way the statistical distribution of scattering intensities collected in the experiment can be used to infer physical properties of the particles in the sample. In this work we consider the physics of the Brownian motion of the nanoparticles as well as the electric double layer interaction described in the previous chapter. Analytical expressions relate the shape of the distance distribution to parameters like particle size, surface charge, and solution ionic strength.
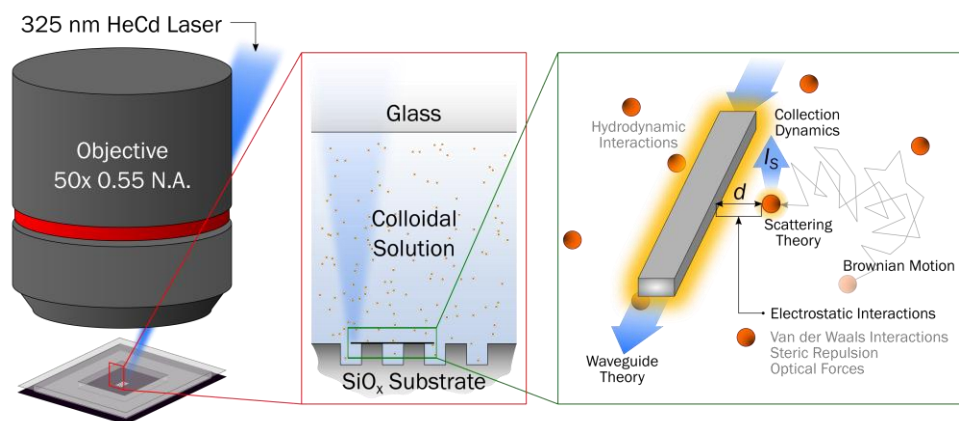
Figure 3.1–1. The nanofiber-based total internal reflection microscopy platform. The experimental setup shown at different scales. The fully assembled device is shown under a microscopy object on the left. The suspended fiber geometry is depicted in the red box, and the relevant device physics is listed in the green box.

The full technique flowchart is shown in Figure 3.1–2 with the basic steps of the signal generation and transformation pathway numbered in order. The end goal of the experiment is to obtain quantitative values for the various physical parameters of the nanoparticle system investigated. However, the accuracy of these values will require considerable work to understand every possible step of the technique that will influence the final parameter estimate. Details of the device fabrication, experimental

setup, data processing, and system physics will need to be analyzed thoroughly to verify proper system function. Subsequent analysis of the limitations of the platform is also necessary to validate the use of the system for probing the behavior of Brownian particles in complex environments.
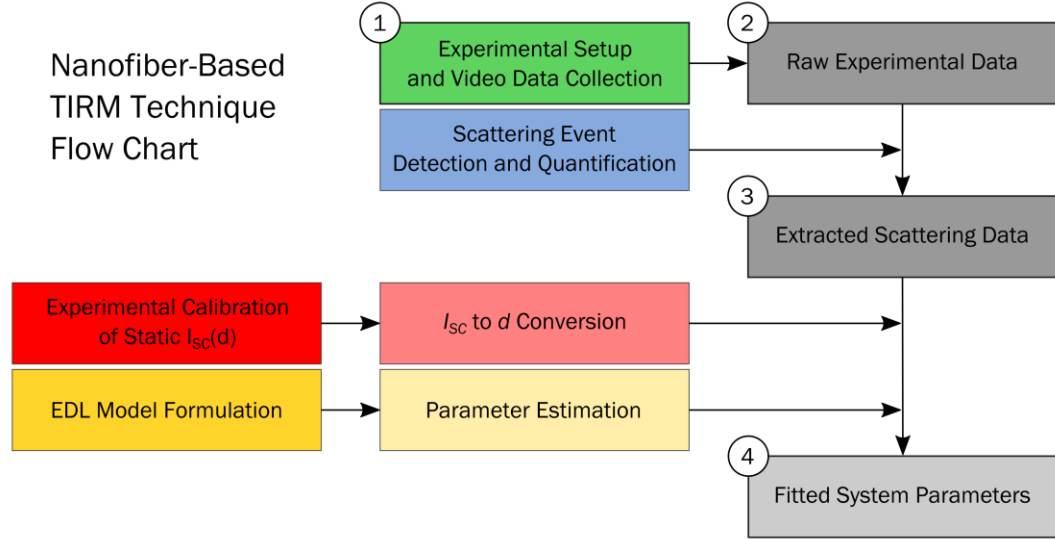
Figure 3.1–2. Technique flowchart. The different aspects of the nanofiber TIRM platform as they relate to the one another in the overall signal transformation pathway. The numbered boxes represent the signal generation and transformation workflow while the unnumbered boxed are details of the signal transformation pathway that determine the accuracy of the quantified signal

3.2. The SnO_2 Waveguide

To get the light into the nanofiber we employ a free space coupling mechanism, focusing the laser directly on the end facet of the waveguide (through the air-glass and glass-water interfaces of the device assembly) without the use of another optical fiber. Usually for waveguides under free space coupling the direct injection of a monochromatic laser line involves very precise positioning of the end facet crystal face relative to the laser beam to achieve proper TIR. [49] However, this is a very

difficult setup to achieve and reproduce because the fibers are so small (cross sectional dimensions on the order of hundreds of nanometers) and the smallest focusing spot of the laser is a spot approximately 20 μm in diameter. Instead, light is generated within a fiber's optical cavity by excitation of the SnO_2 material itself. [53] The 325 nm light ($E = 3.8$ eV) is focused directly on the nanofiber and the SnO_2 is excited above its 3.6 eV bandgap energy. Since SnO_2 has an indirect band gap structure, band edge emission is a very inefficient energy decay process. However, defects (oxygen vacancies) present in the SnO_2 crystal allow for otherwise forbidden transitions by formation of defect states in the bandgap, thus offering another mechanism of energy decay in the excited material. [54] These defect states explain why the light generated in the cavity and seen at the waveguide output has a broad spectrum. The evanescent field surrounding the nanofiber arises as a consequence of the TIR process that guides this light down the axis of the nanofiber

When a colloidal particle is in the evanescent field of the fiber, the intensity of light it scatters is proportional to power of the evanescent field at the particle's position as determined by Rayleigh scattering. Therefore quantified intensity signals give information about the particle's position within the evanescent field if the power spatial distribution is known. In the traditional TIRM technique the evanescent field power decay constant is a function of the refractive indices of the waveguide and surrounding medium as discussed in Chapter 2. For the planar TIRM case the spatial variation of the evanescent field is only a function of the surface-normal distance from

the optical interface, resulting in a one-dimensional relationship between the scattering intensity and distance usually described by a decaying exponential of the form

$$I_s = I_0 \exp\left(-\frac{d}{\tau}\right) \tag{1}$$

where I_0 is the scattering intensity at contact and τ is the characteristic decay constant. [48] For our platform the SnO_2 fibers have a relatively high index n_{WG} of 2.1 and the experiments are performed in aqueous solutions with an index n_{cl} of 1.3. These indexes are the same for all experiments using the SnO_2 nanofibers meaning the decay constant describing the evanescent power change in the normal direction is largely the same. However, for a nanofiber and the all-around sensing scheme we seek to achieve, the spatial distribution of the power at a given distance from the waveguide surface may not be uniform due to the rectangular shape of the waveguide. If the power spatially varies around the waveguide, then the exact scattering intensity profile will be more complicated than a one dimensional intensity-distance relationship. This is exemplified in Figure 3.2. Complicating this further is the wavelength dependence of the scattering intensity as well as the spectral distribution of the evanescent field generated by the sub-bandgap defect emission mechanism of light coupling into the fiber. The slight resonance at bluer wavelengths in the emission spectrum of the waveguide output is evidence of the wavelength dependence of the bound modes of the waveguide with bluer wavelengths exhibiting fewer losses along the fiber. [49]

A major assumption made in the treatment of the TIRM mechanism in this dissertation is that the scattering-intensity relationship for the nanofiber is similar to that of the planar TIRM case. The use of d as a surface-normal measure of particle

proximity implies we assume an angular uniformity of the evanescent decay about the fiber. Therefore we still rely on the form of Equation (1) for describing the relationship between scattering intensity and distance to the fiber surface in the experiments.
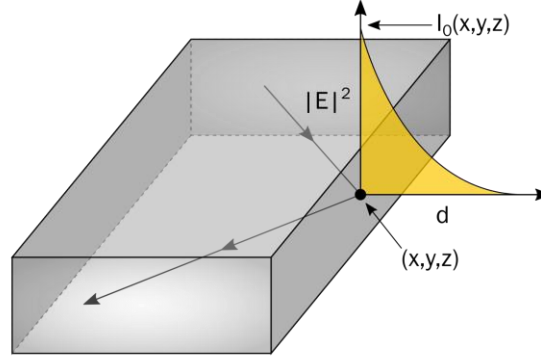
Figure 3.2. Spatial dependence of evanescent field around nanofiber. Total internal reflection results in an evanescent wave whose power decays away from the reflection interface as shown by the yellow graph of the intensity $|E|^2$ as a function of distance from the point (x, y, z) from the waveguide surface. The coefficient of this power decay I_0 is spatially dependent for a rectangular waveguide nanofiber.

Equation (1) describes the overall convoluted distance dependence of the evanescent power decay and the scattering cross section of the particle. Calculating the intensity-distance distribution will be very difficult because the spatial distribution of the waveguide power will depend on the fiber dimensions and composition (influencing distribution of excitable wavelengths in the material by the distribution of crystal defects). Formulating an analytical expression of Equation (1) that includes the physical properties of the system grounded in optical waveguide theory and scattering theory may be too involved for our purposes and still requires experimental determination of those properties themselves. Instead Equation (1) must be

experimentally calibrated. This tool falls in the second category of sensing platforms discussed in Chapter 1. The relationship between parameters must be empirically determined without explicit treatment of the underlying physical mechanism of signal generation.

There are many different experimental methods to accomplish this calibration. In a previous study using the same SnO_2 nanofibers, the scattering-distance relationship was described by a double exponential with two decay constants owing to the additional distance dependence of the plasmon-dielectric coupling of the system. [55] Here however, we consider a simple single exponential profile. While the plasmon-dielectric coupling explains the steeper slope of the measured scattering profile via controlled layer-by-layer polymer deposition, the scattering enhancement due to this effect is only relevant for particles very close to the waveguide surface (within 20 nm), which is not achieved by the freely diffusing particles in the system.

Despite the approximations here and difficulty of the analytical treatment of the system, the fiber synthesis can be tuned to grow more ideal fibers, knowing the physical mechanisms influencing the evanescent spatial distribution and that we want to maximize the overall evanescent power around the waveguide. The single-crystalline SnO_2 nanofibers are synthesized in-house via a chemical vapor transport (CVT) process using a standard benchtop tube furnace. [53,56] In the general process, commercially purchased tin monoxide (SnO) powder is placed in an alumina boat crucible and heated to 1000°C in the center of the tube furnace under a 200 mT vacuum pressure to vaporize the powder. Additionally oxygen (mixed with inert argon

gas to a 0.01% partial pressure) is also flowed into the tube with a flow rate of 25 sccm and is allowed to react with the vaporized SnO to form SnO_2. Under the gas flow this reaction is carried downstream, and at a location in the tube furnace where the temperature has dropped by a certain amount, the vapor condenses to form single-crystalline SnO_2 fibers with rectangular cross sections. Typical fiber dimensions are around 200x400 nm in cross section and 200-300 μm in length. The fibers are chemically robust and highly flexible materials. In this fiber synthesis process, the above values for temperature, pressure, flow rate, and oxygen partial pressure are nominal and can be controlled and adjusted to try to control the fiber dimensions. It is believed that the smaller the nanofiber, the larger the loss and therefore the larger the evanescent power. However, a balance must be achieved because as the fiber becomes smaller, so does its capacity to support a bound mode. If the fibers are too small, they will not be able to guide light down the optical cavity, thus precluding the TIR transduction mechanism.

Once the fibers are synthesized, they must be transferred from the substrate on which they were grown onto another substrate for easier manipulation of fibers under a microscope. They are typically placed onto a silicon oxide (SiOx) substrate via direct contact transfer from the growth substrate. The fibers must be transferred to a non-quenching substrate. Fibers directly on Si substrates without an oxide layer will not waveguide because the laser light will be absorbed by the substrate rather than exciting the oxide material. After the fibers are on the SiOx substrate, fibers with good optical properties must be harvested manually using a 3-axis micromanipulator and

tungsten dissecting probe. This is a tedious process as fibers must be individually separated from an entangled mass and checked one-by-one for good waveguiding properties since the growth of these fibers is not perfectly controlled and there will be a distribution of sizes and lengths.

We check these fibers optically in air by focusing the 325 nm laser line on the end facet, but we only have qualitative properties by which to gauge the appropriateness of each fiber for our device. The first thing to check for is whether or not these fibers guide light by seeing if light is emitted from the fiber end facet after excitation of the SnO_2. If they do not support a fundamental mode, then the fibers will not be good for TIR. To get a gauge on the size of the fibers, we look at the fiber output color. Since we know that the loss of the fiber is wavelength dependent and that the bluer light is more strongly bound within the optical cavity, we look for a blue or green output to tell us that the fiber is small enough to likely have a large evanescent field. This is a rough estimate of the optical properties of the fiber and has not been confirmed with specific evanescent mapping, fiber size, and waveguide output spectra, but it provides a good intuition for the specific fibers we seek for the device. The last property that is important for a good fiber is to have very few scattering centers along the fiber itself. These scattering spots can be due to either physical (surface roughness, step profiles) or chemical (molecular vacancies) crystal defects. Many defects will not be visible under the higher refractive index of water that the experiments are typically run in, but too many will obscure the active sensing area of the fiber and contribute to the background noise of the scattering signals. Conversely, a few scattering defects

along the length of the fiber can be beneficial as indicators of the varying power fluctuation in the fiber (this will be discussed later) and as visual cues to correlate positions along the fiber when comparing different experiments. These aspects must often be weighed on a case-by-case basis, depending on the specific application of the fiber. Because there is no definitive marker of a good fiber, usually, many fibers are harvested and placed on a single device to be evaluated in a preliminary experiment.

After the fibers have been selected for the device, they are transferred to another SiOx substrate where they are positioned perpendicularly across 50 μm wide and 20 μm deep etched channels. This channel suspended configuration is what allows for the all-around sensing scheme. Once positioned, the probe is used to drop PDMS across the ends of the fiber and this PDMS is allowed to cure before using the device. This tacking down of the fibers enables the repeated use of the same fibers (upwards of hundreds of experiments).

3.3. General Experimental Procedure

After the device is fabricated, the experiments are ready to be performed. Here we describe the general experimental procedure for using the nanofiber TIRM to probe the properties of free diffusing colloidal particles in solution. The details of this procedure are important because of the sensitivity required for probing the Brownian motion of the system. The following steps, in order, must be performed prior to each experimental run to ensure that all experiments are reproducible and performed in the same manner, enabling the proper correlation of measured signal with physical system attributes.

3.3.1. Device Cleaning

The disassembled device (no coverslip, no PDMS spacer) was cleaned before each experimental run to ensure a consistently charged nanofiber surface, facilitating comparison of different datasets. The procedure is as follows. A diluted piranha solution (3:1 sulfuric acid to hydrogen peroxide, diluted with an equal volume of deionized water) was pipetted (glass pipette) onto the device and allowed to soak for 3 minutes. Immediately after the entire device was placed in a fresh deionized water (DI) bath for 3 minutes, then dried with compressed air. Aqua regia (3:1 hydrochloric acid to nitric acid) was then pipetted onto the device and allowed to soak for 3 mins. The entire device was again placed in a fresh DI bath for 3 minutes and subsequently dried with compressed air. After the aqua regia cleaning, the device was placed in an oxygen plasma cleaner for 5 minutes on the high setting (~ 30W RF power) at a base process pressure of 200 mT. Oxygen plasma cleaning standardized the surface groups on the nanofiber for each experiment. It also made the surface hydrophilic, which inhibited the trapping of microbubbles in the etched channels and near the fibers during sample preparation and final device assembly.

3.3.2. Colloidal Sample Preparation

Commercially available 80 nm, 100 nm, and 150 nm gold nanoparticles stabilized in a citrate solution (Sigma Aldrich) were washed using the following procedure to ensure ionic concentrations were comparable during different experiments. First, 100 μl of the nanoparticle solution was added to an Eppendorf tube with 900 μl of DI. This solution was mixed for 10 sec using a vortex mixer and then

placed in a centrifuge and spun at 7500 RPM for 5 min. After centrifugation, the 950 μl of the supernatant were discarded and replaced with 950 μl of fresh DI. Vortex mixing, centrifugation, and removal of supernatant were repeated for a total of 3 times. The remaining 50 μl of washed gold nanoparticles were sonicated for 10 sec to redisperse the colloid and this prepared sample was kept at room temperature for the duration of the experiment (2-5 hours). The 80 nm DNA-coated gold nanoparticles were washed and prepared in a similar manner. These particles were synthesized from commercially purchased bare gold nanoparticles (Ted Pella, Inc) and characterized using a previously described method. [56]

A stock solution of 10x phosphate buffered saline (PBS) was prepared according to previous methods and adjusted to a pH of 7.4 using hydrochloric acid. [57] For experiments varying ionic concentration, a serial dilution of the 10x PBS stock was performed using fresh DI to obtain final solutions of 0.1x, 0.075x, 0.05x, 0.01x, and 0.005xPBS. The final step in preparing the colloidal solution for testing was to add the washed nanoparticle solution to the PBS solution. This final solution was only prepared immediately before data collection to avoid flocculation of the nanoparticles. The prepared nanoparticle solution was sonicated for 10 sec, then 4 μl of this solution were added to 30 μl of the prepared PBS solution. After vortex mixing, 30 μl of this final prepared colloidal solution were placed on the device as described previously.

3.3.3. Experimental Setup and Alignment

First the nanofiber was imaged through the eyepiece in darkfield mode and focused by eye under the 50x objective, then the darkfield illumination was then turned off and the beam block removed to view the focused spot of the laser. This spot was positioned on or near the end facet of the waveguide, which resulted in scattered light to be seen coming from the nanofiber output (typically green-blue in color). The device was then rotated and translated on the stage (the focusing spot of the laser was also repositioned accordingly) until the output of the waveguide was maximized and the background scattering minimized.

Once this device orientation was determined, positioning guides were taped down on the microscope stage to aid in fast and consistent orientation of the nanofiber relative to the laser beam for every experiment. Additionally visual markers were noted (e.g. edge of channel aligned with horizontal bar of eyepiece crosshair and length of waveguide oriented along vertical crosshair bar) after imaging the positioned waveguide in darkfield mode for consistent translational alignment of the nanofiber under the objective.

After positioning of the device on the microscope was done, the laser was focused further with the aid of the Andor Solis program (version 4.22.30005.0), which was used to collect the video data. First the CCD was physically rotated on the microscope to align the waveguide axis perpendicular to the pixel shift axis. Then the 512 x 512 pixel field of view was cropped to a tight subarea just around the waveguide that includes the waveguide output, but not the laser focus at the waveguide input,

typically about 330 x 20 pixels. This alignment enables the fast frame rate of the camera in frame transfer mode. The darkfield illumination was then turned off and the output scattering signal was the only signal seen by the CCD in live view video mode. In the Andor Solis program, the center of the waveguide output was selected and the pixel profile in the vertical and horizontal dimensions were seen on the program as shown in Figure 3.3 below.
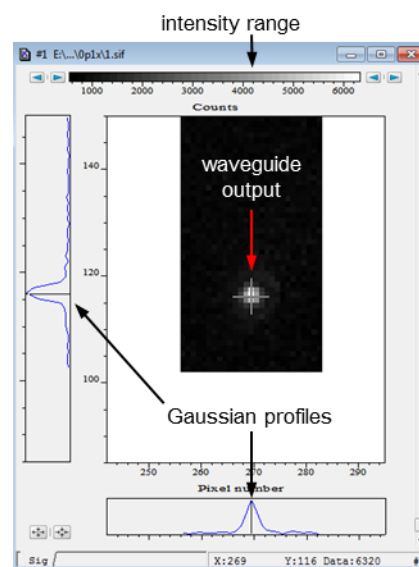
Figure 3.3. Selection of waveguide output in the Andor Solis program. Intensity profiles shown on the left and bottom of the image corresponding to the location of the cross hair.

The data histogram was then locked to a specific intensity range (top grayscale bar in Figure 3.3) and the laser focusing knobs as well as the fine focus knob of the microscope stage were incrementally and repeatedly adjusted to maximize the peak value of Gaussian intensity profiles of the output. The procedure was repeated periodically between video collection to ensure consistent laser focusing and maximize coupling efficiency into the waveguide for every experiment.

The video data was collected using the frame transfer mode of the CCD, which is why the length of the waveguide had to be oriented a certain way relative to the CCD sensor and the image area must be cropped tightly around the waveguide. Typically videos are collect in 20k to 40k frame increments up to a total of between 80k to 240k frames of video for one experimental run. This translates to about 20 minutes of data collection depending on the exposure time of the experiment. Typical experiments are collected at a frame rate of about 190 Hz for a 5 ms exposure time with the gain set to 200. All other settings were left on the program default. With all these details defined in the experimental procedure, we have established a means of confidently comparing datasets with the knowledge that the variables under investigation are the ones being probed if the rest of the experimental setup is the same.

Chapter 3, in part, is currently being prepared for submission for publication of the material. (Villanueva, Joshua, Qian Huang, Gaurav Arya, Donald. J. Sirbuly) The dissertation author is the primary investigator and author of this material.

Chapter 4

Data Processing Algorithms

4.1. Event Detection

Once the raw data is collected, it must be processed to extract the quantitative scattering signals that will provide information about the solution-average interaction between the particles in the sample and the nanofiber surface. The data is in the form of a video that can be thought of as a 3D stack of 2D images. An example collected data frame is shown in Figure 4.1–1 with the corresponding darkfield image of the fiber next to it. The scattering from the waveguide output is always collected with dataset (for reasons to be discussed in the following chapter), and the experimental setup always has the waveguide output located at the bottom of the collected frames. A scattering event is depicted as a 2D bright spot on the image. This bright spot is from a diffraction limited scattering source, therefore its profile is an airy disc pattern that can be approximated as a 2D Gaussian. The peak of the Gaussian profile is equal to the scattering intensity.

For these experiments, the scattering events only occurs along the region of the fiber suspended over the channel because the portion of the nanofiber on the substrate is covered by a thick layer of the tacking PDMS. This prevents the particles from getting close enough to the fiber surface to scattering light from the evanescent field. Over the channel, the background noise of the image is seen to be clearly elevated compared to the other parts of the image. This noise is due to scattering of the free space coupled laser or the ambient light of the lab off the channel walls and is unavoidable. The scattering event is overlaid on top of this background noise. The processing of this data to get a quantitative value for the scattering event is done in

three steps: event detection, signal quantification, and noise filtering. The detection

algorithm will be discussed first where the scattering signals will be systematically

distinguished from the background noise according to a threshold intensity value.
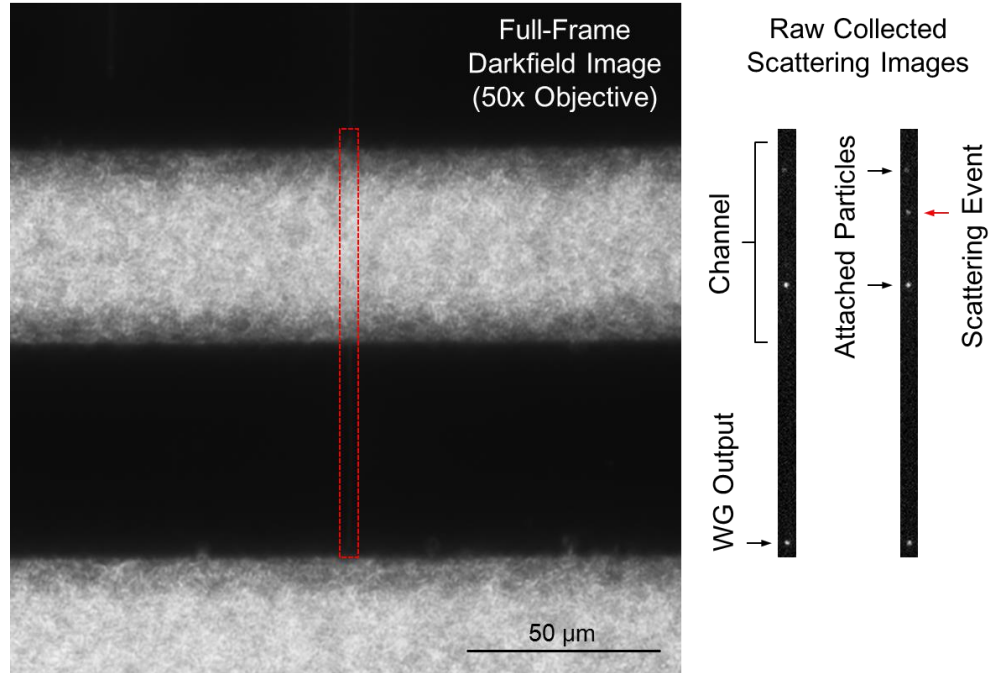
Figure 4.1–1. Example raw collected data. Two consecutive cropped video frames collected from an experimental run are shown alongside the full-frame darkfield image of the fiber in the experimental setup. The waveguide output is the large scattering signal at the bottom of the image; nanoparticle scattering events only occur on the section of the fiber suspended across the substrate channel. Attached particles are identified by their persistent scattering while freely diffusing particles are marked by their transient scattering.

Detection of the scattering events essentially involves localizing the events in

space and time. This is processing is required for these datasets where freely diffusing

particles move in and out of the evanescent field because the scattering events are

transient and can occur at any position along the fiber over the channel. For detecting

the scattering events, a basic 1D contrast method is used. The overall schematic of the

algorithm process is shown in Figure 4.1–2. This method required that the input data was a vector of pixel values and that we input a threshold value to discriminate the desired signal from the background noise. To transform the data into a vector form we averaged the pixel values across the width of the waveguide in each video frame and worked with the video dataset as a time-varying intensity profile along the length of the waveguide. This enabled us to use the *findpeaks* function in MATLAB while retaining the spatial and temporal information of the scattering event. Processing the data in this way acted as a rough noise filter that reduced many of the small, high-frequency fluctuations in the pixel intensity along the length of the WG. However, the averaging of pixels also resulted in a minor loss of information, namely the scattering position in the transverse-waveguide direction (which is mostly localized within 3 pixels of the center of the waveguide) as well as the possible elimination of very small (low intensity) scattering events.
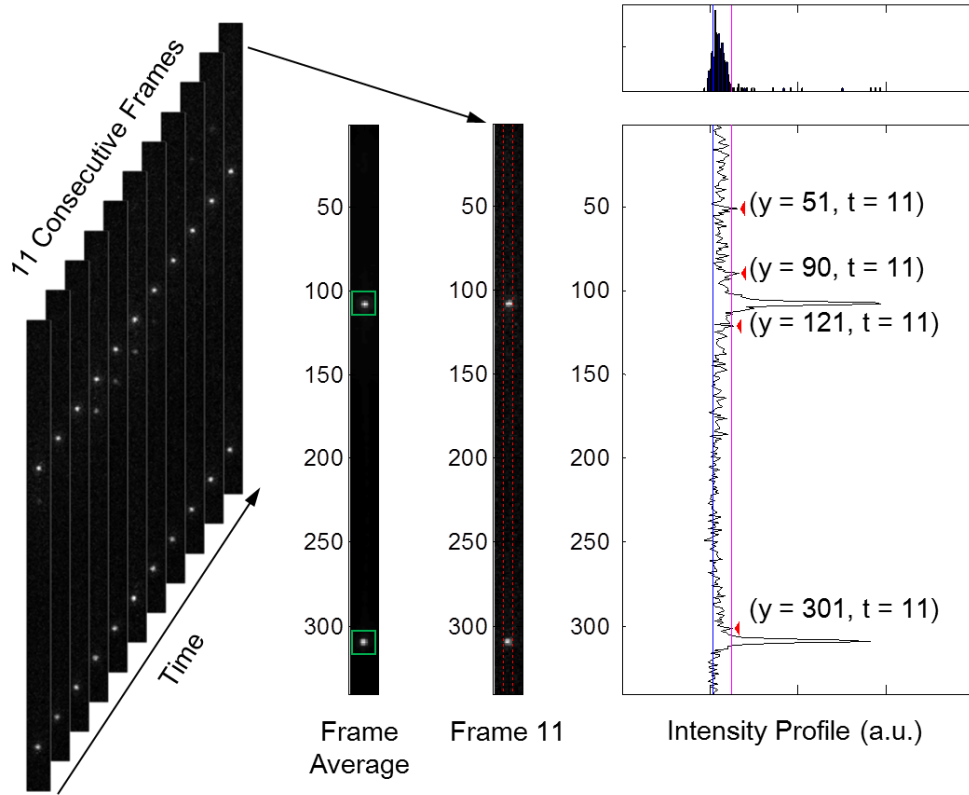
Figure 4.1–2. Diagram of detection algorithm steps. Raw data is processed in a frame-by-frame manner where persistent scattering is ignored and only transient scattering events are detected. The 2D frame image is collapsed to a 1D scattering profile along the fiber and the distribution of profile intensities (top histogram) is used to determine the thresholding parameter to identify scattering events.

Determination of the threshold value was not trivial as this dictated how much noise we collected in our data processing (and also influenced the speed of running our program). Selection of a single threshold value was not desirable because one number was not able to account for the background of the entire dataset, which would have resulted in the detecting many noisy pixels in some parts of the video dataset and possibly missing good data in other parts of the video. To understand this, we considered the form of the noisy background in our collected video. Because of the

free-space coupling of the laser into the nanofiber, slight fluctuations in the power of the supported modes in the waveguide resulted in a temporally fluctuating average background noise level. Also, as noted earlier, the scattering from the channel edges contributed to a spatially varying noise level, with more background noise in the pixels over the channel (primary sensing region) compared to the area of the image near the nanofiber output. Because we do not know *a priori* where and when the scattering events will occur, this presented a major problem for the accuracy and efficiency of processing our data.

Calculating an ideal threshold value from which to distinguish the scattering events required first flattening the spatially and temporally varying background noise and then calculating the threshold value based on the distribution of background pixel values in in each image. To accomplish this, the individual frame intensity profiles were plotted in sequence to form a two-dimensional image of the entire video dataset with the y-axis representing the spatial positon along the length of the waveguide and the x-axis the frame (or time) of the collected intensity profile. This spatiotemporal image of the video dataset was processed using a tophat filter that flattened the background of the entire image, effectively accounting for the temporally and spatially varying background in a single step. From this flattened image, we calculated the threshold value for each video frame from the distribution of pixel values in each flattened intensity profile, which was generally Gaussian distributed. The threshold value was calculated by summing the mode pixel value M plus one standard deviation of the distribution of pixel values S.

$$Thresh = M + S \tag{2}$$

This is effectively determining the detection threshold based on the noise of the collected dataset, which is a more dynamic means of event detection rather than setting an arbitrary, constant threshold for the entire dataset. The mode value was used rather than the mean pixel value because the presence of scattering events skews the Gaussian distribution of pixel values towards higher intensities, which would affect the mean value. Using this threshold value in the peak finding algorithm resulted in identifying the location of brightest intensity for each identified scattering event.

Efficient detection of the scattering intensity from the data employed processing the flattened 2D image using the 1D peak finding algorithm and cross-referencing the detected intensity peaks in both the spatial and temporal dimensions. After identification of the scattering signal at a certain position along the waveguide in each frame of the dataset (profile-by-profile peak finding along x-axis of the 2D image), we independently identified the time of the scattering events that occur at each pixel position along the waveguide (profile-by-profile peak finding along the y-axis of the 2D image). We again calculated a threshold value using the method described above, but calculated the values for the distributions of pixels associated with a specified positon along the waveguide for the entire duration of the collected video dataset. After both datasets were collected, only scattering events that were detected independently both along the time and y-spatial axes were preserved for intensity quantification. In this cross-referencing scheme, the scattering of a single particle over

multiple frames is not counted as multiple events, but rather the brightest intensity is identified and counted as a single scattering event.
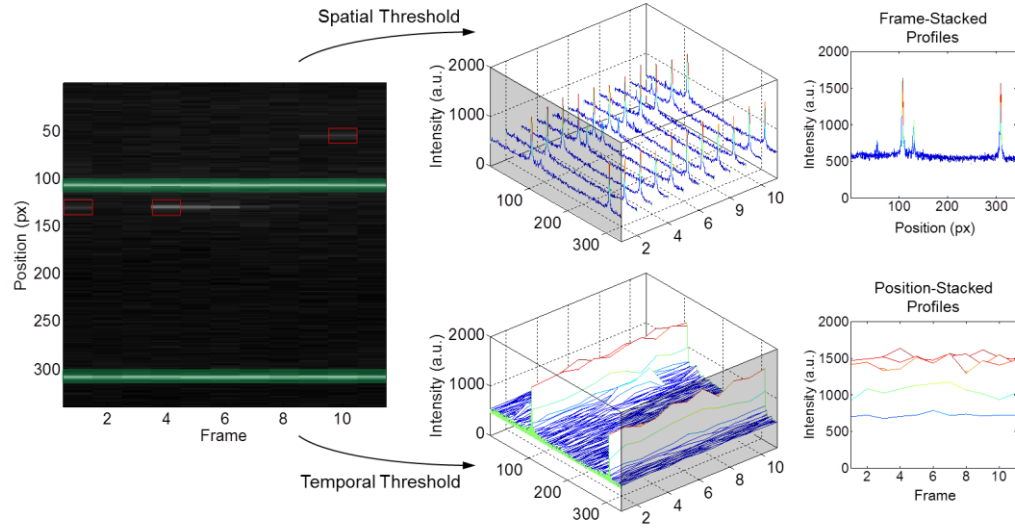
Figure 4.1–3. Signal cross-referencing in space and time. Scattering events are localized in a two-part detection scheme, thresholding against a background signal in both space (top row) and in time (bottom row). Independently detected events that are localized to the same pixel and frame are counted as true signals (red boxes) in left image. Temporally constant scattering events are not detected in the temporal threshold scheme and ignored (green boxes).

To localize the signal in the transverse-waveguide spatial dimension (along the x-axis), we took a similar peak finding approach. For an identified scattering event frame, we took the subset of raw data within 3 pixels of the identified position of a scattering even and averaged this sub-image along the axial length of the waveguide. The peak finding algorithm was used to identify the position of highest intensity for this scattering event, using the same threshold value calculated for identifying the scattering event spatially in this frame. Once localized in both spatial dimensions and

in time, the peak intensity value was readily obtained from the raw video data as described below.

4.2. Quantifying Scattering Intensity

4.2.1. *Peak Intensity Method vs Integrated Intensity Method*

Once the scattering events are localized in space and time, the raw pixel value corresponding to the identified frame and x- and y-coordinate is simply taken as the scattering intensity of the signal. The value of this pixel is a measure of the charge generated at that point in space as the photons from the nanoparticle scattering hit the image sensor in the far field. The charge is proportional to the number of photons collected at that pixel during the exposure time of the image collection corresponding to the time the aperture of the camera is open.

Here it is worthwhile to discuss our choice of quantification, what we term the "peak intensity" corresponding to the maximum value of the 2D Gaussian profile for the scattering event, that differs from most other processing techniques that integrate (sum) all the pixel values over a localized region of interest (ROI), which will be referred to as the "integrated intensity". The primary difference in the two methods comes down to the associated error of the quantified signal, which depends on the detection algorithm and the form of the collected data. The integrated intensity offers the benefit that the resulting calculated intensity is far less susceptible to random pixel fluctuations associated with the noise of the CCD and errors associated with localization of the peak pixel of a scattering event. However, a challenge of the

integrated ROI method lies in determining the appropriate ROI size to integrate over as well treatment of the integrated background noise.

We can consider this integrated error using our approximation of the imaged Airy disc pattern of a scattering event with a symmetric 2D Gaussian overlaid on top of a noisy background. A perfect integrated intensity, I_{ROI}, quantifies the intensity of a scattering event as a volume of the 2D Gaussian, $V_{2DGauss}$, that is proportional to its peak height, I_{Pk}, according to the equation for the volume of a 2D Gaussian

$$I^*_{ROI} = V_{2DGauss} = 2\pi I^*_{Pk}\sigma^2 \tag{3a}$$

where σ is the standard deviation of the symmetric Gaussian and the asterisk indicates the ideal quantified value. For the actual quantified signals, our peak intensity method has an error, ε_{Pk}, that is associated with the background scattering, pixel shot noise, and charge bleed that occurs in high speed CCD imaging.

$$I_{Pk} = I^*_{Pk} + \varepsilon_{Pk} \tag{3b}$$

The real integrated intensity will have a background noise error, ε_{bkgd}, associated with it also

$$I_{ROI} = I^*_{ROI} + \varepsilon_{bkgd}, \varepsilon_{bkgd} = \sum_{ROI} \varepsilon_{Pk} \approx A_{ROI}\overline{\varepsilon_{PK}} \tag{3c}$$

where ε_{bkgd} is equal to the sum of all the individual pixel errors in the ROI, which can be approximated by multiplying an average per-pixel noise value for the image, $\overline{\varepsilon_{PK}}$, with the area of the ROI, A_{ROI}. The mode value, M, from Equation (2) can be used as a rough measure of $\overline{\varepsilon_{PK}}$.

The integrated background noise minimizes the shot noise error of the calculated signal, but significantly increases any noise associated with the

accumulation of charge on the CCD sensor (i.e. fluctuating error about a mean is minimized, but offset noise is amplified). Therefore, for the integrated intensity method, a background subtraction is often necessary. As with any quantitative microscopy technique, determination of this noise is a nontrivial matter. Typically, an average background value per pixel is calculated for the image frame, multiplied by the integration area, and then subtracted from the integrated intensity value. However, due to the spatially varying quality of the background noise as previously described, it is difficult to obtain an accurate value for the average pixel noise of a frame. Therefore large offset errors result in trying to quantify the scattering intensity using the ROI integration method for the datasets associated with our fiber-based TIRM technique. This is exemplified by plot in Figure 4.2 where the same, real data is quantified using both the peak intensity and integrated ROI intensity method.
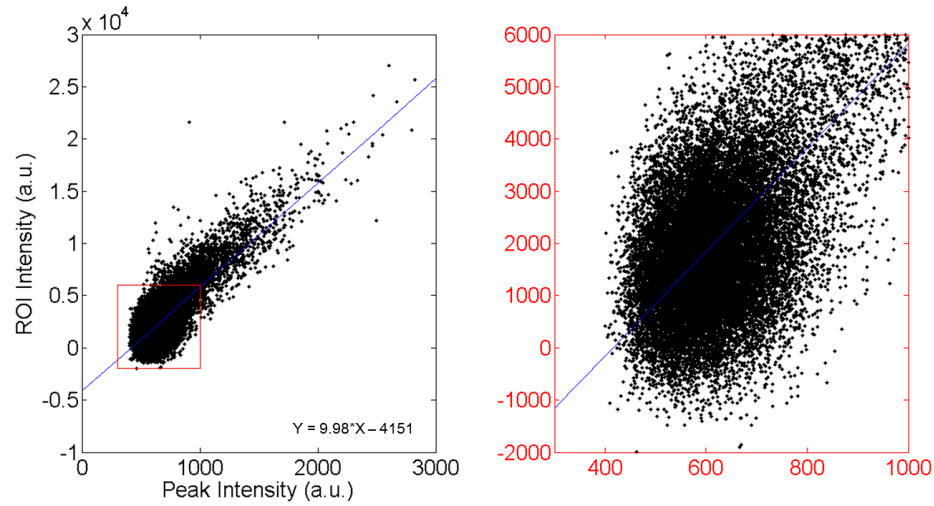
Figure 4.2. Integrated region of interest (ROI) intensity vs peak intensity of unfiltered dataset. Right graph (zoom-in of red box in left graph) shows high density cluster of detected noise. Blue line is linear fit of scatter plot data.

The linearity of this trend validates our assumption that the scattering signal can be approximated as a 2D Gaussian as the volume of a 2D Gaussian is linearly proportional to its peak value. The negative y-intercept of the scattering plot shows that the mode pixel value method for calculating the integrated background overestimates the error. If this error was consistent across all datasets this would not be an issue for comparison, but as the background noise may be different between experimental runs, this poses a problem for comparing different datasets. Therefore the peak intensity method is preferred with only a minor offset error due to background scattering.

The previous discussion concerned the noise associated with each quantification method, and due to the spatially varying quality of the collected dataset, it was determined that the peak intensity method resulted in less overall error in the quantified intensity distribution. However, the linearity of the data in Figure 4.2 and Equation (3a) can provide insight on ways to improve the ROI integration method. This analysis, while still not idea for the dataset at hand with error due to the spatially varying background, is applicable to other datasets where the scattering signal may be localized to a single area (see Chapter 8) and therefore worthwhile to discuss here.

Until now, we have not considered the effect of the ROI size on the error of the quantified signal. In most instances, the ROI size is arbitrarily determined. However, since we know that the integrated background error is proportional to the integration area by Equation (3c), one way to improve the ROI integration method would be to minimize the ROI size to as tight an area around the scattering event as possible. The

question is then, by what means are we going to define the appropriate ROI area? If we again consider the dataset as a 2D Gaussian overlaid on a noisy background, we know that any pixel data integrated beyond the width of the Gaussian that falls below the noise will significantly contribute to the offset error. Therefore, what we aim to do is define the ROI size based on the noise level of the data. We can do this by considering the equation for the full-width-at-half-maximum (FWHM) of a 1D Gaussian

$$FWHM = 2\sqrt{2 \ln 2}\, \sigma \tag{4a}$$

where the 2 in the natural logarithm comes from the fact we are calculating the width at half of the height of Gaussian peak. If we want to set the ROI size (width of a square) to the full width of the scattering intensity peak at the background noise level, then we simply replace the 2 in the logarithm by the signal-to-noise ratio (SNR) where the SNR would be the peak scattering intensity (Gaussian maximum) divided by the mode pixel value, M.

$$\text{ROI Size} = 2\sqrt{2 \ln(SNR)}\, \sigma, \; SNR = \frac{I_{Pk}}{M} \tag{4}$$

The standard deviation can be determined empirically from a calibration dataset similar to that in Figure 4.2 where σ can be calculated from the slope of the linear fit by Equation (3a). For the specific data in Figure 4.2, $\sigma = 1.26$. For the value of the SNRs, that will depend on the specific scattering event. However, for the dataset in 4.1 the SNR varies from about 1.15 at the low end (M values typically about 350 counts) to as much as 8.6 for bright scattering events calculated from the peak scattering intensity range shown along the x-axis. Therefore the ideal ROI size for these

scattering events is between 1 and 4 pixels (rounding to the nearest whole pixel). This ideal ROI size is small and further justifies the use of the peak intensity method, which is equivalent to the ROI integration over 1 pixel (without background subtraction). As the SNR increases, the ideal ROI size will increase more slowly according to the radical, but it is expected that σ may also increase as well. Regardless, for low SNR datasets Equation (4) can be a useful method for improving the ROI integration method to minimize integrates noise in the signal.

4.2.2. Intensity Normalization

The last part of the signal quantification procedure involves normalization of the scattering events signals. Intensity normalization is necessary because the fluctuations in the non-normalized scattering signal are not necessarily only due to changes in nanoparticle position, but also dependent on the power of the evanescent field as discussed in Chapter 3. The latter effect must be decoupled from the former to improve the accuracy of the conversion of intensity to distance. For the experimentally collected datasets we normalize to the waveguide output because the output signal changes with the guided power in the waveguide and therefore the evanescent power. Fluctuations in this output intensity signal are Gaussian distributed as a result of many different noise sources including fluctuating laser power, positional movements of the laser focusing spot relative to the waveguide end facet, and the scattering of the light from the beam path of the laser from nanoparticles as it passes through the colloidal solution.

Because the scattering from the output is spatially localized and persists for all frames of the dataset, detection and quantification of the output intensity is more straightforward. Spatial localization of the scattering event in each frame is determined using the peak finding algorithm as described in the previous section. The quantification method for the output signal is the same as that used for the scattering events, the peak intensity method. The implications of the normalization on the meaning of the quantified intensity will be discussed further in Chapter 5.

4.3. Data Filtering

After the data has been detected and quantified, we need to know if the processing was accurate. Did we detect all the scattering events in the dataset? Are all the detected events true events or did we incorrectly identify some noise? Did we quantify the signal correctly? In order to judge the extracted data, we must first establish an intuition for what to expect the data to look like. We base this off of our general understanding of the physics of the colloidal physics described in Chapter 2, the TIRM mechanism of operation in Chapter 3, and other experimental TIRM work done by other groups.

4.3.1. Expected Form of the Data Distributions

From the foundational work on traditional planar TIRM systems done by Prieve, [58] we know that the quantified scattering intensities will form a distribution that can be converted to a distance distribution using Equation (1). This experimentally measured distance distribution is effectively the probability density function (PDF) of the system. If we assume the system follows a Boltzmann

distribution where the PDF (here denoted as P) is proportional to the exponential of the negative of the system energy, $U(d)$, relative to the thermal energy, $k_B T$, where k_B is the Boltzmann constant and T is the system temperature

$$P(d) \propto \exp\left[-\frac{U(d)}{k_B T}\right] \tag{5}$$

then the experimentally measured $P(d)$ can be inverted to determine the physical system properties if an appropriate model incorporating these properties is used for $U(d)$. However, this accuracy of this analysis is strongly dependent on the accuracy of the I_S–d calibration.

To work directly with scattering intensity distributions instead of the distance distributions, we can use the transformation described by Prieve. His assumption was that the number of particles described by a given intensity interval should be equal to the number of particles in some other distance interval. The total number of particles described by an arbitrary interval on the PDF of a system is the integral of the PDF between the interval bounds. In a small interval, the number of particles is described by the differential interval width times the value of the PDF at some intensity value within the interval. For the above relation between the intensity and distance PDFs, a given number of particles, N, is given by

$$N = P(I)\Delta I = P(d)\Delta d \tag{6a}$$

where $P(I)$ is the PDF of the collected intensity, $P(d)$ is the PDF of the particle distances, and ΔI and Δd are the differential PDF interval widths for an intensity distribution and distance distribution, respectively. Rearranging Equation (6a) in the limit of a infinitesimally small interval widths we get

$$P(I) = P(d)|I'(d)|^{-1} \propto \exp\left[-\frac{U(d)}{k_B T}\right]\left[\frac{\tau}{I_0 \exp\left(-\frac{d}{\tau}\right)}\right] = \left(\frac{\tau}{I_0}\right) \exp\left[\frac{d}{\tau} - \frac{U(d)}{k_B T}\right] \quad (6b)$$

where we plug in Equation (5) for $P(d)$ and the quantity $I'(d)$ is the absolute value of the first derivative of the intensity-distance relationship calculated using Equation (1). While the exact values of τ and I_0 are still required for Equation (6b), the general qualitative form of the intensity PDF based on the system physics can be inferred from an analysis of limiting cases.

From Equation (1) we know that as the Brownian particles get close to the waveguide surface they will scatter more light; at the same time we qualitatively know that the electrostatic interaction between the particle and the surface increases for a repulsive interaction. For the purposes here, we can assume that the energy term of Equation (5), $U(d)$, is itself a decaying exponential to describe the increasing electric potential of the system as the particle gets closer to the waveguide surface (we restrict our discussion here to purely repulsive electrostatic interactions). This results in a sigmoidal form of the distance PDF. This shape makes sense as the closest the particle will get to the fiber is dictated by balance between the thermal energy of the system and the electrostatic interaction between the surfaces. When the electrostatic potential decays to zero at large distances from the fiber, the surface charges on the fiber no longer have an influence on the diffusing nanoparticle and therefore the relative probability distribution should be constant. The closer the particle gets to the fiber surface, the larger the electrostatic potential, thus the probability of finding a particle as the particle's proximity to the waveguide decreases should also decrease, eventually going to zero.

The high intensity edge of the scattering intensity histogram drops off to zero corresponding to the decrease in the distance PDF with decreasing distance. The low end of the intensity histogram corresponds to where the distance PDF is constant representing the bulk nanoparticle distribution of the system. From Equation (1) we know that the exponentially decaying intensity-distance relationship goes to zero at large distances from the waveguide. Consequently, all the detected particles in the bulk will results in a large accumulation of very low intensity scattering events in the ideal case that should result in the intensity PDF going to infinity as the intensity decrease. Figure 4.3–1 shows example intensity and distance distributions (solid line) calculated from Equations (5) and (6b) to exemplify these trends.
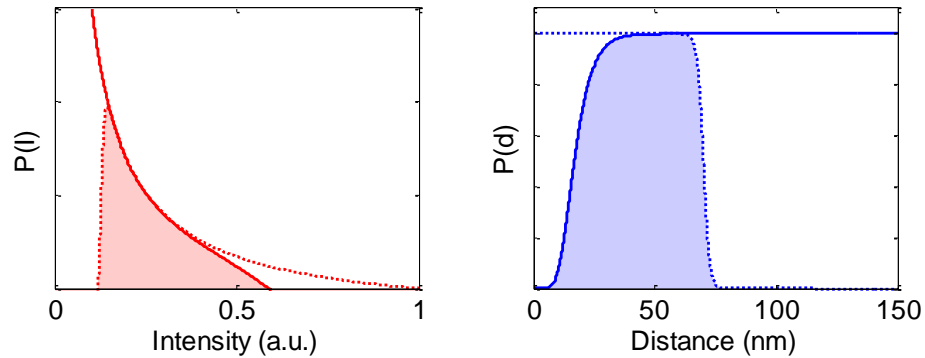
Figure 4.3–1. Example theoretical intensity and distance distributions. The left plot shows an example intensity distribution (solid line) calculated from Equation (6b) based on the distance distribution (solid line) on the right calculated from Equation (5) where the form of the potential $U(d)$ was assumed to be a decaying exponential. The dotted line represents a hypothetical sensitivity cutoff of the nanofiber TIRM system. The area under both curves represents the expected experimentally obtained distributions.

As will be seen experimentally, though, the quantified intensity PDF obtained using the nanofiber TIRM platform goes to zero for low intensities, not to infinity. For planar TIRM setups, this behavior is also exhibited. In the traditional TIRM case, this

is explained due to an additional gravitational component to the potential profile, which keeps the particles near the TIR surface. Rather than a simple decaying exponential, these profiles have the form of a decaying exponential plus a linear curve corresponding to the gravitational potential. The decay is due to the thermal energy of the particles not being able to overcome the gravitational potential at large distances from the TIR surface. The balance of the electrostatic and gravitational potentials forms a potential well that the particles will tend to settle into for the planar TIRM case.

For our system, since we allow for all-around sending, the effect of the gravitational potential is minimal. In fact, considering all radial positions a particle can sample around the waveguide and averaging the corresponding potential profiles gives a solution average potential profile that is purely electrostatic. However, due to the TIR generation mechanism and the size of our particles, the intensity distribution goes to zero because the particles move out of the sensing range of the nanofiber, unlike in the planar TIRM case where the particles are remain between a range of positions dictated by the potential well of the system, which is well within the device sensitivity range of the traditional TIRM setup. This means that for nanoparticle far from the nanofiber, they will not scatter enough light during the exposure time of the CCD to generate enough charge on the sensor to increase the pixel value above the noise floor of the system. These nanoparticles are still in solution, it is just that we cannot distinguish their signal from the noise and therefore we cannot detect them with our current TIRM method. This can be represented as a cutoff probability distribution

shown as the dotted line in Figure 4.3–1. In the nanofiber TIRM case, this low-intensity cutoff is not so much a consequence of the system physics, but a result of the limitations of the sensing mechanism as well as the processing algorithm. These qualitative descriptions of the physical mechanism leading to the shape of the experimentally derived low-intensity/large-distance are summarized in Figure 4.3–1 where the experimentally obtained histograms are expected to have a qualitative form similar to the shaded regions.

This analysis of the expected shape of the intensity distribution assumes a perfect detection scheme. Although in reality, in addition to the sensitivity cutoff of the TIR mechanism and CCD data collection scheme, there is an overlaid noise signal that represents the error of the detection algorithm that incorrectly identifies the background noise as scattering signal. This is present because the threshold value in Equation (2) is not perfect and may underestimate the noise level for some frames, even with the cross-referenced detection scheme. Because we know background noise is typically Gaussian distributed, we expect this overlaid noise signal to be likewise Gaussian distributed and centered about the signal cutoff edge of the intensity and distance distributions (dotted line).

4.3.2. Noise-Based Filtering via Cluster Analysis

Assuming this form of the noise signal lends the filtering process to cluster-based methods for distinguishing the noisy data from good data. Cluster analysis of the intensity distributions typically requires plotting the data against two variables in a scatter plot. For this filtering method we use a scatter plot similar to the one in Figure

4.2 to perform the cluster analysis. The noise in both quantification methods should be Gaussian distributed although with different standard deviations. We use a Gaussian mixture model (GMM) to perform a soft clustering of the data into two clusters, noise and signal, where each data point is associated with a particular probability of being in either the noise cluster or the signal cluster. Data with a greater than 50% probability of being in the noise cluster are marked as noise and consequently removed from the dataset. GMM soft clustering of the dataset from Figure 4.2 and the subsequent histogram filtering based on this clustering is shown in Figure 4.3–2. The soft clustering scheme is employed because the Gaussian noise (signified by the red cluster in the scatter plot in Figure 4.3–2) is overlaid on top of good data and a hard cutoff clustering does not allow for potential preservation of some of the good noise buried in this noise of the dataset.
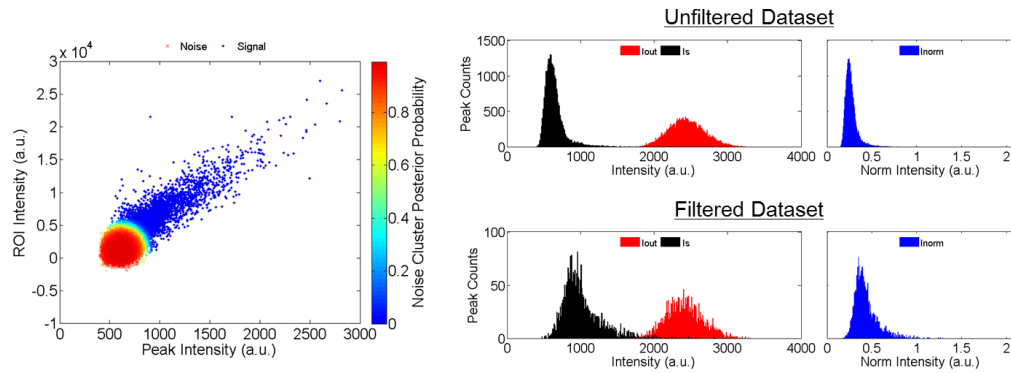
Figure 4.3–2. Clustering analysis and filtering. *Left*: Soft clustering using a 2-cluster Gaussian Mixture Model (GMM) with posterior probability of being in the noise cluster shown with color. *Right*: Unfiltered and filtered distributions detected event intensity (black), corresponding waveguide output intensity (red), and normalized intensity (blue).

While noise cluster filtering is a good way to ensure proper execution of the detection algorithm, it is remains difficult to know for sure how accurate the detection

scheme performed short of going through the data by hand and identifying each scattering event by eye. This is very impractical, therefore to get at least a qualitative idea of how well we detect the scattering events as a secondary verification, we plot the scattering profile of the length of the fiber along the y-axis of an image and the frame number along the x-axis. We break up the total number of frames into 2000 frame increments and vertically concatenate these subsets for easier viewing in a single image as shown below. We plot the detected scattering events on this image based on its centroid y-position and frame number (red circles) and qualitatively examine the images for sections of the video where we do not get consistent detection (possible threshold calculation errors, large background scattering, or setting of nanoparticle) or where we get horizontal streaks of circles (indicating detection of noise or persistent scattering data). Checking this plot, shown in Figure 4.3–3, after processing each dataset provides a general idea of how well the algorithm extracted the true distribution of scattering events from the raw video data. To look at these different sources of error further, we can plot the detected data as a function other processing parameters.
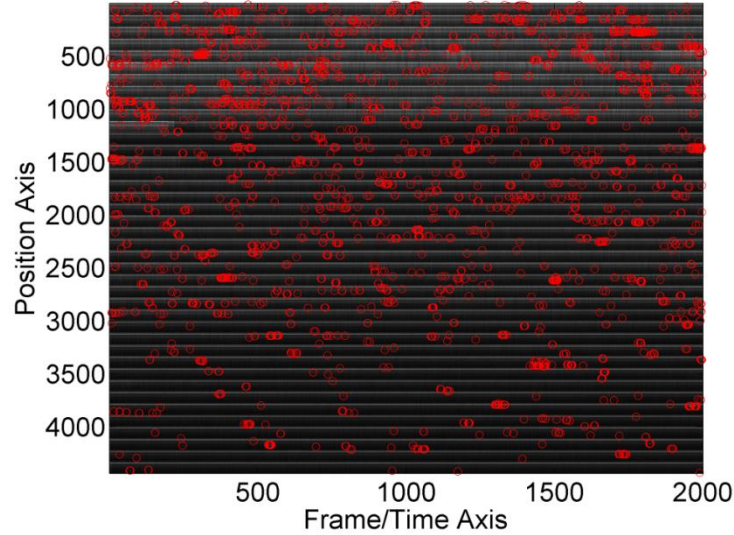
Figure 4.3–3. Data visualization of detected scattering events. Position-Frame image of scattering events and the detected signals (red circles) to visually inspect and qualitatively determine accuracy of detection algorithm. 1D intensity profiles along the fiber (approximately 300 pixels long) are horizontally concatenated for 2000 frames to form a 300x2000 sub-image. These sub-images are vertically concatenated for the entire dataset to form the image above.

4.3.3. Stability-Based Filtering via Temporal Signal Analysis

Once the quantitative scattering data has been extracted from the raw video and filtered as best as possible based on the known form of the noise, the next step towards inferring physical properties of the colloids in solution is to verify that the system setup was stable and that there are no physical peculiarities of the system that would skew the dataset. In this second filtering method, we filter the dataset based on physical sources of distribution skewing rather than data processing sources of error in the previous section. In particular, stability of the experimental setup and stability of the colloidal solution over time are the two aspects of the system under scrutiny.

Verification of the setup stability effectively means that the device setup under the microscopy has minimal drift. Stage drift affects the datasets because it changes the efficiency of the free space coupling of the laser light into the fiber cavity, which as we know will affect the intensity-distance relationship of Equation (1), effectively changing the scaling factor, I_0. Additionally, changes in the relative position of the focused laser beam on the device substrate can also change the background noise of the system. Background noise will affect both the quantified peak intensity and the integrated intensity. Because of these errors, we need to have ways of verifying the setup is consistent for all datasets. As we have discussed with the normalization of the scattering intensity, the waveguide output is a good measure of the coupling efficiency into the waveguide. Therefore we expect that the modulation of the waveguide output scattering in time will center around a mean intensity that is constant. Additionally, because we estimate the background noise in the detection algorithm by Equation (2), we can look at the threshold (and its components) over time to get a measure of the stability of the background noise. These plots are shown in Figure 4.3–4 below. If any of these plots show a trend over time other than fluctuation around a constant value then more critical examination of the dataset is needed to determine if it is a usable dataset.
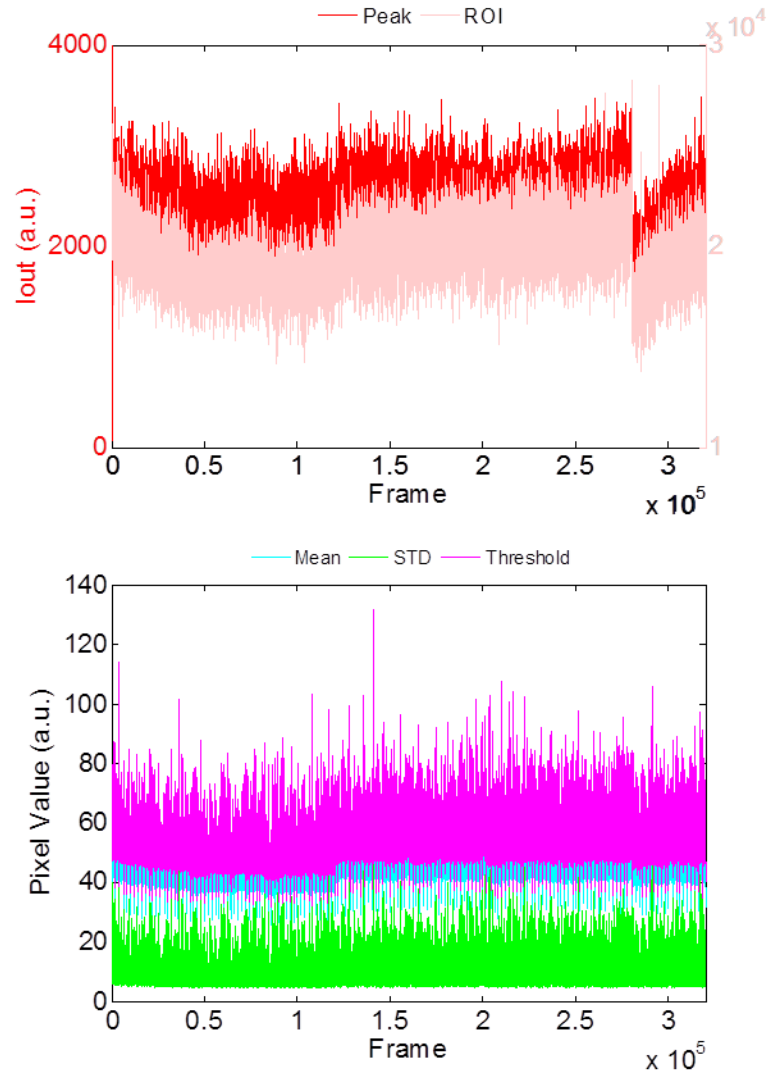
Figure 4.3–4. Verification of experimental setup stability. Plots of the waveguide output signal (using both peak and integrated intensity methods) and the calculated threshold value (and its components) for each frame of the dataset.

In Figure 4.3–4 the variation of the waveguide output in time for both the peak and integrated intensity method are shown in the top plot. For the most part, the intensity looks relatively stable for the middle portion of the collected data. The decaying trend in the initial part of the time series looks to be due to a settling of the

experimental setup where perhaps the focus of the laser on the waveguide end facet becomes misaligned as the stage, the focusing lens, or the coverslip moves over time, causing the a change in the coupling efficiency of guided light in the nanofiber optical cavity. This gradual system settling is markedly different from the abrupt change in the intensities around Frame 120,000 or Frame 280,000. These abrupt changes in the intensity result from realigning of the experimental setup between data collection, where now the change in coupling efficiency is not gradual. However, because the magnitude of these changes is not to large, the dataset us still usable as long as the quantified intensities are normalized to this output signal. Considering the corresponding threshold in the bottom plots, it is clear from the mean signal (light blue) that the realignment does affect Equation (2). However, we see that the change in the threshold, while negligible, follows the trend in the above plot, indicating that the detection algorithm is dynamic and able to adjusts according to the state of the experimental setup.

The next verification we must do is of the stability of the colloidal system itself. This setup is particular to the specific analysis we aim to perform on the steady-state nanoparticle-nanofiber surface interaction, but may also be a method of particle characterization itself if the data is examined more thoroughly. The static system analysis we aim to do relies on the assumption that the PDF of the system for any given PBS concentration does not vary over the course of the experiment.

The first thing we must filter out of the datasets is the persistent scattering of particles that have attached to the fiber. Identification of these attached particles is

done primarily by comparison of the collected video with the standard image taken of the assembled, cleaned device in the experimental setup with a control solution of DI water without any nanoparticle. This can be taken once, immediately after device fabrication, to identify any intrinsic scattering centers along the fiber that are due to physical or crystal defects along the fiber itself (for an ideal nanofiber, these intrinsic scattering spots should be minimized because no good data can be collected from that position of the waveguide and they effectively reduce the active sensing area of the nanofiber). Then during the experiment, if a new scattering center is identified, we can be confident it is an attached nanoparticle.

To filter out all data from persistently scattering locations along the waveguide (except for the waveguide output) we can plot the position of all the detected scattering events as a function of their position along the nanofiber axis, and any position along the fiber that has a much larger frequency of detected events can be excluded from the final dataset. Automatic filtering based on an expected frequency of hits in a given time interval can also be performed where the distribution of detected events in a 2000-frame interval is plotted. This can also provide dynamic information about localized contamination on the waveguide if a change in this distribution occurs over time. Additionally, localized accumulation of scattering events at particular points along the fiber could signify a physical difference of that particular location along the waveguide. The location distribution of the detected events is shown in Figure 4.3–5.
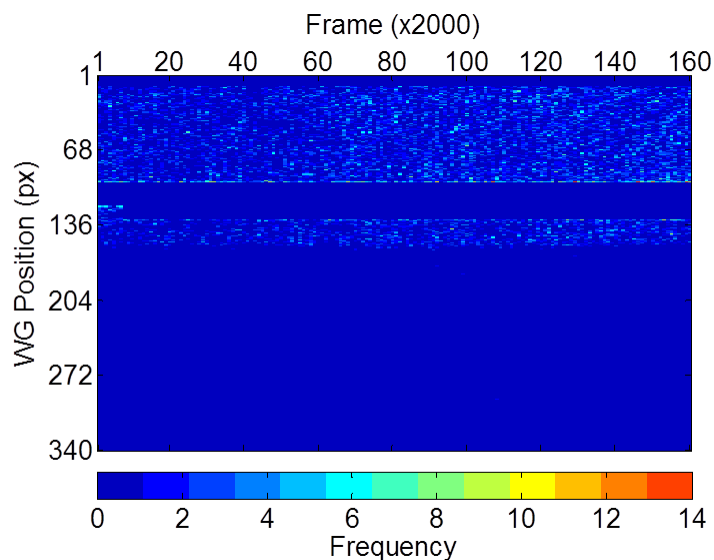
Figure 4.3–5. Distribution of detected event location in time. Distribution of the location of the detected scattering events over a 2000-frame interval is shown for consecutive, non-overlapping intervals. Persistent scattering events are removed as indicated by the clearly seen zero frequency band between pixel 68 and 136. The output signal location is also removed from the plot.

The presence of patches of high frequency would have indicated that significant skewing is present in the final intensity distributions. This skewing would also likely obscure the real data as the detected intensities would be above the noise floor of the data. If the excluded persistent scattering data in the above figure were included in the final histogram, it would be seen as a high intensity Gaussian distribution, with width related to the fluctuation of the coupling efficiency. In Figure 4.3–5, since there is no portion of the image that indicates that there is a concentration of high frequency signal, we can assume that the extracted data is correctly detected using the above algorithm.

The slow formation of NP dimers, trimers, or larger aggregates in the prepared nanoparticle solutions may also skew the data histograms over time (which is what we

were trying to avoid with DLS). The aggregation of particles also accelerates the flocculation of the colloidal system out of suspension, decreasing the rate of detection. To visualize any sort of change in the PDF over time, we can plot the scattering intensity histogram over an increment of 2000 frames as a single row profile (similar to the above datasets for detection location) and generate an image of those concatenated profiles in time. The, slow shifting of the histogram distribution over time may be easily visualized with this plot, which may indicate the presence of the dynamic physical phenomena described above. Aggregation would be seen as a slight shift of the scattering distributions towards higher intensities (see Chapter 6) as well as diminishing of the overall detection frequency over time. The detection frequency of the scattering events can be extracted also from this data by plotting the cumulative number of detected events over time. Aggregation would be also indicated be a corresponding plateauing of the cumulative detection plot as the number of individual scattering objects in solution would decrease. This plateauing could also just indicate overall settling of the colloidal out of suspension. These graphs of colloidal stability are plotted in Figure 4.3–6 where the distribution of intensities looks to be relatively stable over time and the cumulative detection is linear, indicating system stability. It is interesting to note that slight changes in the total detected events (frequency in the top image and slope of the bottom plot) correspond to the changes in the waveguide output signal of Figure 4.3–4. With all of these post-processing graphs, it is possible to identify the specific sources of error by cross-referencing the dynamic distribution plots (4.3–3 through 4.3–6) with each other and inferring the physical state of the

system stability and experimental setup as it is manifested in all the plots because they are all collected from the same dataset.
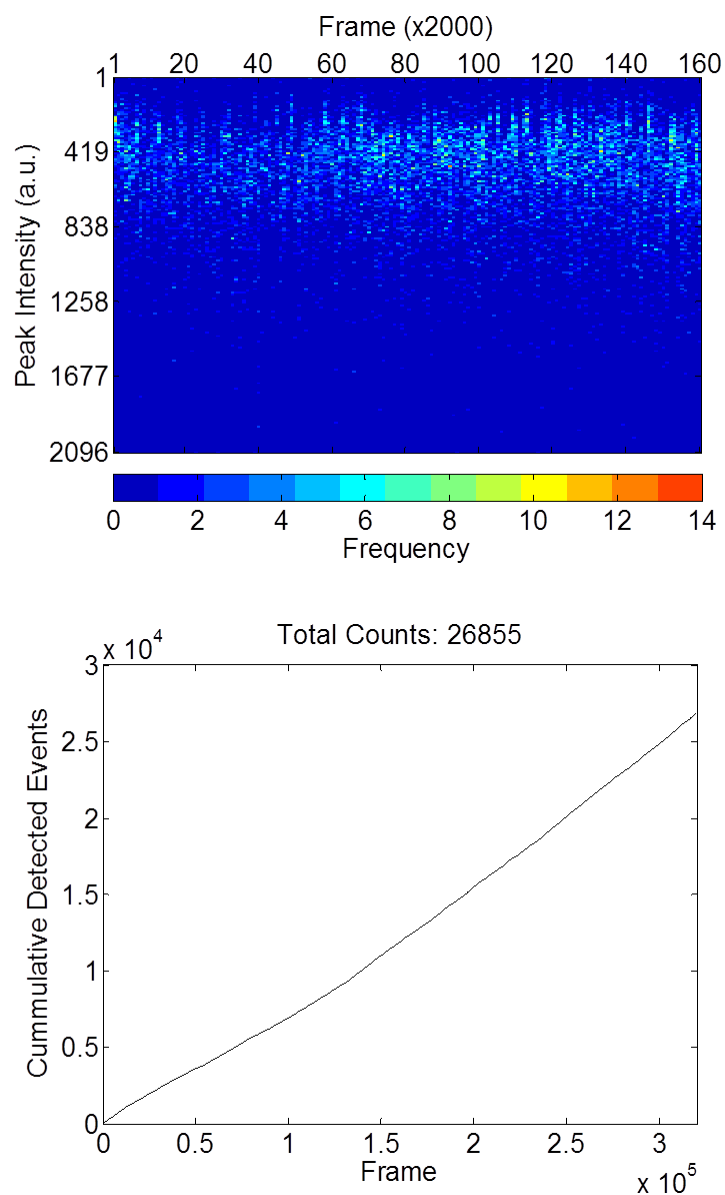
Figure 4.3–6. Quantified scattering intensity in time. *Top*: The scattering intensity distribution from consecutive 2000-frame increments of data. *Bottom*: The cumulated number of detected events as a function of experimental frame.

Chapter 4, in part, is currently being prepared for submission for publication of the material. (Villanueva, Joshua, Qian Huang, Gaurav Arya, Donald. J. Sirbuly) The dissertation author is the primary investigator and author of this material.

Chapter 5

Experimental Verification of Platform

Performance

5.1. Theoretical Model Formulation

Once the raw data has been processed and the accuracy of the detection and quantification algorithms have been verified, we are ready to examine the physics of the colloid-nanofiber interaction in further detail. After all, the utility of the nanofiber TIRM technique relies on relating the statistical distribution of experimentally-measured intensities to the physical properties of the colloidal sample. Here, we aim to leverage simple models that can be easily combined in a multi-physics description of overall device operation. While we recognize that much more sophisticated (and potentially more accurate) physical description of each component of the platform have been developed, their application here is beyond the scope of this dissertation, with the primary goal of establishing a comprehensive and generalized understanding of the operation of the nanofiber-based TIRM. Once the device physics has been established with simple analytical expressions, we can then test these models experimentally to verify that they are accurate enough to describe platform operation within specified limits.

Figure 3.1–1 highlights the different coupled physics associated with this platform. As was described qualitatively in Chapter 2, in an ionic solution the distance, d, between a Brownian particle and a stationary surface is dictated by the balance of the particle's thermal energy and the electrostatic potential between the surfaces. A static model of the electric double layer (EDL) that surrounds all charged surfaces links particle-nanofiber interactions with physical properties like particle size, surface charges, and ionic strength of the solution. Accounting for the EDL in the

equations governing the stochastic motion of the diffusing particles forms the multiscale physical description required to statistically characterize colloidal interactions using the distance-dependent TIRM mechanism. Modeling the random colloid movement near a wall with an EDL-mediated electrostatic interaction is done via an iterative simulation method to describe the Brownian dynamics (BD) of the system. The following sections describe each aspect of this model in further detail.

5.1.1. Electric Double Layer

We utilized the interacting electric double layer (EDL) model as formulated by Ståhlberg to describe the interaction of a charged nanoparticle with a nanofiber surface. [59] In this model the linearized Poisson-Boltzmann (P-B) equation was solved (with a constant surface charge boundary condition) for the potential distribution, $\Psi(d)$, between two charged infinite flat surfaces in an electrolyte solution as a function of separation distance as shown in the blue inset in Figure 2.1. The result was used to calculate the interaction potential between the two surfaces. Applying the Derjaguin approximation yielded an expression for the interaction potential between a sphere and an infinite flat wall

$$U_{EDL} = -\frac{\pi R}{\varepsilon_0 \varepsilon \kappa^2}[(\sigma_{NP} + \sigma_{WG})^2 \, ln(1 - e^{-\kappa d}) + (\sigma_{NP} - \sigma_{WG})^2 \, ln(1 + e^{-\kappa d})] \quad (7)$$

where R is the radius of the sphere, ε is the relative permittivity of the surrounding medium (in this work we used value for water), ε_0 is the permittivity of free space, κ is the inverse of the Debye length ($\kappa = \lambda_D^{-1}$), σ_{NP} and σ_{WG} are the surface charge densities of the sphere and flat wall respectively, and d is the surface-to-surface sphere-wall distance. Although only a rough geometric estimate for our nanoparticle-

nanofiber system, the following sections will test if Equation (7) sufficiently predicts the general qualitative trends in the nanoparticle distributions as a function of different colloidal parameter sweeps in proof-of-concept experiments. The equilibrium distribution of nanoparticles as a function of nanoparticle-nanofiber separation distance is described by Equation (5).

Here we make use of a number of approximations whose limits of applicability must be understood and rigorously checked for all systems to which this analysis is applied. First, the Debye-Huckel approximation (i.e. a first order Taylor expansion of the exponential term) is used to linearize the P-B equation, effectively giving it a form similar to the Helmholtz equation, which has a known analytical solution. This linearization is valid for systems with potentials less than 25mV, but has been shown to be somewhat accurate for potentials up to ~50-80mV. [60] Beyond that, the Debye-Huckel approximation largely overestimates the potential distribution. In order to solve the linearized P-B equation, we have to use either constant charge density boundary conditions or constant surface potential boundary conditions. In this case we used the former because the interaction of Brownian particles is assumed to be too fast to allow for chemical potential changes due to surface adsorption.

The second approximation used is the Derjaguin approximation, which enables us to calculate the interaction force between two charged objects in terms of the known interaction free energy between two charged flat surfaces. This approximation requires that the separation of the two charged surfaces be very small relative to the size of the particle, such that the ratio of the particle radius with the Debye length (κR)

is much larger than 1. For the PBS concentrations we consider in this work, the Debye length ranges from 10 nm − 2 nm (0.005xPBS − 0.1xPBS) and the particle radius is nominally 40nm, giving us a min κR of about 4.

5.1.2. Brownian Dynamics

While the long-time distribution of distances is described by Equation (5) and Equation (7), the movement of the nanoparticles around the nanofiber on a shorter timescale can be described using the Langevin equation shown in Eq. (8) [61]:

$$d = d_0 + \left[\frac{-\nabla U_{EDL}}{\gamma}\right]\Delta t + \zeta(t) \tag{8}$$

From Eq. (8) the new position d of a spherical particle after a time, Δt, (the simulation time step) can be calculated from its current positon, d_0, the instantaneous electrostatic force acting on the particle [calculated from the negative spatial gradient of Equation (7), $-\nabla U_{EDL}$] normalized by the drag coefficient of a sphere in a viscous medium, γ, (equal to $6\pi\mu R$ where μ is the viscosity of the surrounding solution and R is the nanoparticle radius), and a stochastic term, $\zeta(t)$, which is modeled as a random number drawn from a Gaussian distribution of mean zero and standard deviation equal to the mean squared displacement (MSD) of a particle (MSD = $\sqrt{2D\Delta t}$ where D is the diffusivity of the spherical nanoparticle, $D = \frac{k_B T}{\gamma}$). Using Equation (8), we can iteratively calculate these positions to obtain one-dimensional stochastic trajectories of several (non-interacting) particles randomly moving in the one-dimensional electrostatic potential field described by Eq. (7). Verification of the BD simulation

was done by comparing the accumulated distribution of distances with Equation (5) to make sure they match up according to the underlying system properties.

To verify our physical interpretation of the system and test the accuracy of the model formulation for predicting the behavior of these systems, we present a side-by-side comparison of experimentally-measured and theoretically-predicted intensity distributions in the following sections. For verification, proof-of-concept studies were performed with single-variable parameter sweeps, characterizing gold nanoparticle systems of various sizes (smaller than 200 nm), with two different surface coatings, and in solutions of different ionic strength. Equations (5) and (7) describe the long-time behavior of the system based on the physical properties of the particles in solution, and along with our intuition for the expected datasets, we should be able to judge the accuracy of the model's predictions with the experimental results.

5.2. Varying Solution Ionic Strength

Intensity distribution trends were studied under different ionic solutions to test the accuracy of Eq. (7) for approximating the EDL interaction of our nanoparticle-nanofiber geometry. Using the general experimental procedure described in Chapter 3, a nominal system of 80 nm citrate-coated gold nanoparticles was prepared in different concentrations of PBS, and each prepared solution was tested in a separate experimental run. The solutions were all prepared from a single batch of washed commercially purchased nanoparticles and diluted in different solutions of PBS concentration just prior to full device assembly and data collection. Between each experiment, the full device assembly was taken apart and cleaned according to the

procedure outlined in Chapter 3 and data for all the different ionic solutions was collected in the same day where experimental data was collected using a the nominal camera parameters described previously and a 10 ms exposure time. The effect of varying the ionic concentration [κ in Equation (7)] is shown in Fig. 5.2–1 as different colored histograms overlaid on a single plot. The raw collected videos were processed according to the algorithms described in Chapter 4.
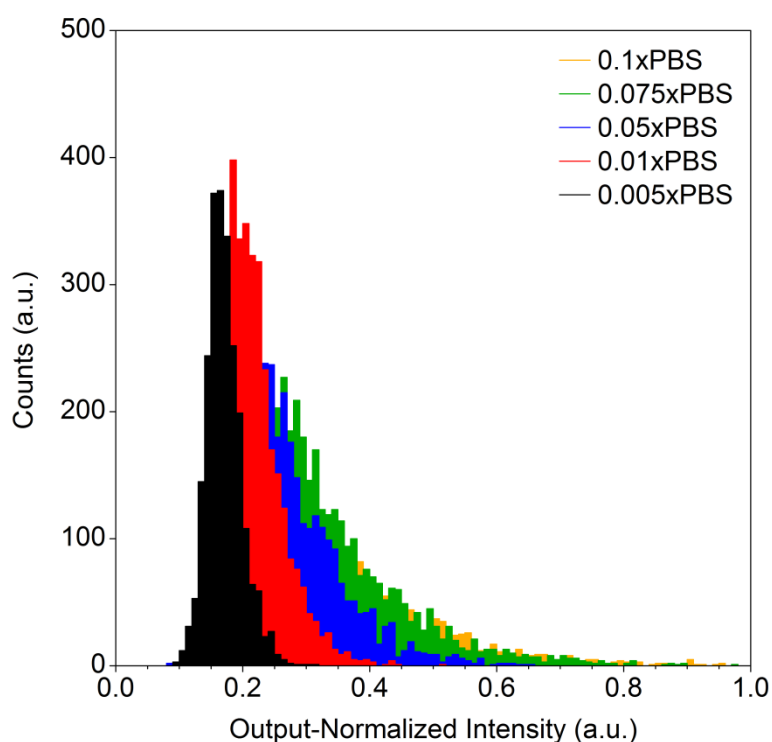
Figure 5.2–1. Experimental intensity distribution varying solution ionic strength. Detected and quantified peak scattering intensity data is normalized to the intensity of the waveguide output in the same frame. Histograms of the post-processing filtered intensity data for experimental runs with 80 nm citrate-coated particles in different concentrations of PBS are shown with a 0.01 bin width. Scattering data was collected with an exposure time of 10 ms using the same waveguide, cleaned between each experimental run. All experiments were run using the same prepared solution of washed colloidal particles in the same day.

Qualitatively, the shape of the distributions fits with our description of what we expect the processed data to look like from Chapter 4, Section 3. The high intensity edge of the datasets decrease to zero according to the balance between the thermal energy of the system (the same for all distributions) and the electrostatic potential between the surfaces (changing depending on the ionic strength of the solution). As the salt concentration increases, the electrostatic potential between the nanoparticle and nanofiber surface is expected to be screened more, and therefore the particles can get closer, on average, to the fiber. According to Equation (1), the closer particles will result in higher intensities. At the low intensity edge of the distributions, the data also decreases to zero according to the sensitivity cutoff of the data. The data was filtered to remove a large portion of the Gaussian distributed noise that obscures the sensitivity cutoff and the intensities were normalized to the waveguide output. The fact that the high salt normalized scattering intensities is an interesting result suggesting that the quantified intensities for these high salt experimental runs was larger than the quantified waveguide output. The physical implications of this will be discussed in Chapter 6.

Plots of theoretical electrostatic potential between the two surfaces and the predicted PDFs based on this potential are shown in Figure 5.2–2 for comparison with the experimental results. In order to calculate these curves, we must use nominal parameter values for all the variables in Equation (5) and Equation (7) that we assume are close to the real values that determine the experimental results shown in Figure 5.2–1. For Equation (7) we use the values for the nominal 40 nm radius of the particle

and the relative permittivity of water. κ is calculated from the equation of the Debye length for a monovalent electrolyte solution with ionic strength calculated for the different PBS concentrations. [57] A value for the surface charge density for the waveguide is taken from literature (0.05 Cm^{-2}), [62] and the surface charge density for the citrate-coated nanoparticle is calculated using the Grahame equation where the experimentally measure zeta potential of the prepared colloidal solutions (using a Zetasizer) is used as an approximation of the surface potential of the nanoparticle (0.012 Cm^{-2}). [24] The temperature of the system was assumed to be room temperature, 298 K, for Equation (5). Since the long-time distribution of particle distances calculated using the Langevin equation should also result in Equation (5), we can also run the BD simulation to generate the expected distributions and compare them to the directly calculated trends in Figure 5.2–2. These simulated distance distributions are not explicitly shown here, but the resulting distributions of the BD simulations match with the theoretically predicted distance distributions.
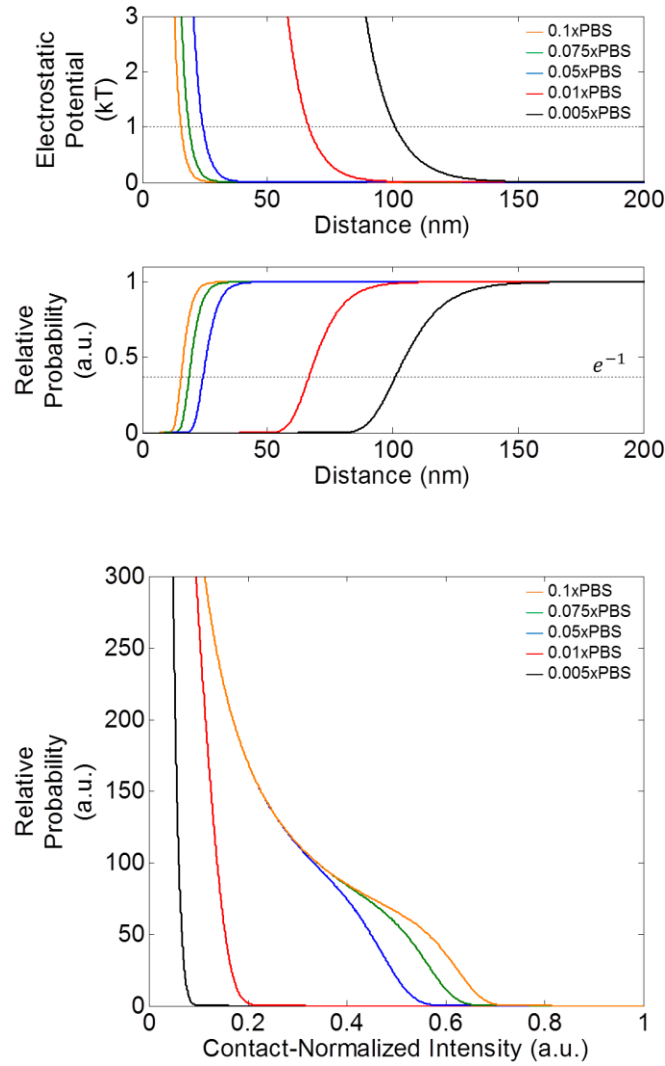
Figure 5.2–2. Theoretically predicted distance and intensity distributions as a function of ionic strength. Electrostatic potentials calculated for an 80 nm citrate-coated particle near a SnO_2 waveguide in units of kT. The corresponding relative (non-normalized) PDFs of the nanoparticle distance to the nanofiber surface are plotted below with the e^{-1} probability shown. The bottom plot shows the relative PDFs of intensity calculated from the distance PDFs and the nominal intensity-distance relationship of Equation (1) with $\tau = 34$ nm and the scattering normalized to the intensity of a particle at contact, I_0.

Since the experimental histograms are of quantified intensity values, we can

use Equation (6b) to calculate the expected intensity distributions. For this, we need to

have values for the scattering at contact, I_0, and the surface-normal intensity-distance decay constant, τ. For the purposes of comparison in this chapter, instead of using an estimated value for I_0 we simply normalize the scattering intensities relative to this number in Equation (1), which eliminates the need to define it [i.e. $I_0 = 1$ in Equation (6a)]. This is similar to normalizing the data to the waveguide output intensity as described in Chapter 4 because I_0 will also fluctuate as a function of the evanescent power. However, here we know that I_0 corresponds the scattering of a particle that is in contact with the nanofiber surface whereas the waveguide output intensity does not correspond to any physical nanoparticle distance. This is an important distinction to be made for interpreting physical meaning from the normalized intensities. For purposes of comparing the relative shape of the intensity distributions in this section, this contact normalization will be sufficient. For the decay constant, we use the experimentally measured decay constant of 34 nm from [63], which was obtained by mapping out the distance-dependent scattering profile around a SnO_2 nanofiber with an 80 nm gold nanoparticle attached to the tip of an AFM. In a similar manner as the treatment of the distance distributions, the BD simulations can also be used to map out the steady state distribution of Equation (6b) by calculating the individual intensities associated with each nanoparticle position [using Equation (1) and the contact normalization and decay constant described here] during the simulation and accumulating the intensities to form the distributions. The intensity distributions are shown in Figure 5.2–3 below where the intensity value was normalized in the same way as the theoretical distributions using the accumulated scattering intensity from a

stationary particle at contact with the fiber. Comparing Figure 5.2–2 and Figure 5.2–3 shows qualitative similarities between the intensity distribution trends, but the contact-normalized intensities are notably smaller for the simulated data compared to the theoretical distributions. This is attributed to the fact that the simulated intensities are generate from an accumulation of calculated intensity values in a finite exposure time, whereas the theoretical distributions are calculated under the assumption of zero exposure time. This idea will be discussed further in Chapter 6.

The range of PBS concentrations examined here represent the limits of the operation for this particular nanofiber and nanoparticle system. For ionic concentration lower than 0.005xPBS, the nanoparticles cannot get close enough to the fiber to generate enough scattered light to be distinguishable from the background noise in the detection algorithm. At higher PBS concentrations, these electrostatic repulsion between the citrate-coated gold nanoparticles and the bare SnO_2 nanofiber surface is screened enough that the particles that get close will then fall into a deep energy minimum (perhaps due to the van der Waals interaction and small optical gradient force of the TIR setup) that prevents from leaving the surface of the fiber. Since this configuration of the nanofiber-TIRM platform is concerned only with the interaction of freely diffusing particles near the nanofiber surface, these the persistent scattering from these attached particles will be ignored by the processing algorithm as described earlier. These limits imply that in this particular characterization mode of the platform, the limitations of the characterization for different particles will require experimental optimization of the ionic concentration of the system, which then must be considered

within the context of the application of the particles. In particular, for any sort of colloidal nanomedicine application, characterization of the particles using the nanofiber-TIRM platform will need to consider how the optimized ionic concentration of the experiment will translate to behavior of the particles *in vivo* where the ionic strength of the local environment (e.g. circulatory system) may be closer to 1xPBS.
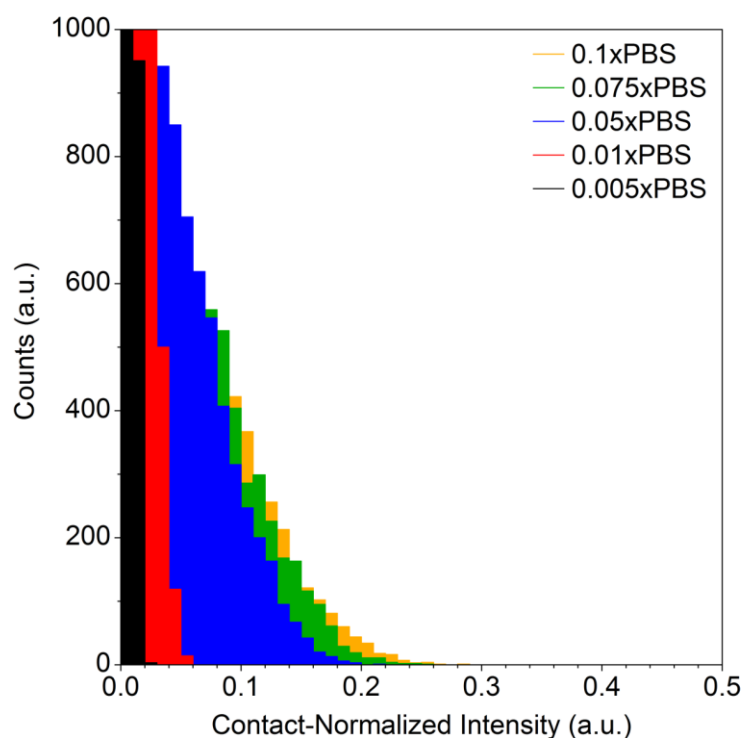
Figure 5.2–3. Simulated intensity distributions as a function of varying ionic strength. Scattering intensities calculated using the Brownian dynamics to simulate particle trajectories near a wall under the influence of EDL interactions for an 80 nm citrate-coated nanoparticle near SnO_2. Intensities are calculated using Equation (1) with $\tau = 34$ nm and I_0 arbitrarily set to 1. These instantaneous intensities are calculated for all positions simulated in a trajectory (using a time step, Δt, of 10^{-8} s) and accumulated for a 10 ms exposure time. This final accumulated intensity is normalized to the theoretical intensity of a similar particle that was stationary at contact for all time steps of the simulated trajectory. This was done for 100 particles for a total simulation time of about 50 s to obtain 500,000 scattering events for each simulated distribution.

5.3. Varying Nanoparticle Surface Charge Density

We also verified the theoretical models against differences in the surface charge density of the nanoparticles. For this study we compared the nominal 80 nm citrate-coated nanoparticles prepared in the previous experiment with 80 nm DNA-coated particles that were prepared in a similar manner. The DNA nanoparticles were synthesized with properties described in [56], and this data was collected on a different day as the previous set of data with varying ionic strength. The experimental 0.05xPBS distribution from Fig. 5.2–1 is replotted in Fig. 5.3–1 with the distribution obtained with the DNA-coated particles under the same experimental conditions (also collected with a 10 ms exposure time) for comparison. Qualitatively, the intensity distributions again have a similar form as expected from the cutoff of the device sensitivity and the noise filtering at the low-intensity edge of the distribution. It is expected that the DNA-coated surface is more negatively charged than the citrate-coated surface, therefore a shift in the intensity distribution to lower intensities (corresponding to a slight increased electrostatic repulsion) makes sense for the high-intensity distribution edge.
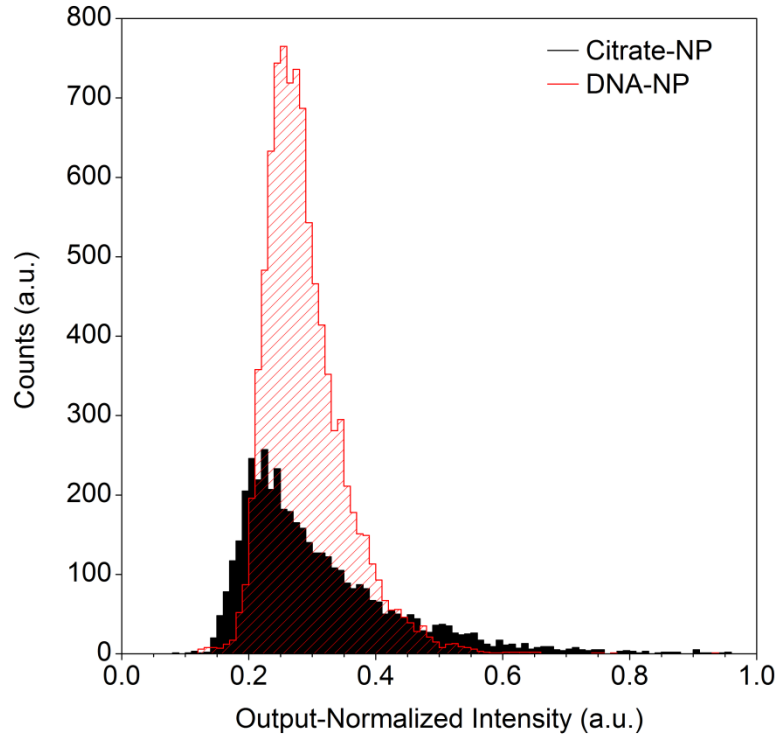
Figure 5.3–1. Experimental intensity distribution varying surface charge density. Detected and quantified peak scattering intensity data is normalized to the intensity of the waveguide output in the same frame. Histograms of the post-processing filtered intensity data for experimental runs with 80 nm particles of different coatings in 0.1xPBS are shown with a 0.01 bin width. The citrate data is replotted from Figure 5.2–1. Scattering data was collected with an exposure time of 10 ms using the same waveguide, cleaned between each experimental run. Both experiments were run on different days with prepared colloidal solutions from different stocks with different nanoparticle concentrations.

The simulation-predicted distributions for distance and intensity are shown in Figure 5.3–2 and Figure 5.3–3, respectively, calculated in a similar manner as described in the previous section. Here, the only difference is that we calculate the distributions for DNA-coated nanoparticle, which should have a different surface charge density. We estimate the surface charge density of the DNA-coated particles, σ_{DNA}, to be 0.019 Cm^{-2} from back-of-envelope calculations based on the approximate

number of quantified DNA strands per particle and the surface area of a spherical particle with radius of 40 nm. The amount of DNA per particle was quantified using the same method as [64] results in about 3440 strands per nanoparticle. We assume a charge of 1 electron per DNA strand corresponding to the charge of the 3' end of the grafted strand.

Comparing the intensity distributions in Figure 5.3–2 and Figure 5.3–3 we again see the smaller simulated intensities as a result of the accumulation method of calculating the normalized intensities. Also, it is evident by how similar theoretical the distributions are that the in order to see accurate differences in the experimentally derived distributions, large datasets with very precisely filtered distributions are required. This highlights the importance of the work done in Chapters 3 and 4 for the determination of a very detailed procedure. The careful examination of the data will ultimately influence the experimental sensitivity of the technique.

Comparison of the simulated data and the experimental data in Figure 5.3–1 shows a larger difference between the high distribution edges of the distribution, which would indicate that there are some errors in the estimated values for the experimental surface charge densities. Also, the primary difference between experimental data and simulation is the large population of low-intensity scattering seen in the DNA-coated data. This is possibly attributable to differences in the experimental setup and data processing of the data as these two datasets were collected on different days using two different stock solutions of washed particles with different concentrations. A difference in the experimental setup on different days may result in

different coupling efficiencies that, while accounted for with normalization, may result in different detection limits due to different calculated threshold values. The large Gaussian-shaped population in the DNA-coated particle data may be due to poor filtering of the data using the processing algorithm as well.

These possibilities must be investigated further to really identify the source of the difference between the datasets. However, considering that the simulated data compares distributions of particles under the exact same conditions save for the surface charge density (perfect detection accuracy, same nanoparticle concentration, same coupling efficiency, etc.), it is also possible that another physical phenomena could be at play. Because different surface functionality is a major design parameter for the field of nanomedicine, particularly with respect to specific targeting *in vivo*, this analysis shows how collecting experimental data and performing simulations in tandem (while also having a detailed understanding of the signal transformation pathway) can help identify errors in the modeling or data processing. These are critical observations for any physical interpretation of data using this platform for the study of colloidal particles.
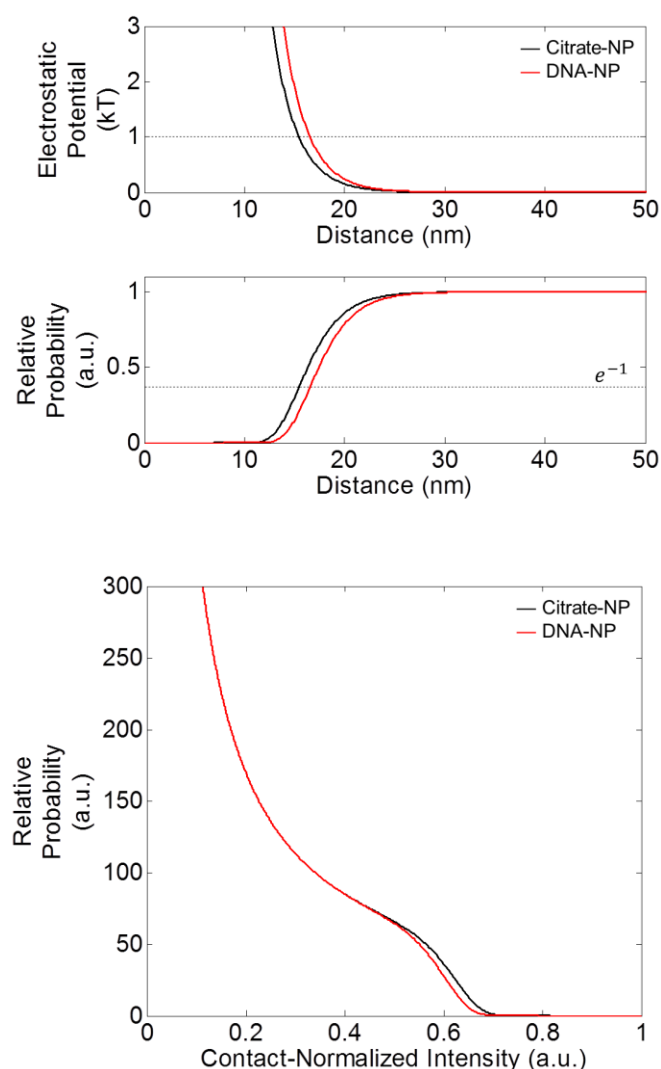
Figure 5.3–2. Theoretically predicted distance and intensity distributions as a function of surface charge density. Electrostatic potentials calculated for an 80 nm citrate-coated and DNA-coated particles near a SnO_2 waveguide in units of kT. The corresponding relative (non-normalized) PDFs of the nanoparticle distance to the nanofiber surface are plotted below with the e^{-1} probability shown. The bottom plot shows the relative PDFs of intensity calculated from the distance PDFs and the nominal intensity-distance relationship of Equation (1) with τ = 34 nm and the scattering normalized to the intensity of a particle at contact, I_0.
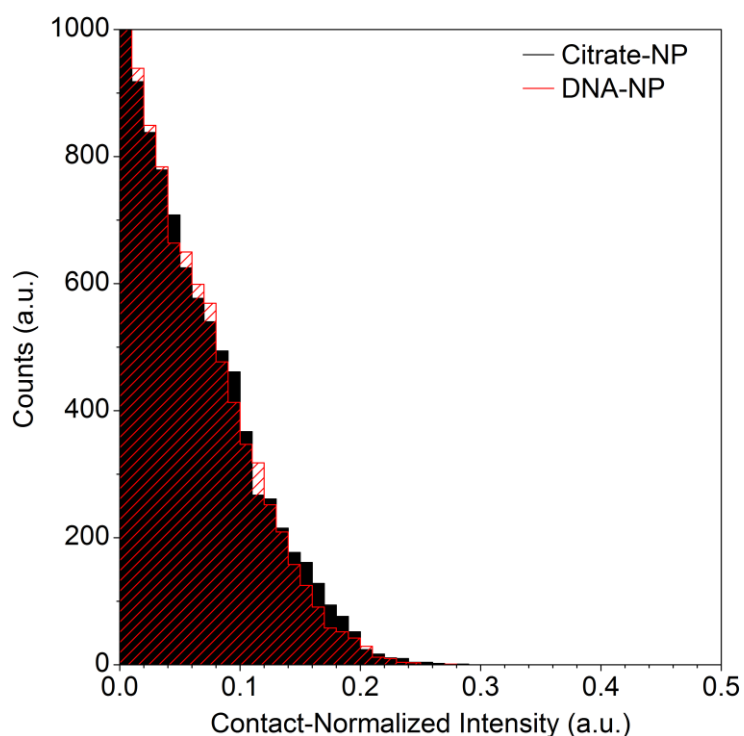
Figure 5.3–3. Simulated intensity distributions as a function of surface charge density. Scattering intensities calculated using Brownian dynamics to simulate particle trajectories near a wall under the influence of EDL interactions for 80 nm citrate-coated and DNA-coated nanoparticles near SnO_2. Intensities are calculated similarly to Figure 5.2–3 for a 10 ms exposure time.

5.4. Varying Nanoparticle Size

Finally, the intensity distributions were collected and compared for separate experimental runs with particle of different size. These experiments were conducted using 80 nm, 100 nm, and 150 nm citrate-coated nanoparticles in 0.1xPBS, collected with a 5 ms exposure time. Considering the effect of particle radius in the EDL model, we expected that for any given distance, the electrostatic interaction between the particle and fiber would increase for larger particles as the potential in Equation (7) is proportional to R. The experimental distributions are shown in Figure 5.4–1. The

experimental trends, however, do not look to be accurately described by a simple shift of the high intensity edge of the intensity distributions as would be expected from the theoretically predicted distance distributions shown in Figure 5.4–2. Here we assumed the same surface charge density of 0.024 Cm^{-2} used for the theoretical calculations of all other citrate-coated nanoparticles in this chapter. For the particle sizes experimentally examined, we see that the difference in the theoretical electrostatic potentials and thereby the PDFs is almost negligible, which does not correspond to the experimental distributions. The experimental distributions show the 150 nm particles have high-intensity distribution edges that are larger than that of the 100 nm particles, which are in turn larger than the 80 nm particles. This would imply that the 150 nm particles are closer to the fiber from our understanding of the data from Chapter 4, which is in direct opposition to the theoretical distributions of Figure 5.4–2. What has not been considered yet in the analysis of the chapter is how the scattering from the particles changes depending on the particle. This has not been an issue thus far since all particles experimentally examined up to this point have been the same size, but it is clearly a factor of the signal transformation pathway that must be considered.

To explain this discrepancy, we must now also consider the effect the particle size has on the scattering intensity separately from the simple electrostatics of the system. First we can consider that the Brownian motion of the particles would be different based on the Langevin equation in Equation (8). As the size of a colloidal sphere increases, the diffusion coefficient decreases. This means that the residence time of the nanoparticle near the fiber would effectively increase. Additionally, the

scattering cross section would be different for different sized particles based on the equation for Rayleigh scattering, which prevents us from directly generating the scattering intensity distributions here. We need to know more about how I_0 varies as a function of particle size. In order to explore this effect more, we needed to examine the dynamics of the signal generation process via far field imaging using a CCD in more detail. This is discussed in the Chapter 6.
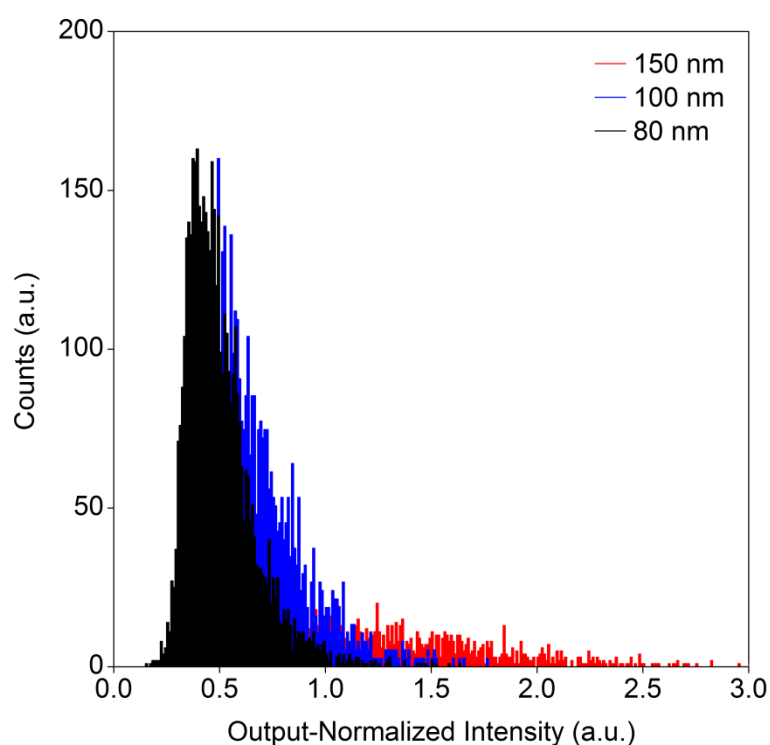
Figure 5.4–1. Experimental intensity distribution varying particle size. Detected and quantified peak scattering intensity data is normalized to the intensity of the waveguide output in the same frame. Histograms of the post-processing filtered intensity data for experimental runs with citrate-coated particles of different sizes in 0.1xPBS are shown with a 0.01 bin width. Scattering data was collected with an exposure time of 5 ms using the same waveguide, cleaned between each experimental run. All experiments were run on the same day with prepared colloidal solutions from different stocks with different nanoparticle concentrations.
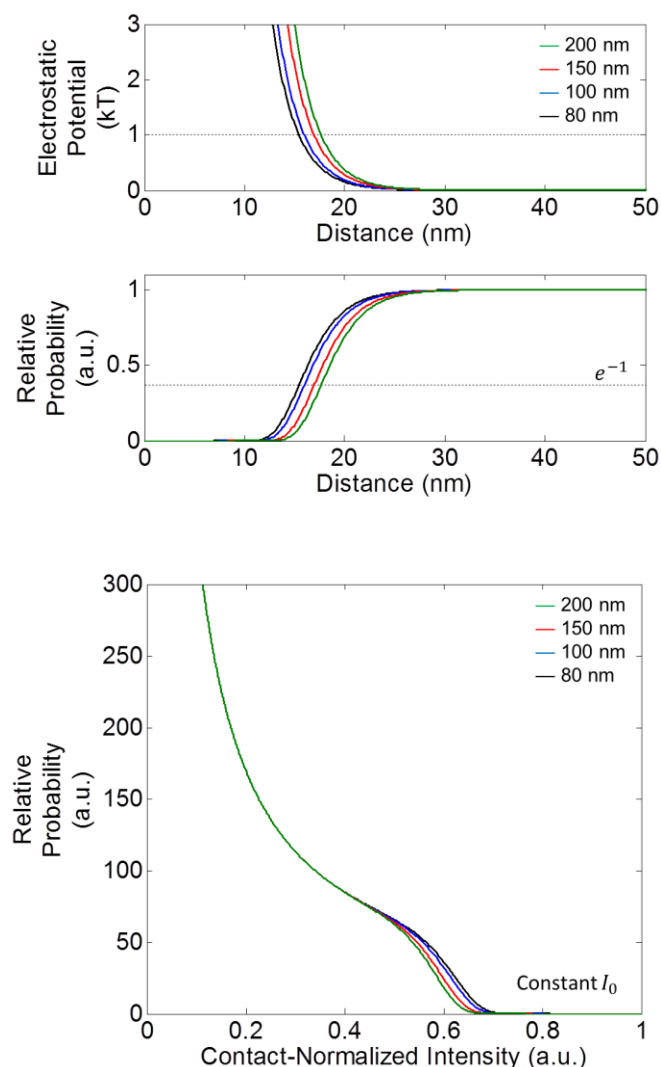
Figure 5.4–2. Theoretically predicted distance and intensity distributions as a function of particle size with constant contact scattering. Electrostatic potentials calculated for different sized citrate-coated particles near a SnO_2 waveguide in units of kT. The corresponding relative (non-normalized) PDFs of the nanoparticle distance to the nanofiber surface are plotted below with the e^{-1} probability shown. The bottom plot shows the relative PDFs of intensity calculated from the distance PDFs and the nominal intensity-distance relationship of Equation (1) with $\tau = 34$ nm and the scattering normalized to the intensity of a particle at contact, I_0, which was held constant for all simulations.

Chapter 5, in part, is currently being prepared for submission for publication of the material. (Villanueva, Joshua, Qian Huang, Gaurav Arya, Donald. J. Sirbuly) The dissertation author is the primary investigator and author of this material.

Chapter 6

Model for Far-Field Imaging

6.1. Generalization of the Intensity-Distance Relationship for TIRM

The last component of verifying the device physics considers how the data is collected. This last step in the signal transformation pathway relates the experimentally acquired intensity data with the particle positions described by the BD-EDL formulation. In planar TIRM, the conversion of scattering intensity to nanoparticle-nanofiber distance is straightforward using a calibrated intensity-distance relationship as described by Equation (1). [34] While the determination of I_0 and τ is a non-trivial matter, [63,65] once they are obtained the intensity is readily convertible to distance using a one-to-one correspondence. For our nanofiber system, however, we must examine in more detail how the scattering signal is generated to determine if Equation (1) is accurate for our purposes and can be used to explain the results of the particle size experiments in the previous chapter. This relies on understanding the general working principle of a CCD sensor.

To generate the raw collected signals in the experiments, the photons scattered by a particle in the evanescent field are collected by a CCD sensor in the far field. This results in a spatial distribution of charge on the sensor as photons hit specific pixels, which is then read out as a 2D array of numbers (pixel counts) on the computer to form an image. The photons from scattering events are allowed to accumulate on the sensor for finite exposure times, corresponding to how long the aperture of the camera is open. The time that the aperture is open directly relates to how many photons hit the sensor before the image is formed, resulting in different quantified intensities. This

time must be adjusted to collect enough photons to generate an image where the signal can be distinguished from the intrinsic noise of the CCD's sensor, but not so long that too many photons from other sources of light obscure the signal coming from the scattering nanoparticle. Then this process is quickly repeated to collect successive images in time, forming a video of the scattering event.

In this finite exposure time, the Brownian nanoparticles are constantly moving and will typically diffuse several hundred nanometers. From the distance-dependent scattering intensity of Equation (1), we know that while the particle's position varies relative to the nanofiber surface, the amount of light it will scatter will also vary. This means that there will be a varying rate of photons hitting the sensor during a given exposure time to generate an image of a scattering event. It is difficult now to use Equation (1) because we do not know to what actual distance a given intensity corresponds. In fact, a single intensity signal corresponds to an unknown stochastic trajectory rather than a single position, and there are a number of different trajectories that can produce the same scattering intensity. This idea is exemplified in Figure 6.1.
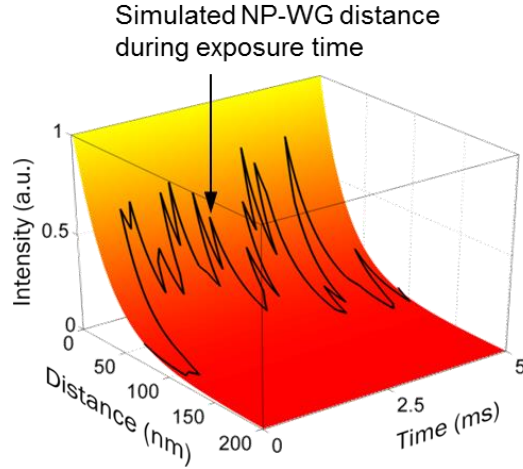
Figure 6.1. Varying instantaneous scattering of a diffusing Brownian nanoparticle during a 5 ms exposure time. A single quantified scattering event imaged by a CCD in the far field is obtained by integrating the intensities plotted by the black line over the exposure time, here 5 ms. The intensities change as the particle randomly diffuses near the nanofiber surface according to Equation (1) and shown here as the exponentially decaying surface. This intensity represents the nanoparticle's trajectory, rather than a single position.

Because we realize now that the scattering intensity depends on the movement of a Brownian particle, proper treatment of our intensity data requires a new model for collecting dynamic scattering data during the course of an extended exposure time, t_{exp}. In this way we can relate the scattering intensity to the size of the particle, which influences how the particle moves. In this new model, the total scattering intensity associated with a nanoparticle trajectory is then represented by the integral of all the instantaneous scattering intensities along this simulated particle trajectory. Equation (9) expresses this accumulation of intensities mathematically as an integral of intensity during a certain exposure time as the instantaneous scattering rate changes along the trajectory of the nanoparticle:

$$I_s = \int_{t_{exp}} A \exp\left[\frac{-d(t)}{\tau}\right] dt \tag{9}$$

where I_S is now the total scattering intensity of a particle (defined as number of counts in the peak intensity pixel) integrated over the exposure time, t_{exp}, with the term in the integral representing the instantaneous scattering of the particle at a particular time, t. The coefficient, A, is the instantaneous scattering rate at contact in units of counts per second, $d(t)$ is the trajectory of the nanoparticle in time, and τ is the same decay constant as in Equation (1) for the same waveguide. Because we calculate defined spatial trajectories of individual particles in the BD simulation, we can also calculate the instantaneous scattering of the particles at the different positions sampled using Eq. (1). Equation (9) is then incorporated in the BD simulations by approximating this integral as a Riemann sum using the trapezoidal rule. While we are specifically concerned with Brownian trajectories in our particular experimental setup, it is interesting to note that Equation (9) is a general expression that can be applied to any form of $d(t)$. With this generality in mind, we can examine limiting cases and different forms of particle trajectories to validate this model before we revisit the experimental trends with particle size. In fact we can classify different types of TIRM experiments now by the general quality of the particle trajectory in any particular experimental setup. In the following sections we consider three different types of particle trajectories: stationary, linear, and stochastic.

6.2. Model Verification: Stationary Particle

The simplest case of this generalized model is where the particle is held stationary. In this situation, the particle trajectory is a constant value independent of

time, d, and can be taken out of the integral. Evaluating the integral results in the static form of the equation:

$$I_{stationary} = At_{exp} \exp\left[\frac{-d}{\tau}\right] + B, \qquad (10a)$$

which is similar to Equation (1). However, here it is clear that the coefficient of the decaying exponential is a function of the exposure time, $I_0 = At_{exp}$. Additionally, we include a constant term, B, to represent the background signal of the data. This form of the scattering intensity-distance relationship was the basis for the experimental mapping of the evanescent field in [55] (without the background term). In this calibration method, knowing the approximate distance of the nanoparticle while the scattering intensity is being collected at a particular exposure time enables us to back out the decay constant.

To ensure that this equation makes sense with our understanding of the device physics, we examine the limiting cases of the station particle position. In the limit that the particle is really far from the nanofiber and d equals infinity, then the first term in Equation (10a) goes to zero and the collected scattering is simply equal to B, the intrinsic noise of the sensor plus the signal from background light sources collected by the CCD. This makes sense as there is no particle in the evanescent field. Conversely, when the particle gets close to the nanofiber d goes to zero, the exponential approaches 1, and we get a linear relationship between the scattering intensity and the exposure time of the system, with the slope equal to the instantaneous scattering rate of the system.

$$I_{contact} = At_{exp} + B \qquad (10b)$$

Since Equation (10b) represents the scattering of a stationary particle at contact, we can use this relationship to back out the parameters *A* and *B* by imaging a particle at contact at many different exposure times, getting the slope and y-intercept of the linear trend, respectively.

Figure 6.2 shows several linear trends for different nanoparticles attached to a fiber in pink, where an experimental run similar to that described in Chapter 5, Section 2 was prepared in a 0.1xPBS solution and a few particles were allowed to attach to the nanofiber before data was collected. Once the particles attached, the exposure time of the camera was varied and the data collected for 5000 image frames. The intensities plotted in Figure 6.2 were quantified using the peak intensity method (no filtering needed) and averaged over the 5000 collected frames for each attached particle. While the linear trends strongly validates Equation (10b), we see that the parameters fits from Figure 6.2 vary for different particles. This means that many particles must be analyzed in this manner to get an acceptable average value for *A* and *B* that can be generally applicable to all scattering events collected. The average over all nanoparticles is shown as the red line with the scattering from the nanofiber output is shown in black.
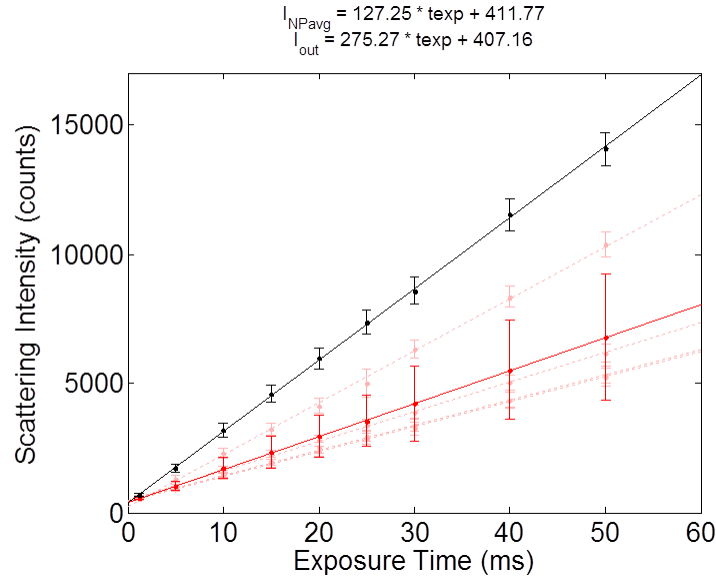
Figure 6.2. Exposure time analysis of multiple 80 nm particles in contact with the nanofiber. The pink data fit to different lines represents different attached particles, while the red data shows the average trend over all particles. The black data is the scattering from the waveguide output, and the error bars for the black and pink line show ± the standard deviation in the scattering intensities over 5000 collected video frames at each exposure time. The red error bars are ± the standard deviations of the particle average intensities at each exposure time.

This is a difficult experiment to perform because there are many sources of error that contribute to the final quantified intensity and we need to ensure that only variation in the particle size and shape are contributing to the different fitted parameters. To get a distribution of fits from multiple attached particle though is a tedious process because the number of particles that can be attached an analyzed for any one given experiment must be limited to only a few (less than 5) particles at a time. This is because we see that as more particles attach to the nanofiber, the output intensity diminishes, implying that multi-particle attachment will not produce the same fits as for a single attached particle. Therefore, allowing only a few particles to attach to the fiber at any one time ensures the quantified intensities are not affected by

upstream scattering of the particles as they may affect the guided power in the fiber. However, in addition to physical particle parameters, slight variation of the fitted parameters is inevitable due to variations in the setup when multiple particle data is collected, which cannot be perfectly repeated between different runs. The good thing though is that once the particle is stuck to the fiber, data collection is done by simply changing the settings on the camera via the computer and the experimental setup can be left undisturbed. This minimizes experimental setup variation in a single experimental run varying t_{exp}, resulting in a highly linear trend with exposure time for any given attached particle as long as its orientation and position do not change during the exposure time analysis or other particles do not attach the fiber during the data collection. Getting a good average for A and B should enable us to predict how the scattering intensity of a stationary, roughly spherical, 80 nm particle should change as a function of scattering intensity and distance from the nanofiber surface (assuming the same 34 nm scattering intensity decay for τ.

6.3. Model Verification: Linear Particle Trajectory

The true test of this model formulation is extension to a dynamic system, the simplest of which is a linear nanoparticle trajectory towards or away from the nanofiber surface. This trajectory can be described by the general linear form

$$d(t) = Rt + d_0 \tag{11}$$

where R is the constant particle velocity, t is time, and d_0 is the initial position of the particle relative to the fiber surface. For this case we define a negative particle velocity as a particle moving towards the fiber, while a positive velocity is a particle moving

away from the surface. Plugging this into Equation (9) and evaluating the indefinite integral results in

$$I_{linear} = A\left(-\frac{\tau}{R}\right)\exp\left(-\frac{Rt+d_0}{\tau}\right) + B \tag{12a}$$

where we still get an expression similar to Equation (10a) with a decaying exponential, a coefficient, and a background term. Again in the limit that the particle is moving at a really far distance away from the fiber where $d_0 \gg Rt$ the scattering intensity is approximately the background value. When the particle is really close to the fiber, the total scattering will depend on how long the exposure time is set. If we evaluate the definite integral from an initial time $t_i = 0$ to a final time $t_f = t_{exp}$ we obtain

$$I_{linear} = A\left(-\frac{\tau}{R}\right)\left[\exp\left(-\frac{Rt_{exp}+d_0}{\tau}\right) - \exp\left(-\frac{d_0}{\tau}\right)\right] \tag{12b}$$

Equation (12b) is equivalent to the difference in scattering intensity of a static particle at the final and initial times of the exposure time multiplied by a constant factor

$$I_{linear} = \left(-\frac{\tau}{Rt_{exp}}\right)\left[I_{stationary}(t_f) - I_{stationary}(t_i)\right] \tag{12c}$$

Here, we assume the background is equivalent at both times and it is eliminated in the subtraction.

Experimentally, this system can be realized by controlling particle movement using an AFM tip as exemplified in [63]. In this experiment, we prepare an 80 nm gold nanoparticle on the tip of an AFM and bring it in contact with the nanofiber surface in a controlled manner using a linear approach and retraction of the AFM

cantilever at a set rate, R, while collecting the scattering from the particle in the far field. The scattering profile is shown in Figure 6.3.
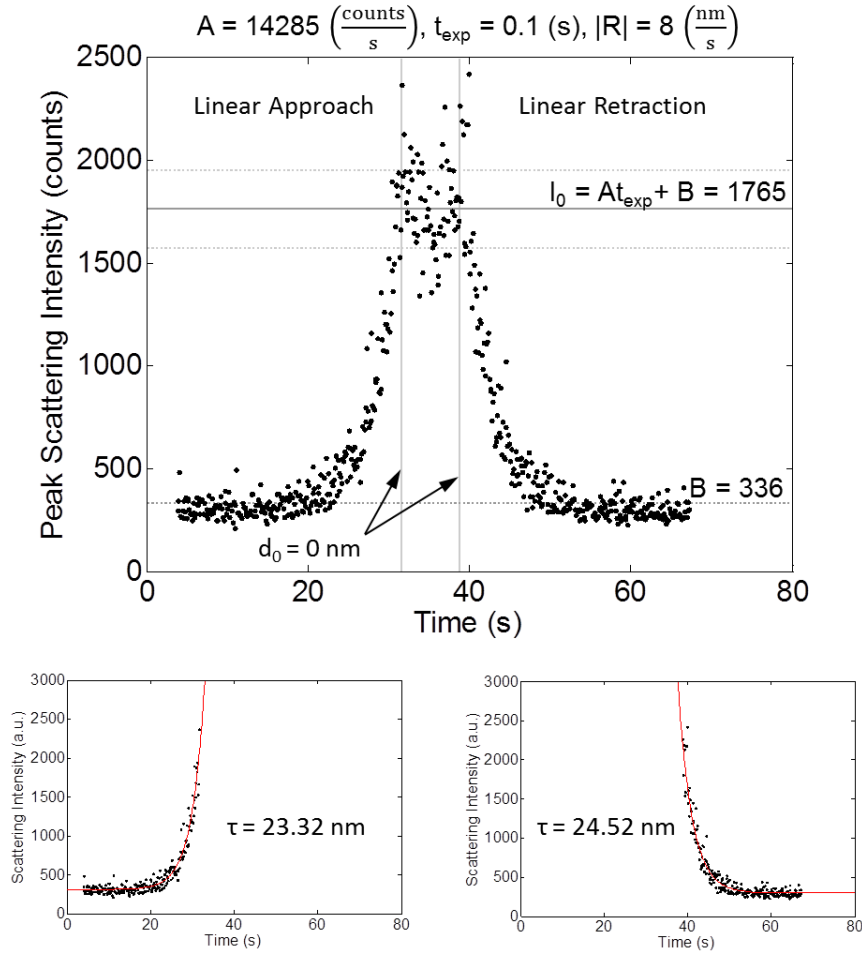
Figure 6.3. Scattering intensity from a linearly moving particle attached to AFM tip. Scattering from an 80 nm citrate-coated gold nanoparticle in time as it is brought closer to the nanofiber surface (linear approach regime) with a velocity magnitude, $|R|$, of 8 nm/s and retracted from the surface (linear retraction regime) at the same rate. The plateau region in the center represent the nanoparticle contact where the cantilever continues to move towards the surface, but the particle cannot get closer therefore the intensity is flat. At the center of this plateau region the direction of the cantilever changes and retraction begins. The flat regions at the beginning and end of the intensity plot show the background scattering. The bottom two plots are the fits of the approach and retraction region to Equation (12a) to obtain the scattering decay constant for the fiber, τ. This fiber is different from the fiber used to collect all the data in Chapter 5.

Here we do not know the decay constant of the scattering profile, τ, but we can use the shape of the scattering curve to back it out. We know the total time of the approach and retraction, and we can assume that the flat part of the intensity trend in time corresponds to the time when the nanoparticle is touching the nanofiber surface. Additionally, if we assume the particle started far away from the fiber well below the noise floor of the CCD, then we can use the initial part of the intensity curve as an estimate of B. Knowing this, the intensity in the plateau region of the curve can be averaged to get a value for A, since we know the exposure time of the camera. All these parameters can be used to back out the fit for the decay constant, τ. In this way, the AFM method can be used to calibrate the scattering intensity-distance profile of the fiber without a layer-by-layer polymer deposition. The extracted parameters here make sense with what is expected for the SnO_2 fibers of similar size and using 80 nm gold nanoparticles, but as the previous discussion highlighted, a more thorough analysis of the particle intensity under different exposure times and using different particles might give more accurate values.

6.4. Size Trends Revisited

With evidence that this general expression is applicable to multiple different classes of nanoparticle trajectories, we can reexamine the experimental trends with particle size presented in the previous chapter. Using the exposure time analysis in the previous sections we can also account for how the scattering intensity might change at any given distance as the size of the particle changes. To do this we perform the same analysis as in Section 6.2, but as a function of different particle sizes, to get an

empirical trend that describes the change in scattering rate. The result of this trend for the 4 different particle sizes simulated in the Chapter 5 is summarized in Figure 6.4–1. The expression for the scattering rate at contact as a function of particle size is

$$A = 0.39(\text{particle diameter})^{1.31} \tag{13}$$

The value for this faster-than-linear trend makes sense compared to the experimentally derived relation for dielectric particles by Prieve and Walz in [66] as the scattering here is due to plasmonic particles.

We can also use this exposure time analysis to examine how the difference in normalization between the experimental and theoretical data affects the quantified signals. In Figure 6.4–1 the ratio of the contact scattering rate to the waveguide output scattering rate is shown. By using these ratios, it should be easy to transform the normalized experimental data to a form that is more informative of the proximity of the particles to the surface. It is expected in a perfect set of experiments that the waveguide output, I_{output}, would be constant, and thus dividing the experimental data by this ratio (corresponding to the appropriate particle size) should both account for the fluctuation in the coupling efficiency and also relate the data to an absolute distance. This would enable direct comparison of the experimental data to the simulated distributions. However, due to the differences in the experimental setup between each run, this value varies as seen by the different slopes of the black lines in the top row of the figure. This is complicated by the fact that the different slopes might be due to both experimental setup differences and also the change in the evanescent

field as particles attach to the fiber surface. This prevents the relation of the output-

normalized experimental data to contact-normalized data.
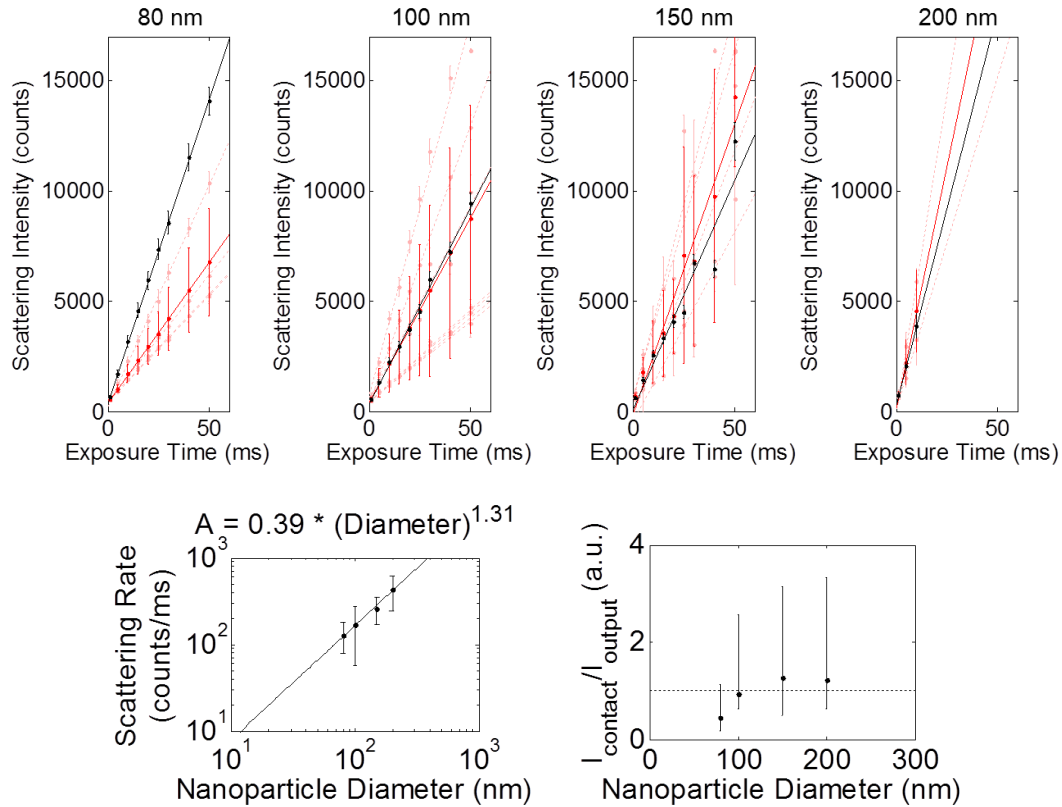
Figure 6.4–1. Exposure time analysis of particles in contact with fiber surface as a function of particle size. *Top Row*: The faint pink lines represent linear fits to exposure time data collected for individual attached particles with the error bars showing standard deviation of the intensity fluctuation over 5000 collected frames. The red line is the average fit for all nanoparticles with the error bars here representing the standard deviation of the mean intensities for all particles at that exposure time. The black line is the exposure time analysis of the waveguide output. All data for each nanoparticle size was collected from a single experimental run. *Bottom row*: The left plot is the fitted scattering rates (red line slope) for each nanoparticle size on a log-log plot with the scattering rate-size relationship obtained from the fit of the line through the points. Error bars here represent slopes fit to mean ± standard deviation of the mean particle data shown in red. The right plot is the ratio of the red line slope to the waveguide output slope for each particle size with error bars calculated in the same way as for the left plot. The line is a ratio of 1 for comparison to the data.

Regardless of this limitation on directly comparing the experimental and theoretical data, the theoretical intensity distributions as a function of particle size can now be corrected to account not only for the different electrostatic interaction but also for the difference in scattering intensity. Since we know particle size affects its dynamics also, we can begin to understand how differences in diffusion during a given exposure time will be reflected in different overall scattering intensities using the BD simulations as well. When we model the system now, we calculate A based on Equation (13) and use Equation (12c) to calculate the scattering of a particle that we assume has a linear trajectory between calculated positions, r and r_0, using Equation (8) in the BD simulations. We then accumulate these intensities until we have simulated the particle trajectories for a given exposure time. This final accumulated intensity is used as the quantified intensity, and we normalize these values to the scattering intensity from a stationary particle at contact with the same scattering rate and imaged for the same exposure time as in Equation (10b). We see that the new theory accurately predicts the experimental trends with size as shown in the simulated scattering intensity curves in Figure 6.4–2, which have a similar quality to the experimental distributions in Figure 5.4–1.

The experimental particle sizes shown here also represent the practical limitations of using the nanofiber-TIRM platform in the presently described configuration for characterizing different particles. For particles smaller than 80 nm, the scattering rate is expected to be smaller and therefore for the typical exposure times used in these experiments (5 or 10 ms) the total scattering intensity will still be

too small to be distinguishable form the background noise, much like the case for low salt concentration. This can in theory be remedied by simply using a longer exposure time, but this case will be considered in Section 6.6. For larger particles, the main limitation is the timescale of settling. As the particles become larger, the gravitational component of their potential increases with the third power of the particle radius $\left[U_{gravity} = mgh = (\rho_{NP} - \rho_{solution})\left(\frac{4}{3}\pi R^3\right)gh\right]$ where ρ_{NP} and $\rho_{solution}$ are the densities of the particle material and the suspending medium respectively, g is the gravitational constant, and h is the height of the particle. The falling out of suspension is significant for the 200 nm citrate-coated particles in the water and over the course of the 20 minute data collection only about 10 scattering events were detected within the first 5 minutes of data collection. This would imply that in order to get more statistical datasets for larger particles in this same nanofiber-TIRM configuration, multiple experimental setups would need to be repeated and the data consolidated or a higher concentration of particles would need to be examined. The higher concentration of particles might be a more efficient option, but physical differences in the system and the accuracy of the electrostatic models must be considered as the assumption of non-interaction particles in the BD simulations may no longer hold. Furthermore, this flocculation may not necessarily be a limitation for studies of particles in biological conditions as the incorporation of fluid flow may agitate the colloidal system enough to prevent settling.
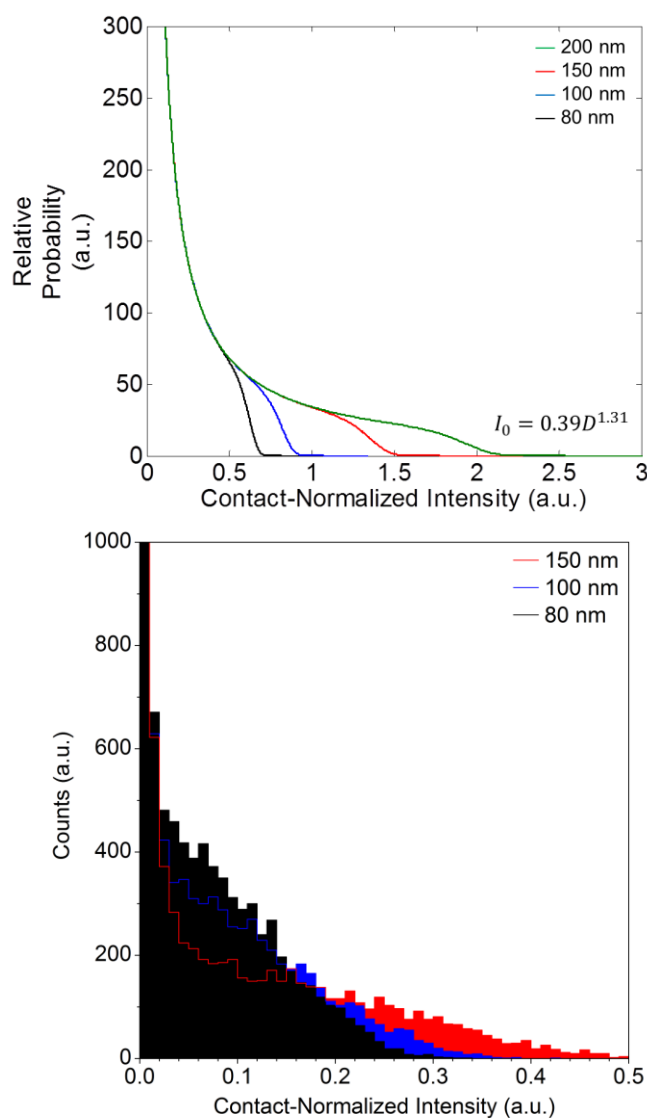
Figure 6.4–2. Theoretically predicted and simulated intensity distributions as a function of particle size corrected with varying contact scattering. The top plot is the PDF calculated from Equation (6b), here with a contact scattering value determined by particle size from Equation (13). The bottom plot shows scattering intensities calculated using Brownian dynamics to simulate particle trajectories near a wall under the influence of EDL interactions for citrate-coated nanoparticles of varying size near SnO_2. Here only distributions for particle sizes experimentally investigated are simulated. Intensities are calculated similarly to Figure 5.2–3 for a 5 ms exposure time.

6.5. Robustness Against System Heterogeneity

One of the benefits of the nanofiber-based TIRM setup described in Chapter 2 was that it was a means of efficiently collecting high-throughput single-particle interaction information for solution-level characterization similar to DLS. The main advantage of this approach was that this technique was less sensitive to sample contamination, enabling the accurate characterization of colloidal systems without the need to filter the particles by size. For traditional DLS, this is almost always necessary due to the inherent heterogeneity of batch-synthesized nanoparticle samples.

To test the robustness of this technique against particle size skewing, we collected data on mixed solutions of 80 nm and 150 nm CNPs in 0.1xPBS collected with a 5 ms exposure time. This analysis is now possible because we can account for the difference is scattering intensities of the two sizes of particles in solution. We first collected control runs with only 80 nm particles and only 150 nm particles, then collected a 50:50 mixture of the two samples as well as mixtures of a 25:75 ratio and 75:25 ratio of the particles solutions. We also compared the experimental runs with the Brownian dynamics simulations. The experimental and theoretical results of the scattering intensities are shown in Figure 6.5–1.
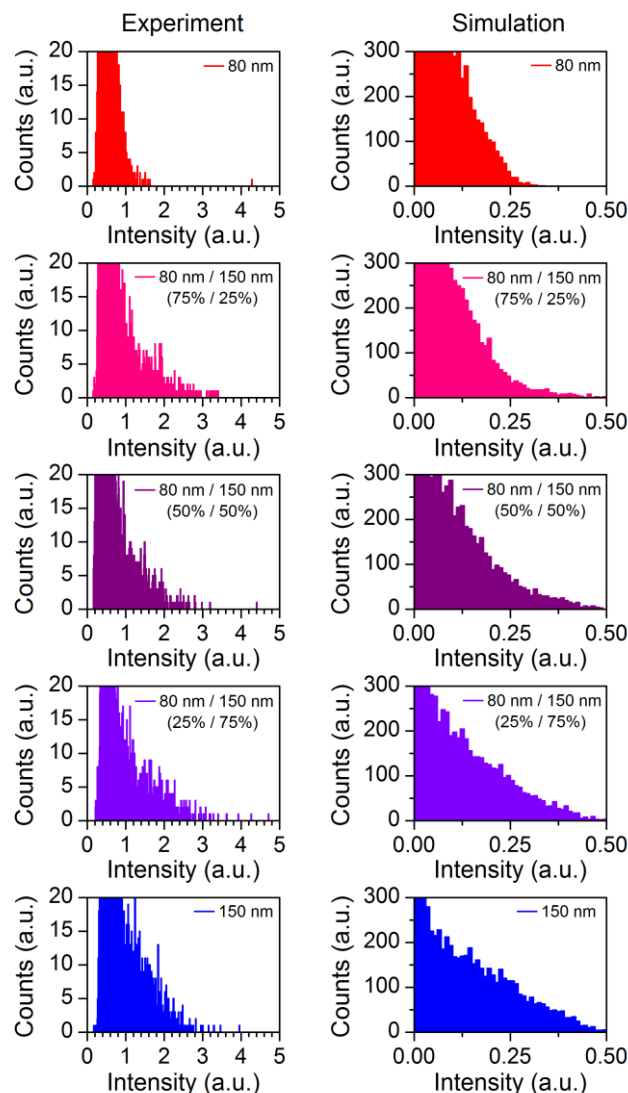
Figure 6.5–1. Experimental and simulated intensity distributions of solutions with a mixture of particle sizes. 80 nm and 150 nm citrate-coated gold nanoparticles are mixed in various proportions in 0.1xPBS. Experimentally collected (5 ms exposure time) and quantified intensities at are shown in the left column where the peak intensities are normalized to the waveguide output. The right column shown BD simulations for the same experimental conditions, using size-based contact scattering values.

While the shape of the distributions changes as a function of the relative proportion of the different populations, it is evident by the qualitative trends of the mixtures that the presence of multiple populations of particle size will not skew the

data like with traditional DLS. In fact, the agreement with the theoretical simulations suggest that this platform has potential to characterize the solution-level interaction of real colloidal solutions with non-specified surfaces, accounting for the polydispersity of the sample. Theoretical simulations of samples with varying polydispersity are shown in Figure 6.5–2 and show clear qualitative differences. This is a major benefit of this platform. In practice, it will require much more thorough analysis of the data and the experimental procedure to actually derive quantitative polydispersity values, but this analysis present a novel capability that is unique to TIRM systems.
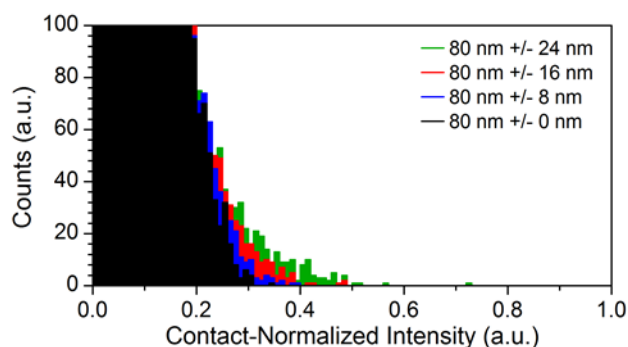
Figure 6.5–2. Simulated intensity distributions of samples with varying polydispersity. A nominal system of citrate-coated particles in 0.1xPBS is simulated using the size-dependent scattering intensity with a Gaussian particle size distribution with mean 80 nm and varying standard deviations.

6.6. Stochastic Particle Trajectories and the Problem of Parameter Estimation

With the development of the scattering intensity data collection model, we were able to account for the difference in scattering rates for different size particles. However, we can also look at how differences the collection time affect the quantified intensity signal and what that means for relating these collected intensity distributions to the theoretical distributions calculated from Equation (5). The effect of exposure time was already alluded to in Chapter 5 where the theoretical normalized intensity distributions were larger than the simulated distributions. This trends with exposure time was examined further both experimentally and with the simulations as shown in Figure 6.6–1. The experimental intensity distributions shown in the left plot were collected for a prepared 80 nm citrate-coated nanoparticle sample in 0.1xPBS. Here, the experimental setup was undisturbed and the only difference between distributions was that the camera settings were changed. The BD simulation distributions are shown in the center plot and, using the intensity-distance relationship from Equation (1) (shown in the inset), the intensities were converted to distances whose corresponding distributions are shown in the right plot.

The actual distance distribution of the particles from the BD simulation is shown as the dotted line in the right plot and this should be the same for all distributions as the colloidal system did not change at all. It is clear that changing the exposure time also changes the intensity distribution (experimentally and in the simulations), and this change corresponds to the idea presented in Chapter 5 where the

difference between theory and simulation is due to the finite exposure time of the simulation versus the physically impossible 0 ms exposure time of theory. As exposure time increases, the normalized intensity distribution gets shifted to smaller intensities. If we consider the non-normalized intensities, they should increase with increasing exposure time as the integral of Equation (9) would suggest. However, because we normalize to a stationary particle at contact, see from these simulations that the constant scattering increases faster with exposure time than the moving particle. This makes sense comparing Equation (9) and Equation (10b). The longer the exposure time, the large this discrepancy between the two increasing intensities.
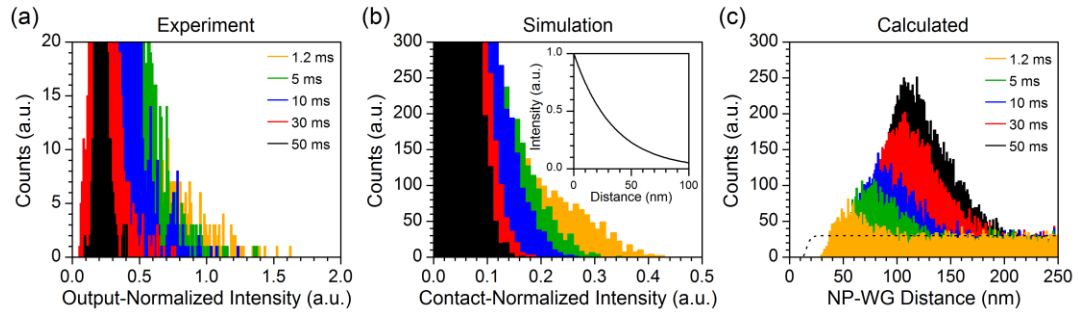
Figure 6.6–1. Effect of exposure time on experimental and simulated distributions. *Left*: Experimentally measured and quantified scattering from 80 nm citrate-coated gold nanoparticles in 0.1xPBS collected at varying exposure times, normalized to the waveguide output. *Center*: BD simulation of the experiment, normalized to the scattering of stationary particle at contact. The inset shows the intensity-distance calibration curve described in Equation (1) with a decay constant of 34 nm and contact scattering of 1. *Right*: Theoretical distance PDFs obtained from calculating the distance values from the simulated intensities in the center plot using the calibration curve shown in the inset. The theoretical distance distribution for the system calculated using Equation (5) is shown as the dotted line (corresponding to intensity data collected with 0 ms exposure time) scaled so the flat portion of the theoretical PDF coincides with the flat portion of the simulated PDFs.

Using Equation (1) for the distance conversion now highlights the difficulty in estimating the parameters from the experimentally obtained intensity distributions and using the electrostatic models of Equation (7). We know by nature of the experiment that all the different distributions in Figure 6.6–1 all correspond to the theoretical distribution shown by the dotted line, and it is really only this dotted line that we can extract quantitative parameter values because that is what the analytical model describes. However, experimentally we can never collected data that will results in this theoretical distributions because we always need to collected scattering intensities using finite exposure times. Furthermore, use of Equation (1) shows that not only is the data shifted to larger distances, but there is the formation of an anomalous population in the distance distribution, which should not be there as there is no physical mechanism in the simulations that would result in an accumulation of particles in this way.

This problem may be remedied by using a different intensity-distance relationship. We already developed a different model of this relationship that accurately describes the experimental data, but the integral form of Equation (9) cannot be used to convert intensities to distance. The main problem here is that the intensities obtained using a finite exposure time are not actually related to individual distances, but rather they correspond to particle trajectories. Using the BD simulation, we can invert the collected intensity information to map out the distribution of particle positions that underlie each quantified intensity. This is plotted for different exposure times in Figure 6.6–2.
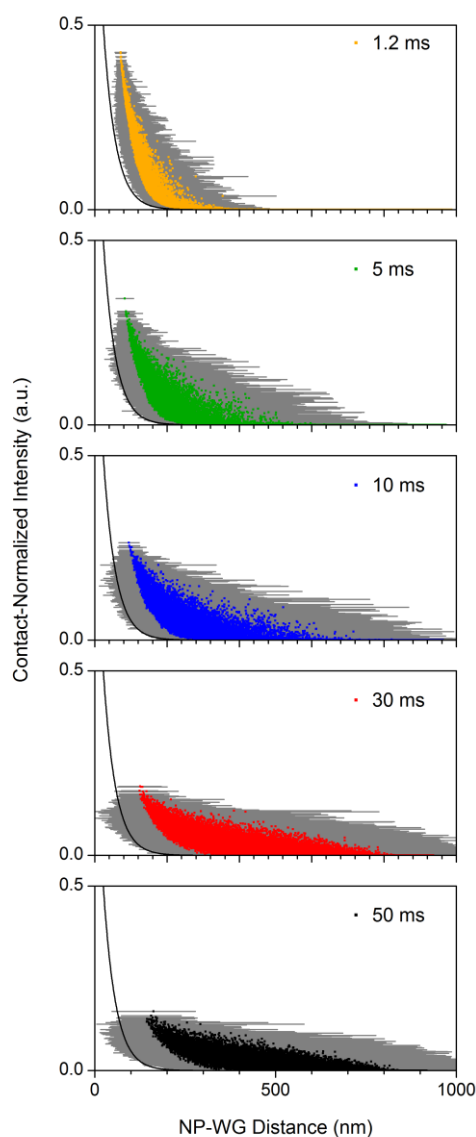
Figure 6.6–2. Intensity-trajectory relationship obtained from BD simulations. Lines representing particle trajectories plotted at the quantified intensities for different exposure times. The colored scatter plot is the mean position of each trajectory while the gray line spans ± the standard deviation of positions in the trajectory. The nominal intensity-distance relationship of Equation (1) is plotted for comparison with contact scattering equal to 1 and decay constant equal to 34 nm.

These plots represent the simulated trajectories of the particles as a mean value

(colored data point) and ± the standard deviation of positons (span of the gray line),

and this is plotted at the intensity quantified as a result of that trajectory using the relationship of Equation (1) with I_0 equal to 1 and τ equal to 34 nm, plotted as the black line for comparison in all the plots. From these plots it is clear that as the normalized intensity approaches is maximum value for each exposure time, the number of different particle trajectories that can result in that intensity decreases. In theory, the absolute maximum intensity should related to a single particle trajectory with zero standard deviation and mean equal to the absolute closest approach of the particle allowed by the electrostatics and thermal fluctuations of the system. As the intensities decrease, many more particle trajectories can result in the same intensity, which is shown by the higher density of trajectories at low intensity as well as the wider spread of position standard deviations. The question of what analytical intensity-distance relationship is appropriate for signal transformation still remains, however. While these plots give us more information about the intensity relates to particle trajectories, these trajectories were still obtained by using nominal values input into the BD simulation. Therefore, it would seem that we are at an impasse because the parameters we want to extract from the distributions also affect these intensity-distance plots.

To understand this problem further, it may be useful to consider why this data is different from other traditional TIRM datasets. The Brownian motion of a freely diffusing nanoparticle in our case can be represented by a random walk, or what is called a Wiener process. [67] The accumulation of the piecewise linear trajectory of

the simulated particle motion done in the previous sections results in an expression that can approximate the dynamic scattering from a Brownian particle:

$$I_{stochastic} = \sum_{i=1}^{N} I_{linear,i} \tag{14}$$

In the limit that the time between t_f and t_i goes to zero, the summation will be over infinitely many terms, with each term representing close to zero change in intensity, but this total summation will then essentially become an integral over the stochastic trajectory of the particle as in Equation (9). The influence of a surface and the EDL excludes some possible positions, and thus the trajectories are bound on one side by an electrostatic potential, but open on the other side. A similar situation occurs with a particle in a potential well. This can be represented by a mean-reverting random walk, or what is called an Ornstein-Uhlenbeck process, [68] and is typically realized in the traditional planar TIRM setup, but also related to a tethered or attached particle configuration. Similar to the freely diffusing particle case, each quantified intensity represents a random one-dimensional trajectory of the nanoparticle in the surface-normal direction. However, for this situation the trajectory is bound between two positions and therefore the particle only samples those positions in between. From a statistical point of view this is an easier system to work with. By representing an Ornstein-Uhlenbeck trajectory with a mean position, eventually the entire potential profile will be mapped because of the boundedness of the system. This is why it is possible to use Equation (1) for a traditional TIRM setups. On the other hand Equation 1) is not applicable for the nanofiber-TIRM setup in a non-bound particle configuration because a system profile with possible positions unbound on one or both

sides is impossible to map out using a one-to-one mapping. The unboundedness of the profile precludes mapping of the entire profile.

Chapter 6, in part, is currently being prepared for submission for publication of the material. (Villanueva, Joshua, Qian Huang, Gaurav Arya, Donald. J. Sirbuly) The dissertation author is the primary investigator and author of this material.

Chapter 7

Nanofiber TIRM with Mechanical

Feedback

7.1. Introduction

Atomic force microscopes (AFM) and optical/magnetics traps are useful for measuring molecular level forces and mechanically characterizing nano-scale systems for a variety of applications. [5,40,69–71] Particularly in areas of chemistry, materials science, biology, and medicine, these technologies have played an important role in studying the underlying physical mechanisms of various chemical interactions and physical phenomena that occur across several length scales (nanometers to micrometers). Examples include the mechanical properties of advanced soft materials and tissues, [72] the stiffness of cells in diseased and healthy states, [73] and the binding strength of specific ligand-receptor interactions and drug-target complexes. [74] However, because of the larger size of the transducer components (micron-sized cantilevers and trapped beads) and complex control/feedback mechanisms, it is often difficult to use these technologies to investigate mechanical phenomena within systems, beyond their surface. [69,75] Furthermore integration of AFM or trapping setups with multiplexed read-out and high-throughput analysis schemes (e.g., lab-on-a-chip and biodiagnostic devices) remains challenging despite the need for statistical datasets to understand the inherently stochastic nature of systems at these length scales. [37,73,75] While many sophisticated AFM and trap systems have been built that can achieve high force and displacement resolutions, [36,39] there is an immediate need to develop alternative transducer

designs that can facilitate high-throughput nanomechanical studies *in situ* inside of a material.

One method of addressing this size issue is to use a transducer that operates based on the mechanical response of a compressible polymer thin film. In principle, such a system could be synthesized on a probe of arbitrary size and shape to suit the desired application, relying only on a characteristic force-indentation profile to quantify nano-scale events that physically deform the polymer. Moreover, by eliminating the need for a large cantilever arm, piezo-stage, or high numerical aperture objectives, the compact design could offer a new dimension of portability and integration for nanomechanical studies. For example, small optical nanofiber platforms [76] could leverage the compressible properties of a soft polymer cladding to provide mechanical resistance and feedback for individual plasmonic optical transmitters that decorate its surface. Forces under investigation would displace these transmitters into the cladding, within the fiber's evanescent field, and can be measured in the far-field via indentation-sensitive scattering intensity modulation. [64] The one-dimensional structure and angstrom-level displacement sensitivity of these systems are promising features for developing nano-scale analytical alternatives to AFM and trapping technologies that can probe diverse intracellular environments. [75] Additionally, there is a particular interest in utilizing polymeric systems as sensing elements because of the diverse catalogue of advanced stimuli-responsive materials being developed. [77–79] Coupling the capability of fine mechanical measurements

with one of these stimuli-responsive systems is an appealing design for a versatile multi-functional probe.

Development of this new class of mechanical transducers requires a well characterized force-indentation profile for accurate force measurements. However, because the motivation for these transducers is largely application-orientated, it would be difficult and inefficient to design and optimize a new polymer film on an individual-experiment basis. In this work we propose a general polymer brush indentation model to guide the development of such transducers, from a bottom-up synthetic approach, aiming to help circumvent guess-and-check design methods for these thin films. The model is formulated based on an application of Alexander-de Gennes polymer scaling laws, via simple geometric arguments, to an elastic Winkler foundation representation of a thin compressible film. We start from a single-chain perspective to describe the packed structure of the brush, but depart from the traditional free energy treatment of these systems under loads to derive an expression for the single-chain stiffness that also incorporates the linear elastic modulus of the compressible layer. The latter is useful for characterizing these systems in terms of a quantitative material property for comparison among different mechanical transducers. In doing so, we develop a new hybrid model that bridges a molecular-level thermodynamic analysis and a macroscopic continuum theory. This enables us to begin to understand how the fine molecular structure can influence bulk mechanical properties, facilitating the bottom-up optimization and top-down characterization of these transducers with a single model.

7.2. System Description and Model Formulation

7.2.1. Previously Established Compression Models

Development of a new indentation model is largely driven by a need to understand the mechanical behavior of the transducer across multiple length-scales. On the one hand, many traditional indentation models are rooted in Hertzian contact mechanics and formulated based on a continuum treatment of a compressible sample. The original work formulated and solved by Hertz [80] and Boussinesq [81] considered the changing contact area between two deformable bodies as they are forced together under different loads, resulting in a varying pressure distribution across the contacting surfaces that depends on the bulk elastic properties and shapes of both materials. Applying a load to a compliant surface via a rigid indenter, a relation between force and indentation distance was derived. Sneddon expanded on this idea and derived expressions for the general case of axisymmetric solids indenting elastic half-spaces. [82] With the advent of micro- and nano-analytical instrumentation like AFM, these models were used to back out the bulk elastic moduli of materials from experimentally obtained force-indentation curves. As trends towards investigating smaller systems progressed, various adjustments to the Hertzian model were developed by several researchers to account for different phenomena at these scales that affected the force curves in different ways. Of particular interest for compact films, Dimitriadis' formulation accounted for the finite thickness of thin, elastic materials. [72]

Along the same lines, simpler models for describing the force-indentation relation between an indenter and a compliant foundation were developed by Winkler, [83] who assumed that the local indentation of a material was proportional to the local pressure. This established the bed-of-springs representation of an elastic film, of uniform height, on a rigid substrate. As Kerr summarized, [84,85] several improvements to the Winkler elastic foundation were also derived to model the force-indentation relation more accurately by increasing the complexity of the spring foundation. Mathematically, these adjusted models involved higher order terms that could be understood mechanically by the addition of shearing and bending layers over the original bed-of-springs foundation. Popov [86,87] and Heβ, [88] by their methods of dimensionality reduction, discussed the similarities between the continuum and elastic foundation approaches and defined spring constant criteria for the latter model that would result in exact solutions calculated from the former. This drastically simplified the mechanical characterization of flat elastic films for certain simple indenter geometries. However, despite the ubiquity of this macroscopic treatment of thin film indentation mechanics, both Hertzian and elastic foundation theories do not address the molecular-level structural elements of these systems.

From a thermodynamic standpoint, much of the work describing thin polymeric films and the conformations of chains in grafted brush systems can be traced back to the free energy balances examined by Flory [89] and Huggins. [90] In their work, the characteristic size of a linear polymer chain in solution was related to the number of monomers in the chain by balancing the energetic costs of chain

extension and collapse, respectively. The former reduces the conformational entropy of the system, while the latter increases the internal energy via enhanced monomer-monomer interactions in a denser state. This characteristic length scale, called the Flory radius, R_F, can also be described by the self-avoiding walk statistics of the monomers' spatial distribution, and describes the size (diameter) of a spherical volume (often referred to as a correlation blob) that the chain will occupy under thermodynamic equilibrium. The size of a real, free chain in a good solvent is approximated as:

$$R_F = aN^{\frac{3}{5}},\tag{15}$$

where a is the length of a single monomer, N is the number of monomers in the chain (equal to the molecular weight, MW, of the chain divided by the molecular weight of the individual monomer, m), and the good solvent condition implies that the temperature-dependent interactions between the polymer and solution are stronger than the monomer-monomer and monomer-substrate interactions.

Extension of Flory-Huggins theory was carried out by Alexander [91] and de Gennes [92,93] who applied the thermodynamic analysis of polymer systems to grafted and adsorbed polymer brushes. The fundamental construct of Alexander-de Gennes theory says that the characteristic correlation blob size where the chain's monomers behave according to self-avoiding walk statistics is dictated by the spacing between chain grafting sites, D, in a brush system. [94] Because the entirety of the chain will not fit in a blob of size D if D is smaller than R_F, the chain will tend to extend along its free dimension to minimize the free energy of the packed chain

resulting in a linear array of correlation blobs. Balancing the entropic cost of extension and increased internal energy of the system leads to calculation of the equilibrium brush height, t, that is a product of the lateral geometric confinement of each chain. The grafting site spacing, which is approximately the inverse root of the grafting density, affects the overall thickness of the brush as

$$t = Na^{\frac{5}{3}}D^{-\frac{2}{3}} \tag{16}$$

In this way, Alexander-de Gennes theory extends the applicability of self-avoiding walk statistics to a brush system based on a boundary condition imposed by the nano-structure of the film. Since this mechanism of chain extension occurs when D is smaller than R_F, only under this condition is Equation 16 valid. Where D equals R_F is the distinction between the polymer brush regime ($D < R_F$) and the mushroom regime ($D > R_F$), the latter consisting of sparsely grafted chains in non-interacting domains on the film substrate and is not addressed in the model. [95] Improvements to this free energy analysis were done by Milner *et al.* who derived a parabolic distribution of the chain ends using mean field theory. [96] The application of forces to these brush systems lead to free energy expressions for individual chains that depend on the compression distance. [97] By taking the derivative of the single-chain free energy with respect to the indentation dimension, force expressions could be backed out. Although these models could be applied to polymer brush compression, and described the system in terms of chain length and grafting density, there was no explicit term that could be backed out and related to a bulk mechanical modulus.

7.2.2. Hybrid Mechanistic Compression Model

Bridging the molecular level thermodynamic treatment of polymer films with the macroscopic theories of thin elastic film indentation is possible by making a few geometric assumptions about the microstructure of a polymer brush. With the Alexander-de Gennes representation of each polymer chain in the brush as a linear array of correlation blobs, it is a reasonable extension to consider each chain as a single cylindrical volume with diameter, *D*, and height, *t* (Equation 16). Additionally, if we assume each chain is identical and contributes independently to the mechanical response of the transducer, the entire polymer film can be modeled as a close-packed array of these right cylindrical volumes as in the case of the simplest Winkler foundation model. This system is depicted in Figure 7.2A. In this way we have formulated a nano-structured continuum representation of the film whose partitioning is dependent on thermodynamically derived scaling laws. This allows us to obtain macroscopic material properties of the film for mechanical characterization and also to examine the brush packing structure for bottom-up force response optimization using a single model. To obtain a force-indentation relationship, we now only need to derive the form of the proportionality (the spring constant) for each cylindrical volume. Then by accounting for the shape of the indenter, the local forces can be calculated from the local indentation and summed for a total force response. This is summarized in Equation 17:

$$F_{tot} = \sum_{i=1}^{N_C} F_{Si} = -\sum_{i=1}^{N_C} k_i \Delta z_i, \tag{17}$$

where k_i is the stiffness of the ith compressed spring and $\varDelta z_i$ is its indentation. N_C is the total number of chains compressed by the indenter, which will be a function of the size of the indenting sphere and its indentation distance into the polymer film, $N_C(\varDelta z_{max}, R_{NP})$, following contact mechanics. To reduce some of the ambiguity in the model with respect to the indenter, we have assumed a rigid sphere of radius R_{NP}. [98]
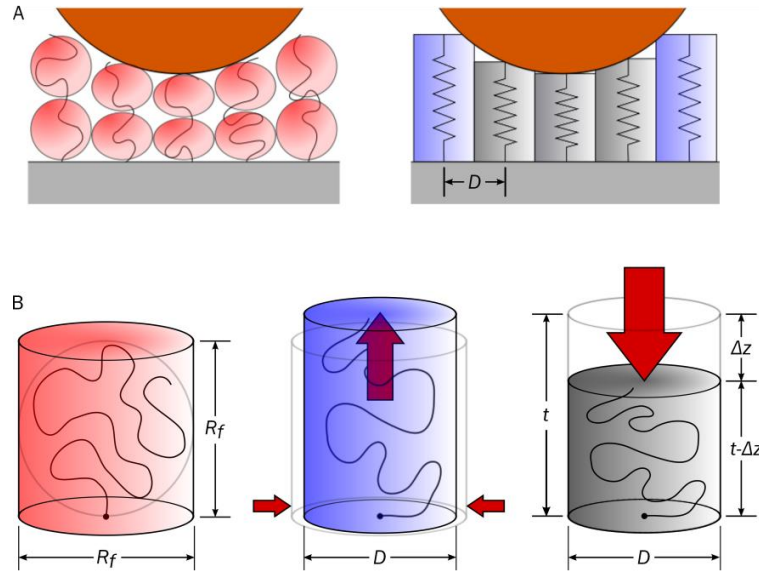
Figure 7.2. Schematic of a polymer brush system compressed under a spherical indenter. In the upper panel (A), the Alexander-de Gennes brush is shown on the left with each chain comprised of multiple correlation blobs of size D determined by the spacing between grafting sites. The corresponding cylindrical volume structured brush used in our formulated model is depicted on the right. In lower panel (B), the unpacked single-chain volume (V_M) is on the left, the packed and uncompressed volume (V_B) in the center, and the packed and loaded cylinder volume (V_L) on the right. V_M is approximated as a cylinder of diameter and height equal to the Flory radius, R_F, rather than a single spherical correlation blob. For V_B the confinement of the brush geometry is effectively loading the brush laterally, which causes expansion in the vertical direction (inward and upward pointing red arrows). The force compressing V_L is represented by the downward red arrow.

With the shape and size of the indenter defined and its indentation distance the independent variable, the term that remains unknown in Equation 17 is the single-

chain spring constant, k. Describing the film nano-structure by subunits of simple right cylinders, we derive a form of k that depends on the deformation of these volumes. This keeps the model general enough to be widely applicable to any polymer brush system. The deformation of a bulk material, though, requires the use of a generalized Hooke's law where the modulus of the material is a tensor, but we aim to derive an equation for the scalar value of the single-chain stiffness. To overcome this challenge, we neglect any shear components of the stress required to indent the thin film and assume that changes in an occupied chain volume are caused by an isotropic pressure. In this way we are able to decouple and simplify the system of equations from a generalized Hooke's law, and transform a 3-dimensional film deformation into a 1-dimensional force response. By approximating the occupied space of the chain as a continuous, compressible material, we can relate its volume change to the local pressure required for its deformation using the bulk modulus equation, [99] which can be rearranged into the form:

$$\Delta P = -K\ln\left(1 + \frac{\Delta V}{V_0}\right), \tag{18}$$

where ΔP is the change in pressure from an initial state to the final state, K is the bulk modulus of the material, ΔV is the change in volume between final and initial state, and V_0 is the initial volume. The change in volume is assumed to be negative under compression, therefore the leading negative sign in Equation 18 ensures that with increasing system compression, the pressure increases (becomes more positive). Rearranging the linear form of Hooke's law, the single-chain stiffness can be related to the pressure via Equation 19:

$$k = -\frac{dF_S}{dz} = -\frac{dF_S}{dz}\frac{A}{A} = \frac{dP}{dt}A = \frac{dP}{dD}\left(\frac{dt}{dD}\right)^{-1}A, \tag{19}$$

where A is the cross-sectional area of the cylinder under compression (proportional to D^2) and the change in indentation, dz, is the negative of the change in film thickness, dt. Therefore, we can use Equations 18 and 19 to derive the linear stiffness of a single chain from changes in its occupied cylindrical volume.

It is assumed that the stiffness can be decomposed into two components: the first from packing the free chain into a brush structure and the second from the compression of the packed chain itself (k_p and k_z respectively). To obtain the final form of the single-chain stiffness, the volume changes from the two chain states must be derived and related to a pressure change between states (here the pressures are defined as relative to the initial pressure of the unpacked free polymer state in the mushroom regime). Figure 7.2B depicts the different volumetric states of a single-chain. The initial state of a grafted chain in the mushroom regime is assumed to occupy the volume (V_M) of a cylinder with height and diameter both equal to R_F. Upon packing, the occupied volume (V_B) of the chain is a cylinder of diameter D and height equal to Equation 16. The relative change in volume between these two states is given by:

$$\frac{\Delta V}{V_0} = \frac{V_B - V_M}{V_M} = \frac{V_B}{V_M} - 1 = \left[\frac{\left(\frac{\pi D^2}{4}\right)t}{\left[\left(\frac{\pi R_F^2}{4}\right)R_F\right]}\right] - 1 = \left(\frac{D^2 t}{R_F^3}\right) - 1. \tag{20a}$$

The final state of the chain is when it's under an axial load, and therefore the volume is equal to a cylinder of diameter D but with height t-Δz_i. The relative volume change between the packed state (V_B) and the compressed state (V_L) is:

$$\frac{\Delta V}{V_0} = \frac{V_L - V_B}{V_B} = \frac{\left(\frac{\pi D^2}{4}\right) \Delta z_i}{\left(\frac{\pi D^2}{4}\right) t} = \frac{\Delta z_i}{t}. \tag{20b}$$

Plugging Equations 20a and 20b into Equation 18 respectively and summing the two resulting pressure expressions gives the final form of the stiffness equation:

$$k_i = k_p + k_z = \frac{\pi}{4} K \left[2 \left(\frac{D}{R_F}\right)^{\frac{5}{3}} D - \frac{\Delta z_i}{\left(\frac{R_F}{D}\right)^{\frac{10}{3}} + \left(\frac{R_F}{D}\right)^{\frac{5}{3}} \left(\frac{\Delta z_i}{D}\right)} \right]. \tag{20c}$$

By plugging Equation 20c back into Equation 17, we are able to obtain the force-indentation profile for a generic polymer thin film based on the size and packing of the chains in the brush-structured transducer.

7.3. Model Trends

Examining the trends that the model predicts from both a single-chain and brush perspective can give us insight into the physical mechanisms that influence the total force response of a device that uses these compressible polymers for mechanical feedback. To mechanistically understand how local chain deformations affect the mechanical properties of the entire brush we must analyze the system in thermodynamic terms. Specifically, how changes in each cylindrical chain volume affect the free energy of the system.

7.3.1. Single-Chain Stiffness

We first discuss the limits of the model with regard to the film partitioning. As described previously, the scaling law used is only applicable to a polymer brush and requires that the grafting site spacing between adjacent chains (D) is less than the Flory radius (R_F). In the limit that D equals R_F (i.e., mushroom regime where occupied

chain volumes do not overlap) the packing stiffness (k_p) in Equation 20c only depends on R_F and thereby scales with the molecular weight (*MW*) of the chain. Additionally, Equation 16 shows that in this limit the thickness of the film (*t*) is equal to R_F so the indentation stiffness (k_z) primarily depends on the indentation (*Δz*) relative to its *MW*. Conversely, with a completely packed film where *D* approaches the size of a monomer (*a*) both k_p and k_z decrease to very small, finite values.

This *k(D)* trend for the individual chain can be explained from a thermodynamic standpoint by considering that as the chain is confined laterally the number of conformations available to it decreases, and thereby the single-chain entropy decreases. With decreasing entropy, the free energy of the chain increases, and it becomes more favorable to compress the chain axially to return it to its unstretched state. Thus the linear stiffness of the single chain decreases because packing is similar to pre-stretching the polymer. In this case there is already an intrinsic tendency for the chain to collapse, and it would be easier to compress an individual chain the larger its lateral confinement (without considering chain-chain interactions or the effect of compressing multiple chains). This decreasing stiffness corresponds not only to a decreasing *D*, but also to an increasing *t* (i.e., *k(t)* has a negative slope), which is obvious from Equation 16 where *D* is in the denominator. By the limits of *D*, it is clear that *t* is constrained to be larger than R_F and smaller than the fully extended length of the linear chain ($R_F < t < Na$).

With R_F in the denominator of both stiffness terms, *k(MW)* has a decreasing trend, which makes sense for the same reasons as the *k(D)* trend. Increasing *MW* while

maintaining a constant D results in decreasing the chain's entropy in a similar way as decreasing D with a constant MW. Again, t is shown to increase with the decreasing stiffness trend because t is proportional to MW. The bulk modulus (K) can be pulled out of both stiffness components in Equation 20c and is directly proportional to the stiffness of the chain. Yet, because K is a bulk material property, the significance of this will be discussed later in the context of the total system force response.

A nonlinear $k(\Delta z)$ is expected and goes from some finite value at no indentation to infinity as Δz approaches the film thickness (remember that Δz is negative because it describes a compression into the film). The model as formulated shows that Δz only influences k_P. The fact that k is finite and depends on the packing of the film in the undisturbed state ($k = k_P$ at $\Delta z = 0$) highlights the importance of D and MW in determining an intrinsic material property based on the nanostructure of the brush. With the pre-stretched chain in the packed brush as the baseline state, we must now consider the effect of the lateral confinement by adjacent chains. Therefore, as Δz increases in magnitude, the volume available to the chain will always decrease because its footprint is always constrained to a circle of diameter D. The effect of increasing Δz on the free energy is thus to decrease the entropy of the single chain even further. Also, as the chain is being compressed the internal energy related to the density of monomers in the cylindrical volume (distance-dependent monomer-monomer interactions; e.g., steric, electrostatic) increases. With respect to full compression, k should approach infinity at an indentation less than t because of the finite space each monomer occupies; the remaining portion of the film can be

considered incompressible. However, the hard sphere repulsion of each monomer has not been accounted for in the model, and because of this large errors are expected in the high compression regime.

7.3.2. Total Force Indentation

Our analysis of the per-chain stiffness trends in the model is important for understanding the nano-structural underpinnings of the total force-indentation profile. The total force trends though are more interesting for the purposes of predicting the mechanical response of force transducers (during optimization) and for ultimately quantifying measurements (using established systems). Parameters important for transducer design in the context of our model are K, R_{NP}, MW, and D as we have discussed in the single-chain analysis. Although of particular interest are MW and D because they constitute the parameters that directly determine the film partitioning and can be tuned during brush synthesis. In this section we examine the effect varying the each of these four parameters has on the shape of the force-indentation curve. By looking at the relative slopes of these profiles, we can begin to understand how to tune the stiffness of the force response by careful design and selection of the transducer components.
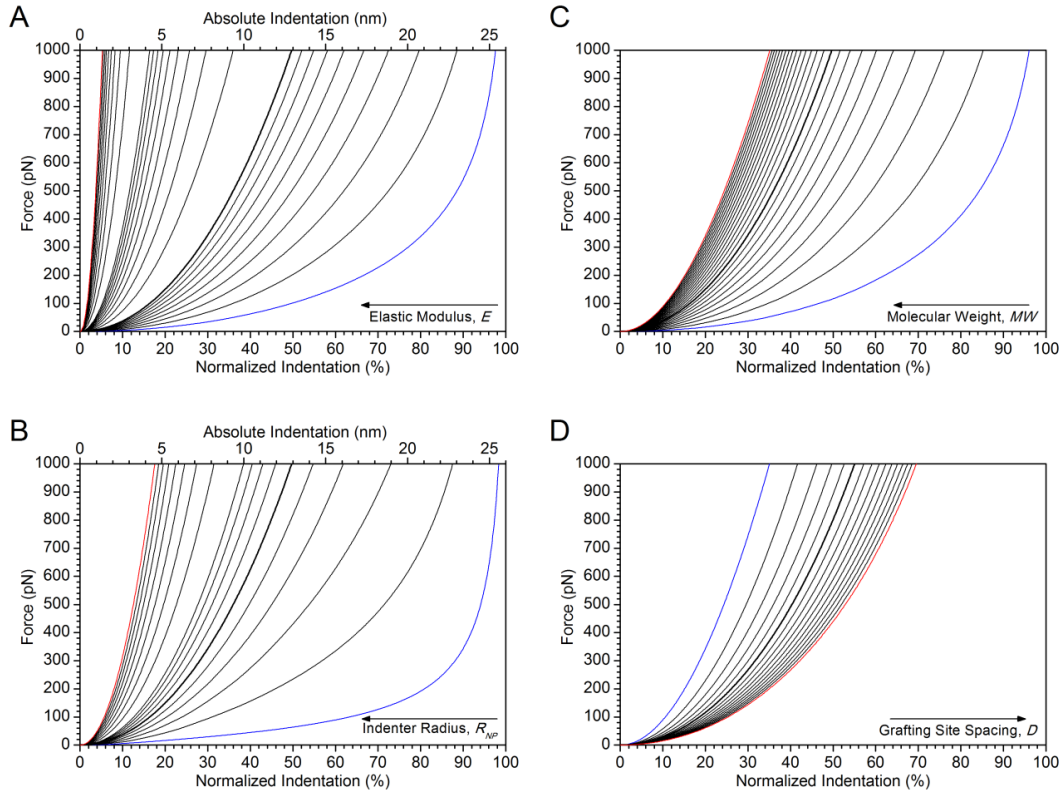
Figure 7.3. Force-indentation trends predicted by the hybrid brush compression model. Trends based on four model parameters: elastic modulus (A), indenter radius (B), molecular weight (C), and grafting site spacing (D). A baseline PEG brush (E = 1 MPa, MW = 10 kDa, R_{NP} = 30 nm, and D = 2 nm) is modeled and shown as the bolded curve in each plot for comparison with the sweeping parameter. Only one parameter is varied in each plot with the blue curve corresponding to the smallest parameter value and the largest in red. Intermediate curves increase incrementally in value in the direction indicated by the arrow in each plot. The parameter values modeled in each plot are: E = {0.1:0.1:1, 2:1:10, 20:10:100} MPa, R_{NP} = {5:5:50 75:25:250} nm, MW = {1:1:25} kDa, and D = {0.5:0.5:8} nm. The notation used here is {min:step:max}.

As described earlier, F_{tot} is calculated by summing the forces (F_{Si}) required to compress each chain under the indenter where each of these forces depends on the local indentation and stiffness (Δz_i and k_i; the latter also depends on Δz_i). An ideal brush system was modeled where the grafting site positions were determined based on a hexagonal close-packed array with spacing equal to D. Then Δz_i and k_i were

calculated based on the ith chain's position under a rigid sphere of radius R_{NP} with maximum indentation (apical indentation) of Δz_{max}. Force-indentation profiles were simulated by calculating $F_{tot}(\Delta z_{max})$ under various system configurations that affect k_i and the number of chains compressed under the indenter (N_C). The results are shown in Figure 7.3. In general terms, for each trend the curve corresponding to the smallest parameter value is plotted in blue and the largest parameter value in red. Alternatively, the increasing parameter trend is shown by the arrow direction in each plot. Each of the curves starts at zero force when the indenter is at initial contact with the film and increases to infinite force as the indentation approaches t (full compression).

The baseline system under investigation is a grafted 10 kDa molecular weight polyethylene glycol (PEG) brush with a 1 MPa elastic modulus, and a grafting site spacing of 2 nm. The indenting sphere radius is set as 30 nm. This nominal system is plotted as the darker curve in the figures for easy comparison. Because the bulk modulus is not typically the mechanical property extracted in indentation studies, we have replaced K in Equation 20c with the elastic modulus, E, by the simple relation:

$$K = \frac{E}{3(1-2v)} \tag{21}$$

where v is the non-dimensional Poisson's ratio. [99] Here we set v to be 0.3, and we use the reported ethylene glycol monomer size (a) of 0.358 nm to calculate R_F. [100] For each plot, only one parameter is varied with all the other parameters set to their nominal values as listed above.

The dependence of the force-indentation profile on E is shown in Figure 7.3A. For these trends, F_{tot} is plotted against the relative indentation of the film on the

bottom axis where Δz_{max} is normalized to t, giving the indentation percentages (i.e.,

strain). This ensures that the parametric profiles can be easily compared to one another

by examining their relative slopes alone. However, because the thickness for all

profiles plotted is the same when only E is varied, the indentation axis can also be

plotted with absolute values (top axis). As Δz_{max} approaches the nominal film

thickness of 25.8 nm (100 percent indentation), all of the trends ultimately converge to

a single curve (not plotted), but the traces show that with increasing E the parametric

curves have a steeper rise to infinite force. Larger forces are required to compress

films with higher E a certain distance. As pointed out from the single-chain analysis,

this bulk material property can be factored out of the stiffness expression, and

therefore simply scales the force curve vertically without changing t or the total

number of compressed chains, N_C. Because E is an independent parameter that is not

affected by the nano-structure of the film, it is truly a material property in the context

of our model and can be backed out of measured force-indentation curves for

characterization purposes. Furthermore, the decoupled nature of E from MW and D

suggests that slight variations in the extracted moduli of differently packed brushes of

the same polymer may be attributed to nano-structural effects.

Considering R_{NP} in Figure 7.3B, the trends present similarly to those of E

where increasing R_{NP} results in steeper profiles, and all curves converge to the same

nominal film thickness since MW and D remain fixed (here again both relative and

absolute indentations can be plotted). However, unlike the modulus trends that vary

due to changes in k_i, the effective stiffening of the force response is caused by changes

in N_C while k_i remains constant. In calculating $F_{tot}(\Delta z_{max})$ we have assumed that for the indentation of films beyond a distance of R_{NP}, N_C is held constant. For compression in this regime the indenter shape has no further influence on the force-indentation trends via changes in the number of compressed chains, and the shape of the force profiles become completely dominated by the form of the single-chain stiffness. While the same criterion was applied for calculating the modulus trends, here the rate of change of N_C with respect to Δz_{max} (i.e., $dN_C/d\Delta z_{max} = f(R_{NP})$) varies with different R_{NP} until Δz_{max} equals R_{NP} whereas $dN_C/d\Delta z_{max}$ is constant for all values of E modeled. This difference can be seen in Figure 7.3 as the slight differences in profile shapes between the R_{NP} and E parameter sweeps.

Examining the force-response trends as a function of MW and D is a little more complicated as changing either of these parameters will also change t. Therefore, here absolute indentation values cannot be plotted for these last two trend plots, and the only way to accurately compare the stiffnesses of different film configurations is to normalize Δz_{max} to t. In this way all response curves still converge to one value at full compression, and the relative slopes can still be used as comparative measure of stiffness. By normalizing the indentation, varying the MW of the chains in the brush affects F_{tot} in an opposite manner expected from the analysis of k_i. As MW increases, the stiffness of each chain decreases, but ultimately the total force shows a stiffer profile. This difference between the single-chain and brush perspectives highlights the effect of the lateral confinement due to the brush packing. In the brush case, increasing MW leads to a larger system internal energy from the additional monomer-monomer

interactions, resulting in an increase of the free energy and an effective stiffening of the force response.

Trends in the total force-indentation profile as a function of D are perhaps the most complicated to analyze in the model because, unlike the other three parameters, changes in D affect both k_i and N_C. Moreover, these two qualities are competing phenomena that affect the force response in antagonistic ways. As D decreases, k_i also becomes small as discussed in the single-chain stiffness analysis, but N_C increases in the summation which buffers the decreasing stiffness in the total force response. When we consider the normalized trends as a function of D the model predicts what would generally be expected for such systems. Decreasing D and effectively packing the chains into a denser brush will increase the stiffness of the force profile as the increasing slope indicates. The thermodynamic argument made for explaining the trends with MW applies here as well; namely, the larger free energy is due to the larger chain-chain interactions (dictated here by brush density rather than just an additional number of interactions), resulting in a stiffer film.

7.4. Comparison to Experimental Data

Our model's predictive power was validated by comparing theoretical force curves with experimentally obtained AFM curves. The films tested were PEG brushes of various molecular weights (2k, 5k, 10k Da) deposited on SiO_2 substrates via the graft-to method with a silane-based reaction [101], similar to those synthesized and mechanically characterized in our previous work. [102] PEG was selected for the study because it is a well characterized system that is chemically robust and can form

monolayers, [101] has tunable mechanical properties, [103–105] and is used in many applications as an inert biological interface. [106–108] The average number of monomers in each sample (N) was calculated from the MW assuming a monomer molecular weight (m) of 44 Da, and again R_F was calculated using Equation 15 assuming a is 0.358 nm. Based on our synthesis method, the films were assumed to be monolayers and to have chain packing densities that result in compressible thicknesses (i.e., $t_C = \Delta z_{max}(F_{tot} = \infty) - \Delta z_{max}(F_{tot} = 0)$) less than 20 nm. For each film, t_C was determined from the indentation data and used in Equation 16 to calculate D. An AFM equipped with a 30 nm (R_{NP}) SiN tip (spring constant = 0.14±0.02 N/m) was used to indent the films. The tip radius was calibrated by imaging a standard sample with sharp features [109,110] and the cantilever stiffness was quantified using a thermal tune method. [111] Because R_{NP} is much larger than t_C, the spherical indenter assumption holds true. All indentations were conducted in 1x phosphate buffered saline (PBS) to minimize the electrostatic interactions between the tip and the substrate to obtain a purely mechanical force response from film deformation.

Before we use the model in a predictive capacity and calculate theoretical force curves, a nominal value of E is required. In this study several AFM indentation curves were analyzed from each MW sample, and an average modulus for each film was backed out. Since K can be pulled out of the summation in the model expression, we can easily calculate E for particular packed brush states by examining how the theoretical curves need to be scaled to fit the experimental profiles. Here we first assume a nominal elastic modulus, E_0, of 1 MPa. By dividing the measured AFM

force at a particular indentation by the theoretical model force, a scaling factor, ε, of the nominal modulus can be extracted, and the true modulus of the film (E) can be calculated and plotted for each AFM data point according to the following equation:

$$E = \left[\frac{F_{AFM}(\Delta z)}{F_{model}(\Delta z)}\right] E_0 = \varepsilon(\Delta z)E_0. \tag{22}$$

Plotting E as a function of normalized Δz_{max} for the various PEG brushes synthesized is shown in Figure 7.4. There are three datasets for each MW, which corresponds to different AFM indentation locations on the same substrate. The 2k, 5k, and 10k samples are distinguished by color (black, red, and blue, respectively) and are ordered from top to bottom. Different AFM measurements on the same sample are distinguished by shape.

A perfectly fit model curve would show a flat trend with constant E as the film indentation increased. It is clearly seen that below an indentation of about 30% and above an indentation of about 90% (grayed out indentation regions in Figure 7.4) there are large errors in the extracted moduli. For the small indentation regime, the large fluctuations in E are due to the small force values analyzed. Here slight deviations between the model and experimental profiles are greatly magnified in the calculation of ε because the denominator is nearly zero. For the large indentation regime, sharp decreases or increases in the modulus curves are possibly due to the errors associated with defining the point of contact in the AFM data, which can shift the experimental plots laterally as contact is always set as the origin of our plots. Similar to the small indentation regime, slight misalignment of the experimental and modeled curves can result in magnified errors under high compression because the numerator is very large.

Additionally, we have noted that the finite compressibility of the chains has been ignored in the model as have any indenter-substrate interactions which can cause underestimations of the film moduli. The gradually increasing $E(\Delta z_{max})$ trends seen in Figure 7.4 for intermediate compressions (between 30% and 90%) are indicative of these underestimations. As is anticipated, the thinner films seem to be more susceptible to substrate effects, which can be seen in the steeper trends with decreasing MW. For this reason, only the data between 30% and 60% compression for the 2k film was used in the calculation of E.

By defining the packing parameter, $\mathcal{P}$, with the expression:

$$\mathcal{P} = 1 - \left(\frac{D}{R_F}\right), \tag{23}$$

we can plot the average E as a function of the packing for each respective MW film (Figure 7.4, inset). The vertical error bars are the standard deviation in E for the intermediate compression region (between 30% and 60% indentation for the 2k measurements and between 30% and 90% indentation for the 5k and 10k measurements), and the horizontal error bars are the standard deviation in $\mathcal{P}$ based on the three indentation curves collected for each MW. The extracted moduli values are 0.7218 ± 0.0171 MPa, 0.6977 ± 0.0581 MPa, and 0.5962 ± 0.0819 MPa for the 2k, 5k, and the 10k films respectively, which are consistent with the $E(MW)$ trends determined by Stan *et al.* [105] Analyzing these samples using Dimitriadis' model, [72] the moduli values are 1.100 ± 0.170 MPa, 0.780 ± 0.180 MPa, and 0.600 ± 0.180 MPa (2k, 5k, 10k, respectively), [102] which are comparable and within the error for the 5k and 10k films. It is possible that the smaller indentation range

analyzed (30% to 60%) is responsible for the larger underestimation of E seen with the 2k sample. Because of the large overlapping error bars associated with our calculated moduli, we use an average extracted film modulus of about 600 kPa to plot the theoretical force responses of all films to see how well the model predicts the form of the force-indentation profiles measured experimentally with AFM. In this way we can evaluate the predictive power of the nano-structural formulation of the model alone, where the differences between force curves are determined only by MW and D. The comparison is presented in Figure 7.5–1, which shows the experimental data (scatter plot) along with the model's curve. It is clear that there is strong agreement between the model and the experimental data. This is a promising result as predictions are reasonable even without explicitly including steric forces, electrostatic repulsions/attractions, or solvent-chain interactions in the model.
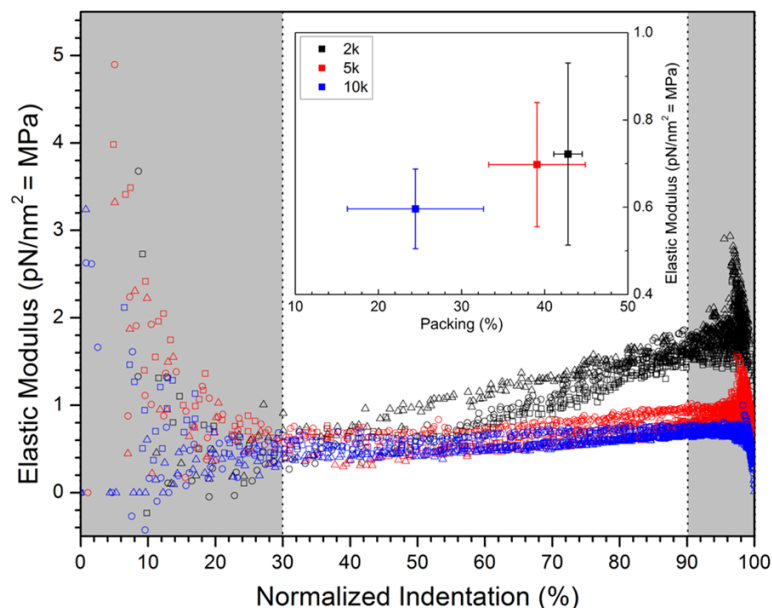
Figure 7.4. Point-by-point calculation of the elastic film modulus extracted from the experimental AFM indentation data. The data was taken on 2k (black, top scatter plot), 5k (red, middle), and 10k (blue, bottom) molecular weight brush samples. The three different shapes (triangle, square, circle) plotted for each molecular weight indicates different indentation curves taken on the same sample. Grayed regions at low and high indentations indicate regimes of poor model fitting for this modulus extraction analysis. The inset shows the average fitted modulus for each molecular weight plotted as a function of its respective brush packing. For the 2k brush, the average modulus was calculated from the data between 30% and 60% indentation, whereas for the 5k and 10k brushes, the average modulus was calculated from data between 30% and 90% indentation. Error bars represent ± standard deviation for each axis variable based on the 3 indentation curves obtained per sample.

7.5. Theoretical Transducer Sensitivity

Understanding how the force sensitivity of these compressible polymers compares to that of AFM and optical trapping systems is important if these films are going to be used as mechanical feedback in novel, compact force transducer designs. To this end we investigated the force sensitivity, defined as the smallest force resolvable by the transducer, as a function of the two main parameters relevant to the

physical packing of these films: *MW* and *D*. While *E* and R_{NP} can also influence the force sensitivity, here we are mainly interested in understanding the effect of changing the film nano-structure because application-specific design criteria of multi-functional probes can often limit the ability to readily change transducer materials.
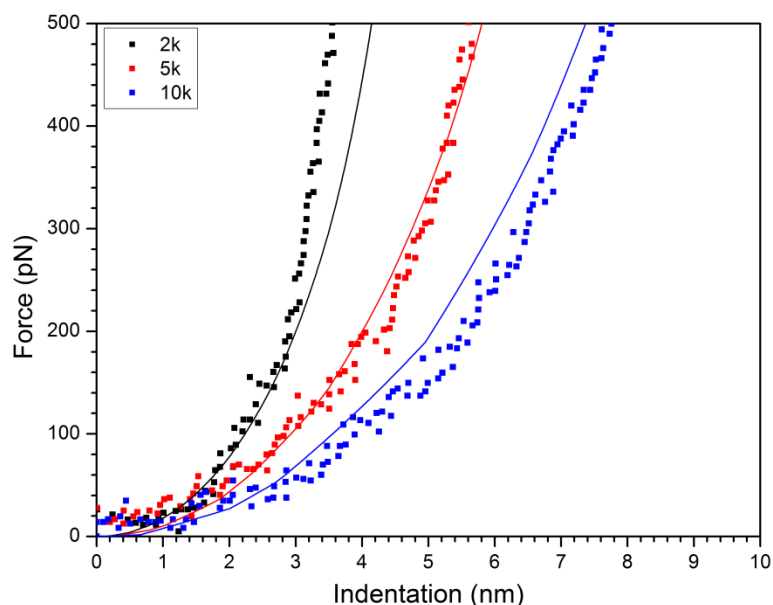
Figure 7.5–1. Comparison of the predicted force response (solid line) with individual representative AFM indentation plots (scatter points) for each molecular weight brush synthesized: 2k, 5k, and 10k (black, red, and blue curves, respectively, ordered from left to right).

Although it is difficult to define brush parameters for a generic transducer design, we can refer to the nanofiber system described earlier as an example platform to demonstrate how the polymeric transducers discussed in this work can be used in a real system, and how to identify specific design criteria for these compressible films based on desired mechanical properties. It has been shown that light-matter interactions occurring within the near-field of a fiber optic can be extremely sensitive to distance, [112] and we can leverage this, in conjunction with the work presented

here, to develop a novel, highly sensitive force probe for high throughput *in situ* (or *in vivo*) measurements. Figure 7.5–2A shows a schematic of such a nanofiber force probe where the position of plasmonic gold nanoparticles (AuNPs) embedded in the evanescent field of a tin dioxide (SnO_2) nanofiber waveguide can be tracked via their distance-dependent far-field scattering signals. Recently it was been experimentally shown that these platforms can resolve angstrom-level displacements. [64] This spatial sensitivity, which is on-par with state-of-the-art optical traps and exceeds that of current AFM technologies, [5] is crucial for unlocking the high force resolution afforded by thin, compressible polymer coatings. In this platform, a compliant polymer cladding would surround the fiber (Figure 7.5–2A, inset) and individual nanoparticles attached to the cladding would serve as independent force transducers (assuming they were spatially isolated by distances greater than the wavelength of light).

If we assume a minimum resolvable indentation distance (Δz_{max}) of 1 Å, an E of 600 kPa for a PEG-based transducer, and an R_{NP} of 40 nm, then we can plot the force sensitivity of the transducer element in the system-space determined by various packing conditions. This is plotted in Figure 7.5–2B where each force curve represents the 1 Å compression of a different *MW* film, plotted as a function of *D,* within the model constraint of *D* less than R_F. With the decaying evanescent field and distance-dependent scattering intensity, the films used in these total internal reflection (TIR) sensing schemes are also limited to thicknesses below about 20 nm to achieve the highest spatial resolutions. [64] Thickness cutoffs are presented in the figure for *MW*

and D combinations that result in films thicker than 10 nm (light gray region) and 20 nm (dark gray region), respectively. Additionally, the experimental limitations of synthesizing very dense films must be taken into account. This is shown by the green line assuming a maximum achievable film packing of 50% (i.e., $D > 0.5R_F$), where regions below the line indicate brush configurations that require high chain densities and would be difficult to synthesize. The plot also captures the predicted force sensitivity for the PEG brushes (2k, 5k, and 10k) that were analyzed with AFM in the previous section.
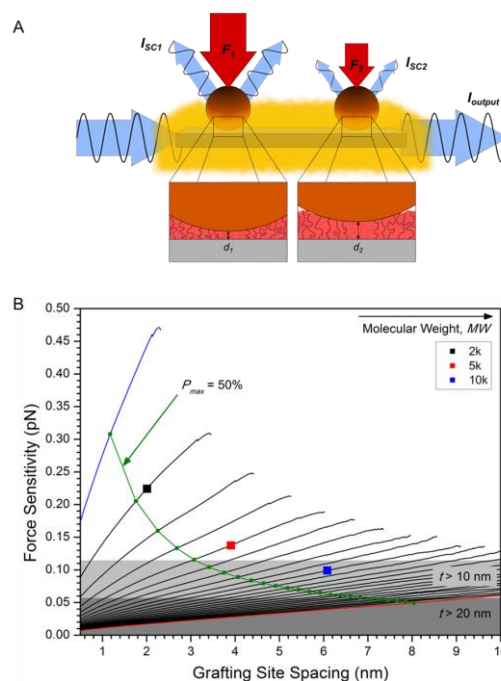
Figure 7.5–2. Schematic of a nanofiber force probe and the force sensitivity of the mechanical feedback mechanism using a polymer brush. (A) Schematic of a nanofiber force probe depicting two forces causing different particle indentations into the thin film transducer. Forces cause displacements of plasmonic nanoparticle indenters within the evanescent field that also compress the thin polymer transducer (insets). By monitoring the distance-dependent scattering of the nanoparticles in the far-field, the forces can be measured. (B) Predicted force sensitivity of a TIR fiber optic-based force transducer with 1 Å spatial sensitivity. The minimum resolvable force is plotted versus brush synthesis parameters: *MW* and *D*. Each curve represents a different *MW* (increasing for each curve from blue to red). *MW* curves are plotted for brushes between a grafting site spacing of 0.5 nm at the low end and $D = R_F$ at the upper bound. The light gray region indicates *MW* and *D* combinations that result in a film thickness larger than 10 nm as determined by Equation (16). The dark gray region indicates films thicker than 20 nm. The green curve shows the synthetic parameters that result in brush packing of 50% as calculated from Equation (23). This packing curve divides the system-space into a densely packed brush regime (below curve) and a sparsely packed brush regime (above curve). The synthesized PEG films corresponding to the experimental indentation curves shown in Figure 7.5–1 are also plotted here to show their relative force sensitivities (2k, 5k, and 10k plotted in black, red, and blue respectively).

This system space analysis implies that the thickest brushes are those that will be most sensitive for detecting small forces. For a given D, Figure 7.5–2B shows that higher MW brushes boost force resolution. Likewise for a given MW, a smaller D results in a more sensitive brush (where slight fluctuations in the curves for increasing D towards the R_F limit are due to the simulation algorithm [98]). However, as mentioned for the TIR-based sensing scheme, there is a trade-off between film thickness and high spatial resolution. While the thickest brushes may be able to deform under the smallest loads, these indentations may not cause scattering signals above the noise of the far-field detection method, therefore, the system space must be limited to thinner film brush structures. Also, because actual synthesized films may have more limited structural properties, the system space is bounded to a smaller region (above the shaded areas and the 50% packing line) that represents practical combinations of MW and D available for nanomechanical performance optimization. From these considerations, it is clear that the benefit of utilizing the model in this manner is twofold: (1) we get an idea of the force response of a system before actual film synthesis, assuming the grafting methods are well established and the packing can be estimated *a priori*, and (2) if a required force-sensitivity is known then brush nanostructure criteria can be quickly identified and used to expedite experimental testing and optimization. Of our synthesized brushes, the 10k PEG film appears to be the most mechanically sensitive based on Figure 7.5–2B, but ultimately the 5k film may be better since the particles are closer to the fiber's surface resulting in higher signal-to-noise ratio and stronger distance-dependent scattering. Finally, it should be

noted that the model predicts sub-pN force sensitivity using the TIR fiber optic platform. These findings justify experimental development of such systems since the fiber force transducers can be much smaller ($< 10x$) than AFM or trap technologies [5] and their force sensitivities can match or exceed that of state-of-the-art instruments.

While the usefulness of the system space modeling approach is apparent for efficiently identifying practical packing states of the polymer brush, there are some important points to note that put this type of optimization analysis into perspective. First, on the synthetic side, these thin polymer brushes can be deposited using one of two well established techniques: the "graft-to" approach [101] or the "graft-from" approach. [113,114] For the films synthesized in this study we use the former method where PEG chains of fixed molecular weight are attached to the substrate as a pre-polymerized unit. In this case, the chain molecular weight in the brush is well defined, but it is difficult to control and tune the grafting site spacing. For the latter synthetic approach, the spatial density of reactive sites on a substrate can be tuned to some extent, [115] but the degree of polymerization is less controllable, leading to more variability in the final molecular weight of each chain. So while the system space analysis assumes that both *MW* and *D* are readily tunable synthesis parameters, the usefulness of the model in this capacity is ultimately limited by how well both packing variables can be controlled. This will vary depending on the specific polymer selected, brush synthesis method used, as well as on the particular substrate supporting the brush. Here, the 5k brush was shown to be the best film synthesized in terms of both mechanical and optical sensitivity, but that was for a brush synthesized on a flat Si

substrate. Perhaps using a nanostructured substrate like the single crystalline SnO_2 optical fiber may impose additional constraints on the packing density and therefore further limit transducer design options.

To this end, another potential error is related to the accuracy with which E can be known *a priori*. Again, we did not account for any electrostatic substrate effects in the model that can contribute extra force components to the indentation profile as discussed in the previous section. Furthermore, the osmotic pressure resulting from forcing solvated molecules (like water) out of the brush upon compression has not been explicitly accounted for in the indentation model either. [116] Depending on the indentation dependence of these extra terms, the slope of the indentation profile could increase or decrease which would alter the minimum resolvable force.

Other measurement criteria beyond force sensitivity may need to be considered as well such as the dynamic range of these transducers. It is suspected that the 2k brush has a small dynamic range because the 1 Å indentation accounts for a larger percentage of the total compressible thickness of the brush compared to the 5k or 10k films. This is another design limitation that must be deliberated on when optimizing these mechanical transducers for particular applications. Moreover, because the TIR-based optical sensing relies on an exponential decay of the optical field away from a waveguide surface, spatial sensitivity may actually change over the device's operable range. Therefore it is important to distinguish this sensitivity analysis, which highlights the capacity for detecting small forces, from an analysis of the resolution of the system, which would be important for designing systems to track small force

fluctuations during spectroscopic measurements. The latter may not be as fine as the initial indentation sensitivity.

Lastly, the idealized brush geometry used in the formulation of the model is a fundamental source of error associated with the analysis in this work. The Alexander-de Gennes scaling laws for the brush assumes a step function monomer density profile (i.e., all chains have the same height in the brush), but we have noted that a more accurate description of this profile is presented by Milner. [117] The surface roughness of the film and the irregular shape of an arbitrary scattering nanoparticle can also play a large role in determining the true sensitivity of a real system. As was the case for the previous indentation models described in this paper, further modifications can always be developed for a more accurate representation of these systems, but often those adjustments come at a cost of model complexity. However, for application of a real transducer system, experimental calibration is still always the first step before true quantitative measurements are collected, and is a major component to achieving high resolution and quantitative data from AFM and trap-based instruments. Thus, despite the many considerations that must be accounted for when modeling a real system, the model is still extremely useful as a tool for predicting the performance of a transducer to a reasonable degree, and for understanding the physical mechanisms contributing to the shape of the force profile.

7.6. Conclusion

In this work we developed a mechanistic model that can (1) analyze the mechanical properties of thin, compressible polymer coatings, (2) screen candidate systems for high-resolution, compact polymer-based nanomechanical transducers, and (3) predict the performance of force transducers that utilize thin polymer layers for mechanical feedback. We have formulated a discretized contact mechanics model where the partitioning is rooted in molecular scaling laws. Because the model's utility relies on its predictive power and general applicability to a breadth of different polymeric systems, we methodically analyzed profile trends in a realistic parameter space to understand how the structure determines the shape of the force response. The model was validated by comparing predicted force-indentation profiles for a thin polyethylene glycol (PEG) film to experimental AFM force curves which showed excellent agreement. Moreover, this analysis highlighted the usefulness of the model for backing out bulk mechanical properties from molecular-based scaling laws. Finally, as an example we presented the theoretical force sensitivities of a TIR-based, polymer-coated fiber optic probe to demonstrate how the model can be used to guide the synthetic optimization of polymeric layers for different applications based on sensitivity and dynamic range criteria. While the expression for the total force response was formulated on a purely geometric and mechanical basis that ignored substrate effects, solvation effects, and electrostatic interactions, these simplifications are justified by the model's predictive capacity and utility in guiding system development. Consequently, by knowing how film structure affects the force response

we can adapt the model to investigate other phenomena such as the influence of non-mechanical parameters (e.g., solvent, temperature) on polymer conformational changes which can have immediate implications for surface engineering, chemical encoding of surfaces, nanoparticle synthesis, and sensor technologies.

Chapter 7, in part, is a reprint of the material that appears in *Journal of Applied Physics*. (**Villanueva, Joshua**, Qian Huang, Donald J. Sirbuly. "Identification and design of novel polymer-based mechanical transducers: A nano-structural model for thin film indentation." *Journal of Applied Physics* 116, no. 10 (2014): 104307.) The dissertation author was the primary investigator and author of this material.

Chapter 8

Advanced Nanofiber TIRM Configurations

8.1. Configuration Space

Expansion of the nanofiber-based TIRM platform for more advanced characterization techniques is feasible, but requires a clear understanding of the physical differences in each setup. The effective implementation of the nanofiber TIRM platform for other applications must consider requirements of both spatial sensitivity and (perhaps more importantly) temporal sensitivity. As the analysis of Chapter 6 has shown, more complicated configurations of the transduction mechanism may have limitations determined by the dynamics of the nanoparticle near the surface and the data collection scheme implemented. This chapter highlights the versatility of nanofiber-based TIRM by formulating a configuration space to aid in identifying the capabilities and limitations of different manifestations of the platform. Several natural extensions of the previous, simple platform are shown in Figure 8.1. and they will be first discussed in an abstract sense before specific examples are presented.

The experiments described in Chapters 5 and 6 were based on the bare nanofiber case under hydrostatic conditions. From a device fabrication and experimental setup perspective this configuration, represented in Figure 8.1 as the upper left quadrant of the configuration space, is the simplest implementation of the nanofiber TIRM platform requiring only the bare nanofiber and an etched substrate. In this work much of the analysis was done with either a freely diffusing particle, or a particle stuck to the surface as shown in the figure. The main requirements for experimental reproducibility were a well-defined device cleaning, sample preparation, and experimental setup procedure. The more challenging aspect of this experimental

setup was developing and testing the accuracy of an appropriate data processing workflow for detecting and quantifying transient, spatially varying scattering events in the low signal-to-noise (SNR) regime. Additionally, identifying the appropriate models to understand the quantified signals and relate them to the physical properties of the colloidal system under investigation proved difficult due to the temporal resolution of the CCD imaging method.
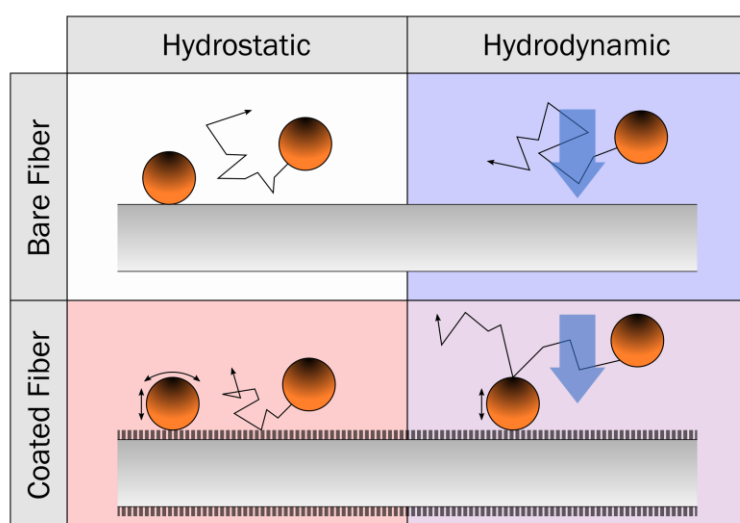
Figure 8.1. Configuration space of the nanofiber-TIRM platform. Extension of the nanofiber TIRM platform to other techniques that require adjustments to the base system of a bare nanofiber under static conditions. The addition of mechanical feedback for force measurements is depicted in the bottom row and the incorporation of fluid flow is shown in the right column.

The addition of a mechanically characterized polymer layer was considered theoretically in Chapter 7, again in the hydrostatic case. This setup is shown in the bottom left quadrant of the configuration space. In this form of the platform, the addition of the polymer layer adds another level of complexity to the fabrication process of the device. Identification and development of a robust polymer system and

synthesis procedure that produces a reproducible, chemically and mechanically stable coating around the nanofiber and the proper attachment of a nanoparticle on its surface is foundational to the implementation of the sensor. Moreover, the accurate calibration of the force-distance relationship is very important for the quantitative measurement of forces acting on the particle. Here, though, the data processing algorithms do not need to be as sophisticated because the scattering signal is spatially static and intensity fluctuations will most likely be in a higher SNR regime with the particle transducer localized close to the fiber surface. However, with the addition of a polymer layer the physical models describing the transducer mechanics must be thoroughly investigated to decouple the intensity modulation due to mechanical loading of the polymer itself from actuation of the particle. Also, the proper intensity-distance calibration will need to account for the variability in polymer thickness and roughness, which determine the attached particle's equilibrium position. There are also possible refractive index changes in the system with the addition of the polymer layer, which could influence the scattering intensity of the transducer. Depending on the type of characterization performed, the temporal resolution of the CCD may not be an issue.

Incorporating flow as an external force in the system also represents an interesting direction for exploring the capabilities of this device, shown in the right column of Figure 8.1. Flow-based characterization methods require further efforts in device design and integration. At the very least, these nanofibers must be integrated into a sealed microfluidic channel that can interface to a syringe pump or have some other means of flow generation. The difficulty lies in designing a system that can be

properly sealed during the experiment, but can also be opened for device cleaning. The seal must be good to eliminate bubbles in solution that can prevent proper imaging and also damage channel-suspended fiber. The appropriate processing algorithm will rely on the specific use of the fiber to study either free particles in solution or attached particles as discussed in the previous examples. The calibrations again will be very important. The intensity-distance calibration will always be required for the TIRM technique relying on distance measurements, and the operation of the device with mechanical feedback will require force-distance calibration. With flow, the local fluid velocity will also need to be measured simultaneously during the experiment and appropriate models will again be required to extract information from modulations of the scattering signal.

8.2.   Bare Nanofiber for Bond Strength Characterization

An example of extending the nanofiber TIRM platform for more advanced characterizations involves the use of the bare fiber for characterization of bond strengths by measuring the bond lifetimes using the TIRM mechanism. In this configuration, the scattering intensity serves only as an indicator of the formation of a bond or interaction and its strength is measured by the time it takes for the spontaneous breaking of the bond and correspondingly the loss of the scattering signal. Therefore, the exact intensity-distance calibration may not be necessary in this case, but consideration of the temporal resolution of the technique with respect to the maximum frame rate of the CCD will need to be examined.

This technique can be operated under static conditions or under flow to extend the dynamic range of the bond lifetime measurements. In the static fluid case, the behavior of the datasets can be extrapolated from the results of Chapter 5. It is expected that strong repulsive interactions will prevent the particle from getting close enough to the fiber for detection (similar to the low PBS concentration experiments). As the particles get closer (higher PBS concentration), the surface charges will eventually be screened enough such that the electrostatic repulsion between the nanoparticle and nanofiber will not be enough to prevent adsorption of the particles to the fiber. For the specific system conditions where the particles are attached to the fiber in a shallow potential minimum, the depth of this minimum will be related to the bond lifetime. Changing the properties of the system will influence this potential and therefore the distribution of scattering event lifetimes; the statistical analysis of the probability of escape under these different conditions will be required to extract quantitative potential information from the lifetime of the scattering events.

This nonspecific binding in a static fluid will comprise the lower limit for the obtainable lifetime measurements. The formation of a specific bond will naturally result in longer scattering event lifetimes. Generally speaking, as the bond strength increases, the likelihood of spontaneous bond breaking decreases and the scattering event will persist for impractically long periods of time. In this regime, the technique can still be useful if the addition of flow is leveraged. This will extend the dynamic range of the system by applying loads to the attached particles and thus alter the potential profiles to facilitate bond breaking. For this case, special attention must be

given to the development of the physical model that describes the fluid transport of a colloidal particle near the fiber as well as the flow-mediated load applied to the particle attached to a large fiber that itself will influence the exact flow profile in the microfluidic system. Furthermore, practical implementation will require considerable efforts to verify formation of the bond itself via several controls.

8.3. DNA-Coated Nanofiber for Hybridization Characterization

In another use of the fiber, we propose to leverage the fine distance sensitivity of the TIRM technique to examine the conformational changes of a DNA strand tethering a nanoparticle to the nanofiber surface as the strand is conjugated with complementary strands of varying degrees of base pair mismatch. In this implementation of the nanofiber TIRM, similar to the previous section, the particles only act as optical reporters of the properties of the bonds under investigation. It is expected that for the hybridization of a complementary strand to the single strand DNA tether, the hybridization will cause the tether to both stiffen and also change length. This should be detectable using the TIRM platform by both a change in the average scattering intensity of the tethered particle (the TIRM has been shown to have angstrom level distance sensitivity) and a change in the intensity fluctuations. With different levels base pair mismatch in the complementary strand, it is hypothesized that the degree of hybridization will change and result in different average intensity changes and likewise different intensity fluctuations.

Preliminary work for this project was done to test whether or not the nanofiber TIRM would be able to detect any physical changes to a single stranded DNA tether by conjugation of a complementary strand. The initial conceptualized experiments involved a 2D-DNA array with tether strands that were formed around the SnO_2 nanofiber. [118] An 80 nm DNA-coated gold nanoparticle was conjugated to the tether strand to form the sensor, and a free complementary strand was added to the solution to hybridize with the single stranded portion of the DNA tether as shown schematically in Figure 8.3–1. Data was collected of the scattering intensities of the attached particles before and after the addition of the free DNA strands to determine if there was a modulation of the signal as shown in Figure 8.3–2 and Figure 8.3–3.
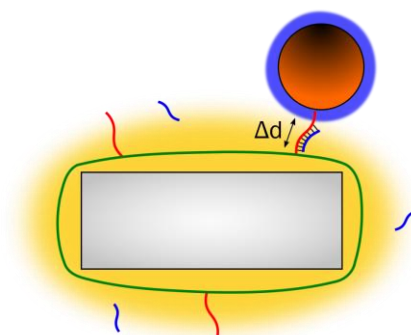
Figure 8.3–1. Characterization of DNA hybridization via changes in strand conformality. Schematic representation of the system setup. In the preliminary experiments, the nanoparticle was coated with DNA brush (blue coating) comprised of short strands of 10 adenine bases. The DNA-coated nanoparticle is conjugated to the end of a 20-thymine single-stranded DNA tether (red) that is attached to specific locations on a 2D-DNA array that coats the nanofiber (green). Free 10-base strands are added to the solution to conjugate with the open bases of the 20-thymine strand to induce a distance change, Δd, that can be detected by the TIRM method.
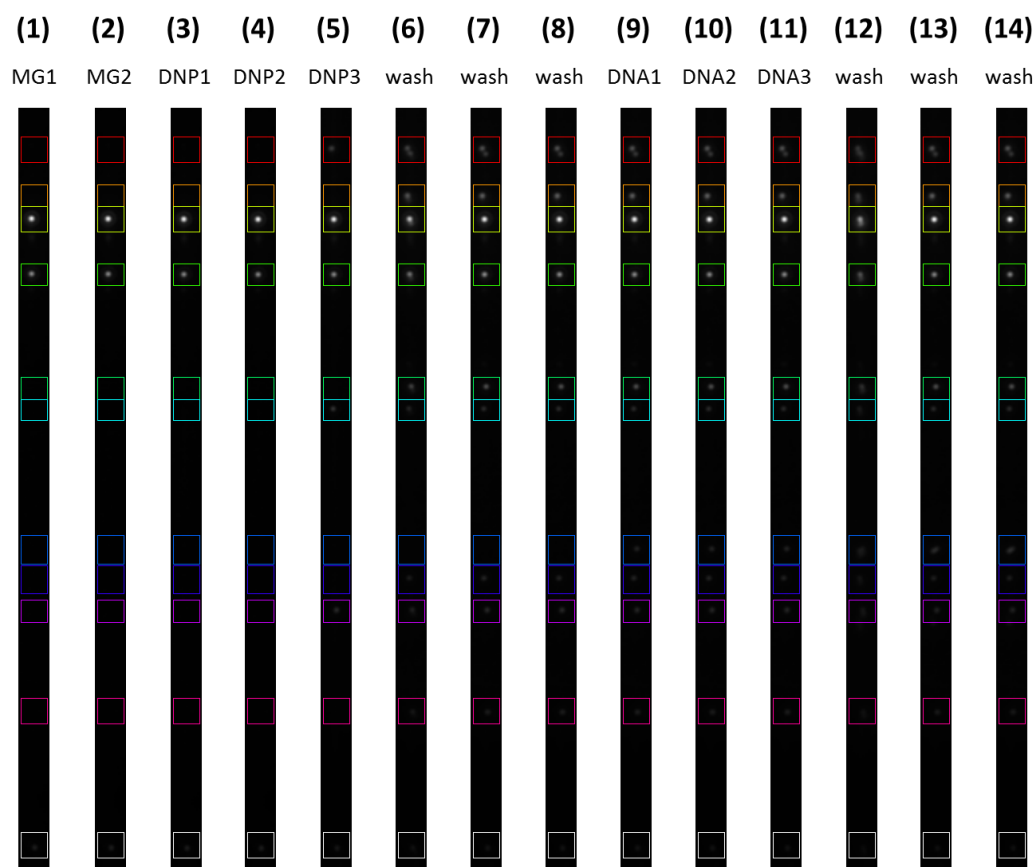
Figure 8.3–2. Location of persistent scattering signal during different stages of experiment. Each image shows the scattering intensity in the collected image averaged over the first 2k frames of the 20k frames comprising each experimental condition denoted by the different numbers. Image (1) and (2) shows the control scattering from the initial setup with 10 mM magnesium acetate solution surrounding the waveguide. In (3), (4), and (5) DNA-coated nanoparticles (synthesized on the same day) were added to the solution. (6), (7), and (8) are a washing step to remove any excess particles in solution after a few were allowed to attach to the fiber. (9), (10), and (11) show the addition of the free complementary DNA strands and (12), (13), and (14) are another washing step to remove the free DNA strands. All steps were performed using with the same 10 mM magnesium solution to maintain a consistent ionic strength. The ROI locations were determined using (14).
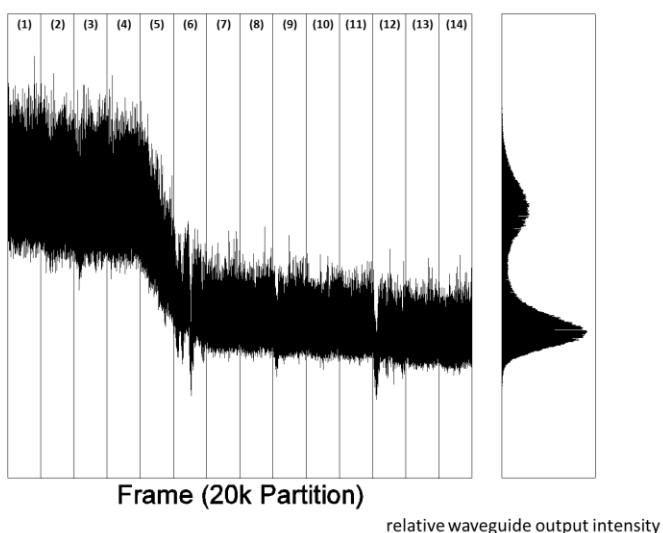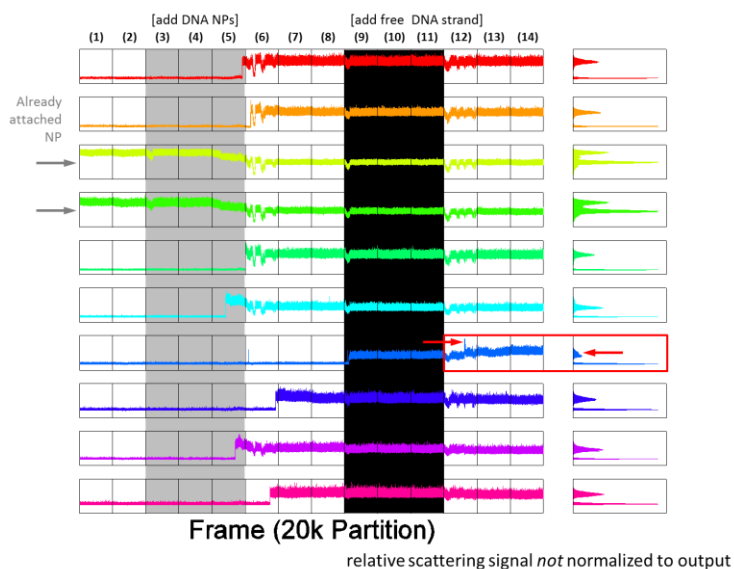
Figure 8.3–3. Scattering intensity of attached DNA-coated nanoparticles and corresponding waveguide output intensity. Preliminary data showing changes in the scattering intensity of attached DNA-coated nanoparticles in under different system conditions as well as the waveguide output intensity.

It is evident in looking at the scattering data for multiple attached particles that no modulation of scattering intensity was seen in the initial experiments before and after the addition of the free DNA strand. This does not necessarily mean the device is

not sensitive enough to detect changes due to hybridization. However, it is clear that the complicated assembly of the nanoparticle tether sensor must be analyzed thoroughly to verify the system under investigation is similar to the one shown in Figure 8.3–1. This is a nontrivial endeavor as the setup procedure must be optimized to verify the proper implementation of the technique, as was the case for the simple configuration in Chapter 5.

It is unclear if the attached particles in the experiment were actually DNA-tethered nanoparticles or if the particles were simply electrostatically adsorbed to the fiber or DNA array surface. The first step to verifying this sensor structure requires all parts of the setup being verified including the presence and conformation of the DNA array and tethers on the fiber. This is typically done using AFM for DNA arrays on a flat substrate, but in this case AFM is difficult with the suspended fiber architecture. Furthermore, the DNA array is formed in solution around the fiber rather than wrapping a pre-formed array sheet on the fiber. The electrostatic interactions at play dictating the DNA-coated nanofiber system must be understood better. Also, the presence of the tether and its orientation away from the nanofiber must be verified. The state of the DNA-coating on the nanoparticles must be examined as well. Once the sensor has been verified, then the hybridization of the free strand must also be considered, in particular where and how the free strands attach to the tether (if at all). Only once all aspects of the setup are thoroughly investigated can the experiment be used to probe the specifics of hybridization.

Chapter 9

Conclusion and Future Outlook

9.1. Summary of Contributions

In this dissertation we presented the development of a nanofiber-based TIRM platform and technique for characterizing the nanoscale interaction that dictate the behavior of freely diffusing Brownian nanoparticles near a wall in ionic solutions. Integral to the accuracy of the quantitative measurement, this dissertation outlined in detail the experimental and data processing procedure that influence the signal transformation pathway and ultimately determine what information is obtained from the measurements. We have performed a thorough analysis of the system from both a theoretical and experimental basis, showcasing a wide range of studies that can be performed using the nanofiber TIRM. For each parameter investigated experimentally, we were able to accurately predict the distributions trends expected from the model. This verifies the use of the model for analysis of more complex colloidal systems that may be more difficult to experimentally characterize. In an attempt to verify the system with theoretical predictions for nano particle size, we formulated a generalized far-field imaging model, which can be used to analyze all forms of scattering intensity data that are collected in the far field. Lastly, we generalized the development process of this technique for the simple colloidal characterization case and provided insight for the development of more complicated nanofiber TIRM instrumentation modalities. These included the incorporation of a polymeric mechanical feedback components, the use of the platform for characterization of bonds in a nanofiber-nanoparticle tether configuration, and the addition of fluid flow for the characterization of nanoscale interactions under mechanical loading.

9.2. Future Outlook

The development of a unique nanofiber TIRM technique is the first step towards formulating predictive theories that can extrapolate fundamental colloidal physics principles to mechanistically explain the solution-level behavior of these nanoparticle systems in complex environments. Performing both experimental and theoretical characterization on simpler colloidal systems in tandem has provided us with significant insight as to the delicate nature of properly analyzing their behavior. In particular, careful consideration of the effect all aspects of the experiment have on the quantitative signal output—from experimental setup and data collection to data processing—is crucial for comparison to theory. Addressing the limitations of the technique with respect to imaging speed or the mathematical treatment of the stochastically generated signals could have significant implications for the experimental investigation of complex colloidal systems, pushing the boundaries of nanomedicine research.

Appendix

Scattering Event Detection and Quantification Algorithm

```matlab
%% CLEAN AND INITIALIZE ENVIRONMENT %%%%%%%%%%%%%%%%%%%%%%%%%%%%%%%%%%%%
clc
format compact
close all
clear all

%% LOAD FILE %%%%%%%%%%%%%%%%%%%%%%%%%%%%%%%%%%%%%%%%%%%%%%%%%%%%%%%%%%%
maxfile = 160; f = 2000;
% Number of files in dataset; Number of video frames in each file

allimg = []; sigmat = []; threshmat = zeros(maxfile,f,3);
% Initialized parameters

for file = 1:maxfile
    fprintf('\nFile: %d ... ',file)

    filename = num2str(file);
    fileext = '.asc';
    raw2d = load(horzcat(filename,fileext));

    [l,h] = size(raw2d);
    w = l/f; % Width of a single frame in video
    raw3d = reshape(flipud(raw2d'),h,w,f);
    raw3d = raw3d(2:h-1,:,:);
    w = length(raw3d(1,:,1));
    h = length(raw3d(:,1,1));
    clear raw2d

    %   User Selected ROI for WG Output
    if file == 1
        favg = sum(raw3d,3)./f;
        imagesc(favg)
        axis image
        set(gca,'xticklabel',[])
        xlabel(sprintf('Box the WG Output'))
        recthandle = imrect(gca,[]);
        api = iptgetapi(recthandle);
        npos = api.getPosition();
        ypx = max([1 floor(npos(2))]):min([ceil(npos(2)+npos(4)) h]);
        close all
    end
    fprintf('Load and Reshape File Complete.\n')

%% SPATIAL/TEMPORAL EVENT DETECTION, CROSS-REFENCING, QUANTIFICATION %%%%%

%   Position-time image generation and background flattening
    w2 = (round(w/2)-5):(round(w/2)+4);
    % New 9px width centered tighter around WG.
    postime = reshape(mean(raw3d(:,w2,:),2),h,f);
    % Width-averaged intensity profile along length of fiber vs frame.
    ptflat = imtophat(postime,strel('disk',15));
    % Background flattening (in space and in time) using disk-shaped
    structuring element or radius 15px.
    kern = fspecial('gaussian',9,1);
```

```matlab
    % Gaussian kernel for filtering; 5x5 size, 0.75 sigma.
    ptfinal = conv2(ptflat,kern,'same');
    % Gaussian blurring of image to reduce high (spatial) frequency noise.
    allimg = vertcat(allimg,[ptflat;mean(ptfinal,1)]);
    % Image matrix for comparison of entire dataset.

    tdet = []; tX = 1;
    for i = 1:ypx(1)
        tprof = ptfinal(i,:);
        tmph = mean(tprof)+tX*std(tprof);
        tprof(diff([0 tprof]) < tX*std(tprof)) = tmph*0.9;
        if sum(tprof > tmph) ~= 0
            [pkt,t] = ...
                findpeaks(tprof,'minpeakheight',tmph,'threshold',0*tmph,...
                'npeaks',round(f./2));
            tdet = vertcat(tdet,[reshape(t,[],1) ones(length(t),1).*i]);
        end
    end

    thresh = zeros(1,f,3); pdet = []; pX = 1; mpd = 3;
    for j = 1:f
        pprof = ptfinal(1:ypx(1),j);
        pmph = mean(pprof)+pX*std(pprof);
        thresh(:,j,:) = reshape([mean(pprof),std(pprof),pmph],1,1,3);
        if sum(pprof > pmph) ~= 0
            [pky,y] = ...
                findpeaks(pprof,'minpeakheight',pmph,'minpeakdistance',mpd,...
                'npeaks',50);
            pdet = vertcat(pdet,[ones(length(y),1).*j reshape(y,[],1)]);
        end
    end
    threshmat(file,:,:) = thresh;

    det = sortrows(intersect(tdet,pdet,'rows'),1);
    for k = 1:length(det(:,1))
        if mod(k,10) == 0 | k == length(det(:,1))
            fprintf('File %0.0f/%0.0f - Percent Done: %0.1f\n',...
                file,maxfile,k./length(det(:,1))*100)
        end
        sf = raw3d(:,:,det(k,1));
        rw = 3; %%% Half-width of ROI Size %%%

%   Localization of event peak scattering value: (locy,sx)
        ly1 = max([det(k,2)-2, 1]);
        ly2 = min([det(k,2)+2, h]);
        [pksx,sx] = findpeaks(mean(sf(ly1:ly2,:),1),'minpeakdistance',w-1);

%   Localization of output peak scattering value: (outy,outx)
        [pkouty,outy] = findpeaks(mean(sf(ypx,w2),2),'minpeakdistance',...
                length(ypx)-1);
        outy = outy + ypx(1) - 1;
        ly1 = max([outy-2, 1]);
        ly2 = min([outy+2, h]);
        [pkoutx,outx] = findpeaks(mean(sf(ly1:ly2,:),1),...
                'minpeakdistance',w-1);

%   Defining ROI Bounds for scatering event
        sh = max([det(k,2)-rw,1]):min([det(k,2)+rw,h]);
        sw = max([sx-rw,1]):min([sx+rw,w]);
        nh = max([outy-rw,1]):min([outy+rw,h]);
```

```matlab
        nw = max([outx-rw,1]):min([outx+rw,w]);

%   Calculating background-subtracted, ROI-integrated intensity for event and
    output
        bkgd = mode(reshape(sf,1,[]));
        As = (sh(end)-sh(1)+1)*(sw(end)-sw(1)+1);
        An = (nh(end)-nh(1)+1)*(nw(end)-nw(1)+1);
        Isb = sum(sum(sf(sh,sw)));
        Inb = sum(sum(sf(nh,nw)));
        Is = Isb-As*bkgd;
        In = Inb-An*bkgd;
        Iscb = Isb./Inb;
        Isc = Is./In;

%   Calculating peak-value intensity for event and output (not background
    subtracted)
        Ispk = sf(det(k,2),sx);
        Inpk = sf(outy,outx);
        Iscpk = Ispk./Inpk;

%   DATA MATRIX
        sigmat0 = [file, det(k,1), det(k,2), sx,...
                % [1,2,3,4]   (event time and location)
                    Ispk, Inpk, Iscpk,...
                % [5,6,7]     (peak intensity)
                    Is, In, Isc,...
                % [8,9,10]    (integrated intensity, background subtracted)
                    Isb, Inb, Iscb,...
                % [11,12,13]  (integrated intensity with background)
                    As, An, bkgd];
                % [14,15,16]  (ROI areas and background value)
        sigmat = vertcat(sigmat,sigmat0);
    end
end

Isctot = sigmat;
save Isctot Isctot
save allimg allimg
save paramvec h w f maxfile rw
save threshparams ypx threshmat mpd w2
```

Gaussian Mixture Model Data Filtering

```
%% GAUSSIAN MIXTURE DISTRIBUTION CLUSTER ANALYSIS %%%%%%%%%%%%%%%%%%%
pv = [Isctot(:,5) Isctot(:,8)];
gm = gmdistribution.fit(pv,2);
P = posterior(gm,pv);
idx = cluster(gm,pv);
sclust = idx(pv(:,1) == max(pv(:,1)));
nclust = setdiff([1 2],sclust);
detnoise = (idx == nclust);
detsig = (idx == sclust);

%   Filtering out GMM-based noise cluster (double filtering)
IsctotGMM = Isctot(P(:,sclust)-rand(size(P(:,1))) > 0 & P(:,nclust)-
rand(size(P(:,1))) < 0,:);
IsctotGMM(IsctotGMM(:,3) <= 10,:) = [];
save IsctotGMM IsctotGMM
```

Brownian Dynamics Simulations

```matlab
clc
close all hidden
clear all
format compact

%% PARAMETERS
S = 1000;                   % size of simulation box (nm)
N = 500;                    % number of NPs in simulation
R = ones(N,1).*75;          % radius of NP (nm)
T = 298;                    % temp (K)
kB = 1.38e-23*1e9;          % Boltzmann constant (N*nm/K)
e0e = 7.08e-10*1e-9;        % Permitivity of solution (F/nm)
mu = 8.9e-4*1e-18;          % viscosity of water at 298K (Ns/nm^2)
g = 6*pi*mu.*R;             % drag coefficient (Ns/nm)

K = 0.415;                  % Debye-Huckel parameter (nm^-1)
                            % K = {0.093, 0.131, 0.293, 0.359, 0.415} nm^-1
                            % for {0.005x, 0.01x, 0.05x, 0.075x, 0.1x} PBS
s1 = 0.05*1e-18;            % surface charge density (C/nm^2)
B = 0.24;                   % ratio of s1 to s2 (m/m)
tau = 34;                   % Isc decay constant (nm)
I0 = (R./40).^0.69;

exptime = 5000e-6;          % exposure time (s)
dt2 = exptime/1000;         % recorded time step (s)
dt = dt2/100;               % simulation time step(s)
t = 25000000*dt2/N;         % total simulation time (s)

%%  1D-BD SIMULATION
rx = (R)+(S-R).*(rand(N,1));   % random initial x-position (nm)
rx0 = rx;                      % initial position distribution
H = rx-(R);                    % distance from WG (nm)

count = 1;
l = round(t/dt2);
posmat = zeros(N,2,l-1);
I = zeros(N,1);
expnum = round(exptime./dt);
rxmat = zeros(N,expnum);
Imat = zeros(N,4,round(t./exptime)-1);
expdispmat = zeros(N,round(t./exptime));
expdispmat(:,1) = H;
expcount = 0;
Icount = 0;
ncount = 0;

for i = 2:round(t/dt)
    i/(t/dt)
    Fx = ((pi.*R.*s1^2*1e9)./(e0e*K)).*((((B+1)^2)./...
        (exp(K.*H)-1))-(((B-1)^2)./(exp(K.*H)+1)));
                                % deterministic force term (N)
    Sx = sqrt(2*kB*T.*g*dt).*randn(N,1);
                                % stochastic term (N)
    H0 = rx-R;                  % old distance from WG (m)
    rxnew = rx+(Fx./g).*dt+(Sx./g);
                                % new particle position after time dt (m)
```

```matlab
    jx = find(rxnew >= S);
    ncount = ncount + length(find(rxnew-R <= 0));
    % periodic boundary conditions
    if isempty(jx) == 0
        for w = 1:length(jx)
            rxnew(jx(w)) = S-rem(rxnew(jx(w)),S);
        end
    end


    rx = rxnew;
    H = rx-R;         % distance from WG (m)

    if expcount.*dt <= exptime
        I = I + (0.5).*(I0.*exp(-H0./tau)+I0.*exp(-H./tau)).*dt;
        expcount = expcount + 1;
        rxmat(:,expcount) = single(rx);
    else
        Icount = Icount + 1;
        Imat(:,:,Icount) = [I./exptime mean(rxmat,2) std(rxmat,0,2) R];
        It0(:,:,Icount) = [I0.*exp(-H./tau) H];
        expdispmat(:,Icount+1) = rx;
        expcount = 0;
        I = zeros(N,1);
        rxmat = zeros(N,expnum);
    end
    if mod(i,round(dt2./dt)) == 0
        count = count + 1;
        posmat(:,:,count-1) = [single(rx) R];
        i*dt/t
    end
end
```

References

[1]   Y. Hiraoka, J. Sedat, and D. Agard, Science **238**, (1987).

[2]   A. Boyer and E. Cissé, Mater. Sci. Eng. B **13**, 103 (1992).

[3]   S. Tadigadapa and K. Mateti, Meas. Sci. Technol. **20**, 92001 (2009).

[4]   A. Yu, Z. Liang, J. Cho, and F. Caruso, Nano Lett. **3**, 1203 (2003).

[5]   K. C. Neuman and A. Nagy, Nat. Methods **5**, 491 (2008).

[6]   N. A. Burnham, X. Chen, C. S. Hodges, G. A. Matei, E. J. Thoreson, C. J. Roberts, M. C. Davies, and S. J. B. Tendler, Nanotechnology **14**, 1 (2003).

[7]   H. Felgner, O. Müller, and M. Schliwa, Appl. Opt. **34**, 977 (1995).

[8]   D. R. Thévenot, K. Toth, R. A. Durst, and G. S. Wilson, Biosens. Bioelectron. **16**, 121 (2001).

[9]   G. M. Gouda and C. L. Nagendra, Sensors Actuators A **155**, 263 (2009).

[10]   M. D. Haw, J. Phys. Condens. Matter **14**, 315 (2002).

[11]   M. Elsabahy and K. L. Wooley, Chem. Soc. Rev. **41**, 2545 (2012).

[12]   A. Albanese, P. S. Tang, and W. C. W. Chan, Annu. Rev. Biomed. Eng. **14**, 1 (2012).

[13]   L. Dykman and N. Khlebtsov, Chem. Soc. Rev. **41**, 2256 (2012).

[14]   S. D. Steichen, M. Caldorera-Moore, and N. A. Peppas, Eur. J. Pharm. Sci. **48**, 416 (2013).

[15]   A. K. Gupta and M. Gupta, Biomaterials **26**, 3995 (2004).

[16]   Z. Li, J. C. Barnes, A. Bosoy, J. F. Stoddart, and J. I. Zink, Chem. Soc. Rev. **41**, 2590 (2012).

[17]   G. Sonavane, K. Tomoda, and K. Makino, Colloids Surfaces B Biointerfaces **66**, 274 (2008).

[18]   F. Alexis, E. Pridgen, L. K. Molnar, and O. C. Farokhzad, Mol. Pharm. **5**, 505 (2008).

[19]   S.-D. Li and L. Huang, Mol. Pharm. **5**, 496 (2008).

[20] D. E. Owens III and N. A. Peppas, Int. J. Pharm. **307**, 93 (2006).

[21] M. A. Dobrovolskaia, P. Aggarwal, J. B. Hall, and S. E. McNeil, Mol. Pharm. **5**, 487 (2008).

[22] P. Aggarwal, J. B. Hall, C. B. McLeland, M. A. Dobrovolskaia, and S. E. McNeil, Adv. Drug Deliv. Rev. **61**, 428 (2009).

[23] W. I. Hagens, A. G. Oomen, W. H. de Jong, F. R. Cassee, and A. J. A. M. Sips, Regul. Toxicol. Pharmacol. **49**, 217 (2007).

[24] J. N. Israelachvili, *Intermolecular and Surface Forces* (Academic Press, 2011).

[25] A. C. Anselmo and S. Mitragotri, AAPS J. **17**, 1041 (2015).

[26] A. S. Hoffman, Adv. Drug Deliv. Rev. **65**, 10 (2013).

[27] P. M. Valencia, O. C. Farokhzad, R. Karnik, and R. Langer, Nat. Nanotechnol. **7**, 623 (2012).

[28] N. Kamaly, Z. Xiao, P. M. Valencia, A. F. Radovic-Moreno, and O. C. Farokhzad, Chem. Soc. Rev. **41**, 2971 (2012).

[29] R. Kubo and R., Reports Prog. Phys. **29**, 306 (1966).

[30] P. Attard, Curr. Opin. Colloid Interface Sci. **6**, 366 (2001).

[31] C. W. Outhwaite, L. B. Bhuiyan, and S. Levine, J. Chem. Soc., Faraday Trans. 2 **76**, 1388 (1980).

[32] G. M. Bell, S. Levine, and L. N. McCartney, J. Colloid Interface Sci. **33**, 335 (1970).

[33] D. C. Grahame, Chem. Rev. **41**, 441 (1947).

[34] M. A. Bevan and D. C. Prieve, J. Chem. Phys. **113**, 1228 (2000).

[35] P. Huang and K. Breuer, Phys. Rev. E **76**, 46307 (2007).

[36] F. A. Carvalho and N. C. Santos, IUBMB Life **64**, 465 (2012).

[37] D. Kirmizis and S. Logothetidis, Int. J. Nanomedicine **5**, 137 (2010).

[38] C. M. Hoo, N. Starostin, P. West, and M. L. Mecartney, J. Nanoparticle Res. **10**, 89 (2008).

[39] T. T. Perkins, Annu. Rev. Biophys. **43**, 279 (2014).

[40] P. C. Ashok and K. Dholakia, Curr. Opin. Biotechnol. **23**, 16 (2012).

[41] M. L. Juan, M. Righini, and R. Quidant, Nat. Photonics **5**, 349 (2011).

[42] D. J. Sirbuly, R. W. Friddle, J. Villanueva, and Q. Huang, Reports Prog. Phys. **78**, 24101 (2015).

[43] P. A. Hassan, S. Rana, and G. Verma, Langmuir **31**, 3 (2015).

[44] G. Bryant, S. Martin, A. Budi, and W. van Megen, (2002).

[45] C. Urban and P. Schurtenberger, J. Colloid Interface Sci. **207**, 150 (1998).

[46] D. C. Prieve and N. A. Frej, Langmuir **6**, 396 (1990).

[47] S. G. Flicker, J. L. Tipa, and S. G. Bike, J. Colloid Interface Sci. **158**, 317 (1993).

[48] D. C. Prieve, Colloid Interfuce Sci **82**, 93 (1999).

[49] A. Snyder and J. Love, *Optical Waveguide Theory* (1983).

[50] P. K. Jain, K. S. Lee, I. H. El-Sayed, and M. A. El-Sayed, J. Phys. Chem. B **110**, 7238 (2006).

[51] D. C. Prieve, Adv. Colloid Inerface Sci. **82**, 93 (1999).

[52] N. Bertrand and J.-C. Leroux, J. Control. Release **161**, 152 (2012).

[53] M. Law, D. J. Sirbuly, J. C. Johnson, J. Goldberger, R. J. Saykally, and P. Yang, Science **305**, (2004).

[54] F. J. Arlinghaus, J. Phys. Chem. Solids **35**, 931 (1974).

[55] I. Yoon, S. E. Baker, K. Kim, Y. Wang, S. C. Esener, and D. J. Sirbuly, Nanoscale **5**, 552 (2013).

[56] I. Yoon, S. E. Baker, K. Kim, N. O. Fischer, D. Heineck, Y. Wang, S. C. Esener, and D. J. Sirbuly, Nano Lett. 1440 (2013).

[57] N. Lloret, R. S. Frederiksen, T. C. Møller, N. I. Rieben, S. Upadhyay, L. De Vico, J. H. Jensen, J. Nygård, and K. L. Martinez, Nanotechnology **24**, 35501 (2013).

[58] D. C. Prieve and N. A. Frej, Langmuir **6**, 396 (1990).

[59] J. Ståhlberg, U. Appelgren, and B. Jönsson, J. Colloid Interface Sci. **176**, 397 (1995).

[60] R. Hogg, T. W. Healy, and D. W. Fuerstenau, Trans. Faraday Soc. **62**, 1638 (1966).

[61] G. Arya, Mol. Simul. **42**, 1102 (2016).

[62] S. M. Ahmed and D. Maksimov, J. Colloid Interface Sci. **29**, 97 (1969).

[63] Q. Huang, F. Teran Arce, J. Lee, I. Yoon, J. Villanueva, R. Lal, and D. J. Sirbuly, Nanoscale (2016).

[64] I. Yoon, S. E. Baker, K. Kim, N. O. Fischer, D. Heineck, Y. Wang, S. C. Esener, and D. J. Sirbuly, Nano Lett. **13**, 1440 (2013).

[65] G. Volpe, T. Brettschneider, L. Helden, and C. Bechinger, in *Front. Opt.* (OSA, Washington, D.C., 2010).

[66] D. C. Prieve and J. Y. Walz, Appl. Opt. **32**, 1629 (1993).

[67] I. Karatzas and S. E. Shreve, *Brownian Motion and Stochastic Calculus* (Springer US, 1988).

[68] G. E. Uhlenbeck and L. S. Ornstein, Phys. Rev. **36**, 823 (1930).

[69] D. J. Müller and Y. F. Dufrêne, Trends Cell Biol. **21**, 461 (2011).

[70] S. Kasas, G. Longo, and G. Dietler, J. Phys. D. Appl. Phys. **46**, 133001 (2013).

[71] M. Capitanio and F. S. Pavone, Biophys. J. **105**, 1293 (2013).

[72] E. K. Dimitriadis, F. Horkay, J. Maresca, B. Kachar, and R. S. Chadwick, Biophys. J. **82**, 2798 (2002).

[73] K. D. Costa, Dis. Markers **19**, 139 (2004).

[74] A. Alemany, N. Sanvicens, S. de Lorenzo, M.-P. Marco, and F. Ritort, Nano Lett. **13**, 5197 (2013).

[75] Y. F. Dufrêne, E. Evans, A. Engel, J. Helenius, H. E. Gaub, and D. J. Müller, Nat. Methods **8**, 123 (2011).

[76] M. Law, D. J. Sirbuly, J. C. Johnson, J. Goldberger, R. J. Saykally, and P. Yang, Science **305**, 1269 (2004).

[77]   M. A. C. Stuart, W. T. S. Huck, J. Genzer, M. Müller, C. Ober, M. Stamm, G. B. Sukhorukov, I. Szleifer, V. V Tsukruk, M. Urban, F. Winnik, S. Zauscher, I. Luzinov, and S. Minko, Nat. Mater. **9**, 101 (2010).

[78]   L. Zhai, Chem. Soc. Rev. **42**, 7148 (2013).

[79]   M. Reinhardt, J. Dzubiella, M. Trapp, P. Gutfreund, M. Kreuzer, A. H. Gröschel, A. H. E. Müller, M. Ballauff, and R. Steitz, Macromolecules **46**, 6541 (2013).

[80]   H. Hertz, J. für die reine und Angew. Math. **92**, 156 (1882).

[81]   J. Boussinesq, *Application Des Potentiels À L'étude de L'équilibre et Du Mouvement Des Solides Élastiques* (Gauthier-Villars, 1885).

[82]   I. N. Sneddon, Int. J. Eng. Sci. **3**, 47 (1965).

[83]   E. Winkler, *Die Lehre von Der Elasticitaet Und Festigkeit* (Dominicus, 1867).

[84]   A. D. Kerr, J. Appl. Mech. **31**, 491 (1964).

[85]   A. D. Kerr, Ingenieur-Archiv **54**, 455 (1984).

[86]   V. L. Popov, Friction **1**, 41 (2013).

[87]   V. L. Popov, Phys. Mesomech. **15**, 254 (2013).

[88]   M. Heß, Phys. Mesomech. **15**, 264 (2013).

[89]   P. J. Flory, J. Chem. Phys. **10**, 51 (1942).

[90]   M. L. Huggins, J. Phys. Chem. **46**, 151 (1942).

[91]   S. Alexander, J. Phys. **38**, 983 (1977).

[92]   P. G. de Gennes, *Scaling Concepts in Polymer Physics* (Cornell University Press, 1979).

[93]   P. G. de Gennes, Macromolecules **13**, 1069 (1980).

[94]   M. Daoud and P. G. de Gennes, J. Phys. **38**, 85 (1977).

[95]   P. G. de Gennes, Adv. Colloid Interface Sci. **27**, 189 (1987).

[96]   S. T. Milner, T. A. Witten, and M. E. Cates, Macromolecules **21**, 2610 (1988).

[97]   S. T. Milner, Europhys. Lett. **7**, 695 (1988).

[98]   J. Villanueva, Q. Huang, and D. J. Sirbuly, J. Appl. Phys. **116**, 104307 (2014).

[99]   F. Beer, E. Johnston, and J. DeWolf, *Mechanics of Materials* (McGraw-Hill, 2002).

[100] M. A. Rixman, D. Dean, and C. Ortiz, Langmuir **19**, 9357 (2003).

[101] Z. Yang, J. A. Galloway, and H. Yu, Langmuir **15**, 8405 (1999).

[102] Q. Huang, I. Yoon, J. Villanueva, K. Kim, and D. J. Sirbuly, Soft Matter (2014).

[103] A. Halperin, Langmuir **15**, 2525 (1999).

[104] T. Drobek, N. D. Spencer, and M. Heuberger, Macromolecules **38**, 5254 (2005).

[105] G. Stan, F. W. DelRio, R. I. MacCuspie, and R. F. Cook, J. Phys. Chem. B **116**, 3138 (2012).

[106] H. Xu, F. Yan, E. E. Monson, and R. Kopelman, J. Biomed. Mater. Res. A **66**, 870 (2003).

[107] I. M. Rio-Echevarria, F. Selvestrel, D. Segat, G. Guarino, R. Tavano, V. Causin, E. Reddi, E. Papini, and F. Mancin, J. Mater. Chem. **20**, 2780 (2010).

[108] S. Upadhyayula, T. Quinata, S. Bishop, S. Gupta, N. R. Johnson, B. Bahmani, K. Bozhilov, J. Stubbs, P. Jreij, P. Nallagatla, and V. I. Vullev, Langmuir **28**, 5059 (2012).

[109] J. S. Villarrubia, Surf. Sci. **321**, 287 (1994).

[110] J. S. Villarrubia, J. Res. Natl. Inst. Stand. Technol. **102**, (1997).

[111] J. L. Hutter and J. Bechhoefer, Rev. Sci. Instrum. **64**, 1868 (1993).

[112] B. Knoll and F. Keilmann, Opt. Commun. **182**, 321 (2000).

[113] J. Pyun, T. Kowalewski, and K. Matyjaszewski, Macromol. Rapid Commun. **24**, 1043 (2003).

[114] S. Edmondson, V. L. Osborne, and W. T. S. Huck, Chem. Soc. Rev. **33**, 14 (2004).

[115] H. G. Börner, D. Duran, K. Matyjaszewski, M. da Silva, and S. S. Sheiko, Macromolecules **35**, 3387 (2002).

[116] Y. Xu, S. Bolisetty, M. Drechsler, B. Fang, J. Yuan, L. Harnau, M. Ballauff, and A. H. E. Müller, Soft Matter **5**, 379 (2009).

[117] S. T. Milner, Science **251**, 905 (1991).

[118] Y. He, Y. Chen, H. Liu, A. E. Ribbe, and C. Mao, J. Am. Chem. Soc. **127**, 12202 (2005).